THERMAL TRANSPORT IN P3HT NANOSTRUCTURES AND NANOCOMPOSITES

A Dissertation
Presented to
The Academic Faculty

by

Matthew Kirby Smith

In Partial Fulfillment
of the Requirements for the Degree
Doctor of Philosophy in the
School of Materials Science and Engineering

Georgia Institute of Technology
May 2017

THERMAL TRANSPORT IN P3HT NANOSTRUCTURES AND NANOCOMPOSITES

Approved by:

Dr. Baratunde Cola, Co-Advisor
George W. Woodruff School of Mechanical Engineer and School of Materials Science and Engineering
Georgia Institute of Technology

Dr. David Bucknall
School of Materials Science and Engineering
Georgia Institute of Technology
School of Engineering and Physical Sciences
Heriot Watt University

Dr. Kyriaki Kalaitzidou, Co-Advisor
George W. Woodruff School of Mechanical Engineer and School of Materials Science and Engineering
Georgia Institute of Technology

Dr. Elsa Reichmanis
School of Chemical and Bimolecular Engineering
Georgia Institute of Technology

Dr. Ken Gall
School of Mechanical Engineering and Materials Science
Duke University

Date Approved: March 8th, 2017

To my family

ACKNOWLEDGEMENTS

I would like to thank my graduate advisors, Dr. Baratunde Cola and Dr. Kyriaki Kalaitzidou, for their support, guidance, and comradery throughout my graduate studies. Dr. Cola, your optimism and infinite curiosity have continued to inspire me and have provided me with the courage to pursue new challenges with confidence and to not be deterred by setbacks. I cannot thank you enough for providing me with the ideal balance of freedom and guidance, which has made my experience at Georgia Tech truly enjoyable and fruitful. Dr. Kalaitzidou, you have always been focused on what is best for me and my future and I truly appreciate that. Your practicality and ability to focus on the task at hand have taught me to how to clearly formulate my goals and to see things through to completion. Thank you both for your mentorship, I am forever grateful to have you both as my advisors.

In addition, I would also like the thank Dr. David Bucknall, Dr. Ken Gall, and Dr. Elsa Reichmanis for serving on my committee. Dr. Bucknall, your kindness and mentorship during my first two years of graduate studies were invaluable, as it quelled my fears and gave me the confidence that I could succeed at this level. Dr. Gall, your commercialization efforts inspired me and our multiple conversations on the topic provided me with assurance that although difficult, it is possible to successfully pursue commercialization in an academic setting. Dr. Reichmanis, thank you for your support and for providing me with multiple opportunities through the IGERT program, I made many friends and valuable contacts through that experience.

I would like to thank Dr. Virendra Singh and Dr. Thomas Bougher; the three of us shared a small closet office for my first few years at Georgia Tech and it would be difficult to quantify the vast amount of information I learned from them. I will always be grateful for Dr. Singh's patience, guidance and willingness to teach, even if I was taking longer than expected to catch onto a topic. Dr. Bougher and I have continued to collaborate throughout my studies, initially as a friendly and educational working relationship (where I was the person often being educated), but now has grown to the point where I consider

him one of my closest collaborators, friends and mentors. Dr. Bougher's deep technical understanding and unrivaled attention to detail have left me with a new appreciation for thoroughness. My time in the lab was significantly more enjoyable due to my friendship with both Dr. Singh and Dr. Bougher, and I will always be grateful to have been placed in their office.

Finally, I would like to thank my family, whom I owe everything and through their successes, have always provided me with the confidence and fearlessness to pursue my goals relentlessly. I am the youngest child of five and have been fortunate to have 7 role models and protectors throughout my life, including my siblings and parents. My passion for the environment and scientific curiosity was deeply embedded at an early age during our many camping trips and explorations through the mountains of Wyoming. I could never thank my parents enough for their love and support and for the sacrifices they made to raise my siblings and me. To my siblings, whom are my best friends, you have paved the way for me my entire life and I thank you for being such amazing people. To my girlfriend, Clarke Flowers, whom stayed in a long-distance relationship with me through three years of graduate studies. Our late-night phone conversations and monthly visits were the only thing that kept me sane during months of long work days and sleeping in the lab. Thank you for always supporting me and being there.

TABLE OF CONTENTS

LIST OF TABLES

LIST OF FIGURES

LIST OF SYMBOLS AND ABBREVIATIONS

BLT	bond-line thickness
k	thermal conductivity
P3HT	poly(3-hexylthiophene)
ρ	density
T	temperature
CNT	carbon nanotube
MWCNT	multi-walled carbon nanotube
PE	polyethylene
AAO	anodic aluminum oxide
R	thermal resistance
R_c	thermal contact resistance
λ	laser wavelength
σ	electrical conductivity
D	diameter
L	length
c	specific heat
OAL	optical absorbance length
TD	thermal diffusivity
LIG	laser induced graphene
δ	uncertainty

V	voltage
I	current
Mw	weight average molecular weight
Mn	number average molecular weight
f	surface fraction
ϑ	contact angle
TIM	thermal interface material
TCR	thermal contact resistance
PA	photoacoustic
CA	contact angle
CAH	contact angle hysteresis
CTE	coefficient of thermal expansion

SUMMARY

Consumers continue to pressure electronic device manufactures to produce smaller, higher performance, and higher reliability products. Moreover, by decreasing size and increasing computational power, electronic devices get hotter and fail faster and thermal management is a growing challenge. Thermal interface materials (TIMs) are used to maximize heat transport across the interface connecting heat generating components (such as processors, batteries, or any other heat generating piece of hardware) to the heat sinking components (such as heat sinks, heat pipes, cold plates, etc.). The focus of this work is to explore the thermal transport properties of three new poly(3-hexylthiophene-2,5-diyl) (P3HT) based nanostructured material systems that show potential for use as TIMs; vertically aligned P3HT nanotubes and nanofibers, vertically aligned P3HT/multi-walled carbon nanotube (MWCNT) composite nanofibers, and P3HT infiltrated laser-induced graphene (LIG) foam composite thin films.

Solution processed P3HT nanotubes are fabricated using a simple template technique where polymer solution is cast onto nanoporous anodic aluminum oxide (AAO) templates. The solution wets the template and fills the nanopores, forming P3HT nanotubes along the length of the pore upon solvent evaporation. The thermal conductivity of the P3HT nanotubes is measured using the photoacoustic (PA) technique and is approximately 1 W/m-K, or ~5x that of bulk P3HT film, indicating preferential chain alignment along the long axis of the tube. In addition, a novel template etching process to control the nanotube array surface morphology is proposed and the relationship between the degree of nanotube clustering (due to capillary forces) and the thermal contact

resistance is established. The solution processed nanotube arrays proved to have poor mechanical stability and a melt processing technique is introduced to produce P3HT nanofibers. The nanofiber thermal conductivity is measured as a function of P3HT molecular weight and nanofiber diameter, where the highest known P3HT thermal conductivity (~7 W/m-K) is observed in 100 nm diameter fibers. In addition, polarized Raman spectroscopy is used to demonstrated preferential polymer chain alignment along the nanofiber's long axis.

To further improve thermal transport in the melt processed nanofibers, a novel method to fabricate P3HT/MWCNT composite fibers is introduced. AAO templates are first infiltrated with MWCNT through sonication in MWCNT dispersion and then subsequently filled with polymer melt. TEM imaging reveals strong preferential alignment of MWCNT along the fibers long axis and the processing conditions are manipulated to achieve P3HT/MWCNT composite fibers with MWCNT wt% of up to 55%. Composite fiber thermal conductivity peaks at a value of 4.7 ±1.1 W/m-K for the 200 nm diameter 24 wt% MWCNT fibers, or roughly twice the value of pure P3HT 200 nm melt processed fiber. Higher MWCNT weight percentages results in pore blocking and the inability of the P3HT to fully infiltrate the MWCNT filled nanopores, which significantly reduces fiber thermal transport.

Lastly, a new material system is introduced where P3HT solution is infiltrated into a three-dimensional graphene foam network. The P3HT/LIG composites exhibit an unexpected increase in LIG foam thermal conductivity, from 0.68 W/m-K for bare LIG to 1.72 W/m-K for LIG foam that is fully infiltrated with P3HT. It is hypothesized that the dramatic increase in thermal conductivity arises from the P3HT's ability to serve as a

bonding agent between broken graphene ligaments, which significantly reduces thermal contact resistances within the graphene foam skeleton.

CHAPTER 1. INTRODUCTION

1.1 Motivation

Thermal management is a growing challenge as manufactures continue to push the limits of power consumption and electronic component packing densities. Power electronic modules are now approaching power densities of 200 W/cm^2 and even relatively low power consumer electronic devices such as smartphones and tablets are experiencing significant thermal management challenges.[1] Moreover, cell phone manufactures are being forced to adopt sophisticated thermal management strategies, as demonstrated by the recent implementation of heat pipes in popular phone brands such as the Samsung Galaxy and the Sony Xperia.

Thermal interface materials (TIMs) are used to mate heat generating and sinking components and often serve as a bottle neck to heat transport away from electronic components. TIMs fill in surface roughness induced microscopic air gaps that occur between mating substrates (even polished hard surfaces have less than 1% contact), _ENREF_2 and they are used to fill larger gaps that occur due to substrate bending and warpage (resulting in noncollinearity) or mismatched design tolerances.[2] Air has a particularly low thermal conductivity (0.026 W/m-K),[3] and any air gaps between adjacent surfaces will significantly increase thermal resistance. As illustrated in Figure 1, the increase in thermal resistance results in the higher device temperature at T_1. By inserting a thermal interface material, air gaps are removed and the thermal resistance decreases, lowering the device temperature to T_2.

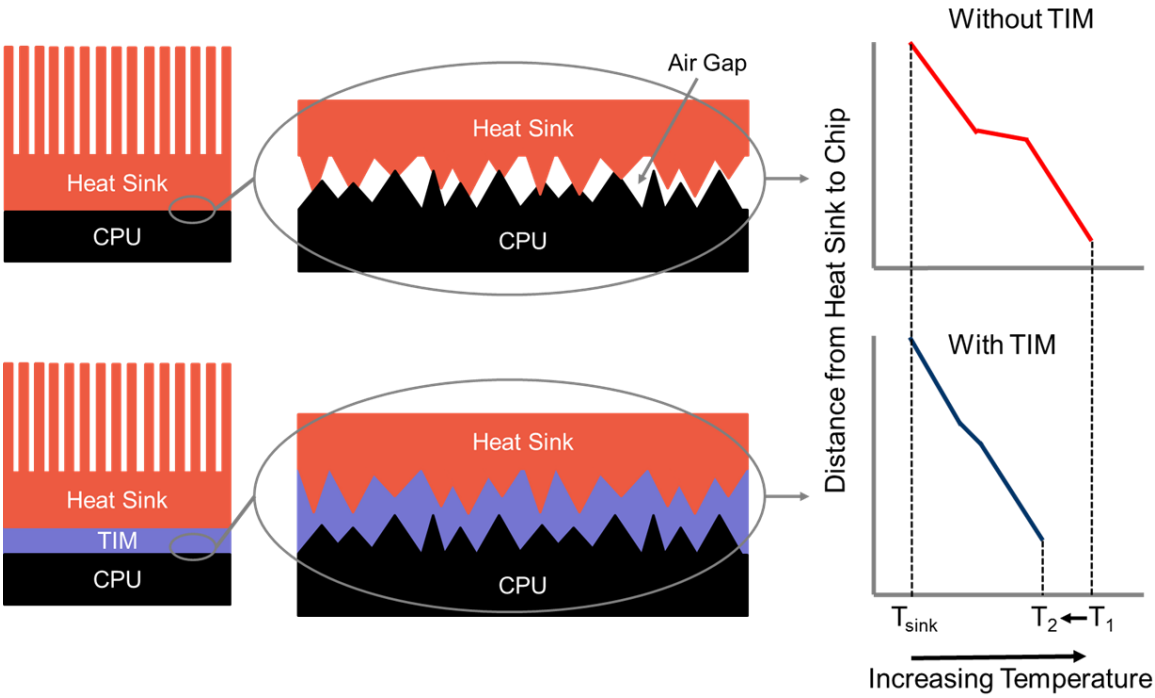

Figure 1. Reduction in chip temperature from T_1 to T_2 upon insertion of thermal interface material.

Although TIMs can significantly reduce the thermal resistance in comparison to a dry bond with no TIM, they still often serve as the bottle neck to thermal transport due to either high contact resistance or low intrinsic thermal conductivity.[4] Moreover, as illustrated in Figure 2, the four contributing factors to the total thermal resistance are the TIM's intrinsic thermal conductivity (K_{TIM}), the bond line thickness (BLT), and the contact resistances between the TIM and the substrates (R_{c1} and R_{c2}). The TIM's total thermal resistance is then equal to the sum of R_{Bulk}, R_{c1}, and R_{c2}.

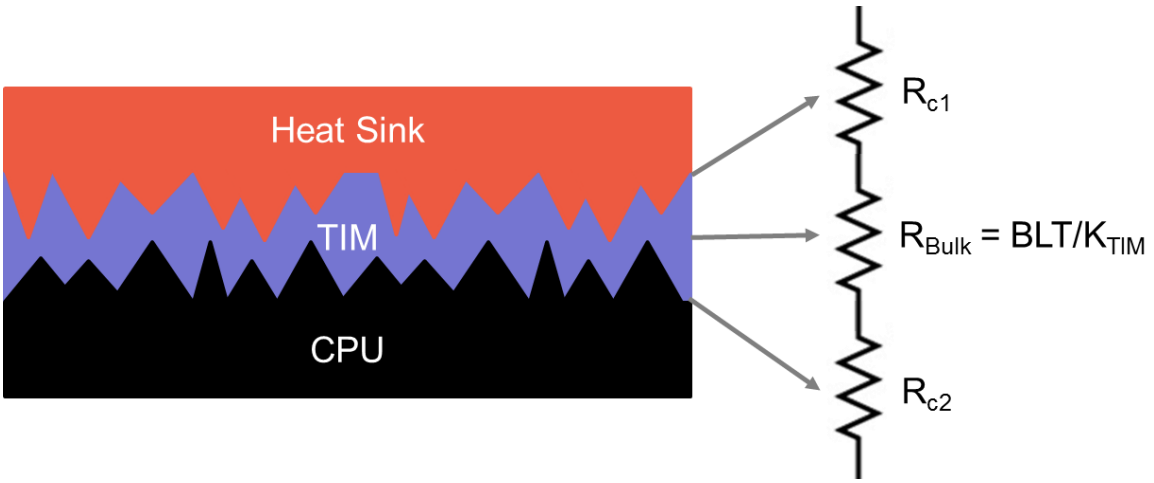

Figure 2. Illustration of the four components that comprise the total thermal resistance of a thermal interface material; the top and bottom contact resistances, R_{c1} and R_{c2}, respectively, and the intrinsic resistance of the bulk TIM, R_{Bulk}.

The minimum achievable BLT is generally governed by engineering tolerances and cannot be manipulated to reduce the total thermal interface resistance. Hence, the primary routes used to reduce resistance are to mitigate the contact resistances or to improve the TIM's intrinsic thermal conductivity. However, achieving high effective thermal conductivity is especially challenging because TIM materials need to be mechanically compliant (shore hardness typically in the A 20-70 range) to account for coefficient of thermal expansion (CTE) mismatches and to fill the microscopic surface roughness voids at moderate bonding pressures.[5] Unfortunately, most naturally occurring high thermal conductivity materials are extremely rigid (non-compliant) and their bonds can only be formed at high temperatures, such as is the case with metal solder.[6]

These dilemmas have resulted in the formation of a projected multi-billion-dollar market (per the 2017 Research and Markets report, "Global Thermal Interface Materials Market Analysis & Trends - Industry Forecast to 2025) for polymer composite based thermal interface materials, which offer both mechanical compliance and high intrinsic

thermal conductivity. Moreover, high temperature (100°C – 200°C) and high performance TIMs can cost up to $1-$10 per square inch, whereas commonly employed materials, such as thermal greases and thermally conducting adhesives, can cost approximately $0.20-$2.00 per square inch (these ranges were determined from the author's experience purchasing and benchmarking TIMs and reflect the current market). Figure 3 depicts the global market for the most widely used thermal interface materials, as reported by BCC Research.

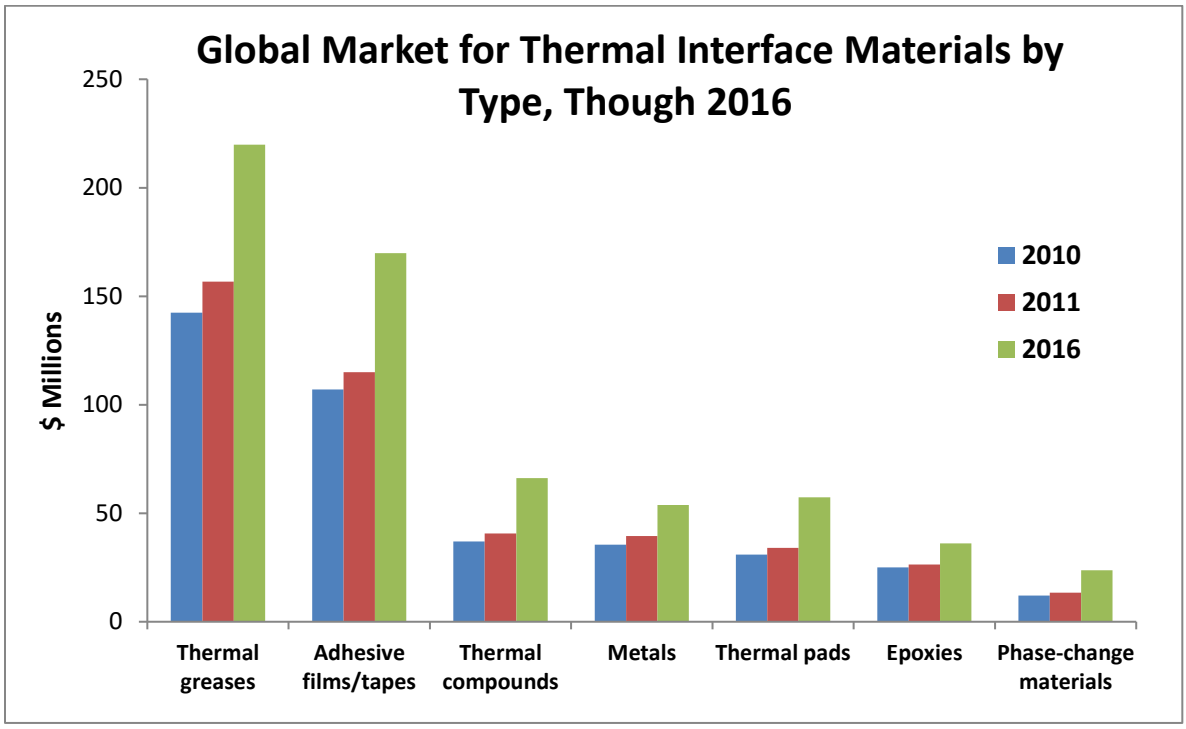

Figure 3. TIM market analysis adapted from a 2011 BCC Research report "Thermal Interface Materials: Technologies, Applications and Global Markets".

Each material exhibits specific properties that can be advantageous for a given application. Greases and phase change materials are commonly used in applications where BLT is below 100 µm, the bond is quasi permanent, and long-term materials degradation

and pump-out is less of a concern.[7] Thermal pads are often thicker (> 100 µm and up to a few mm), can be reworked (non-permanent bonding), and can provide highly reliable long-term performance.[4] Commercially available thermal greases, pads, epoxies, thermal compounds, and phase-change materials primarily consist of a polymer composite material in the form factor of a viscous fluid or thin film ranging from 20 µm to a few mm in thickness. As previously stated, these materials often serve as the bottle neck to heat removal and intense materials research efforts are currently underway to continue to improve the materials effective thermal conductivity.

1.2 Thermally Conductive Polymers

1.2.1 Polymer Composites

Due to extremely low inherent thermal conductivity in bulk polymer films (typically between 0.1-0.5 W/m-K),[8] nearly all polymer based TIMs are comprised of a polymer species with a secondary high thermal conductivity filler dispersed throughout. The polymer is typically a thermoset silicone elastomer, epoxy, silicone oil, paraffin wax phase change material (PCM), or thermoplastic polyurethane (TPU) elastomer.[9-12] The high thermal conductivity filler provides high thermal transport and the polymer matrix provides mechanical compliance. Filler concentration typically ranges from anywhere between 20-70 wt%, where mechanical properties and processability are generally reduced and thermal properties improved with increases in filler wt%.[7, 13, 14] The distribution, size/shape, and orientation of fillers, as well as the surface interaction between the fillers and the polymer matrix, are all factors that contribute to the composite materials thermal

and mechanical properties. Fillers often found in state of the art polymer composites can be broken down into two categories, electrically conducting and electrically insulating.

Electrically conducting filler materials include metal particles and wires,[15] graphene,[16] carbon fibers,[17, 18] and carbon nanotubes,[19, 20] to name a few. Electrically conducting composites manufactured using high thermal conductivity carbon fibers typically result in the highest achievable composite thermal conductivities due to the high intrinsic thermal conductivity and dispersibility of chopped carbon fibers (500-900 W/m-K for carbon fibers, depending on processing).[17, 21, 22] For randomly dispersed filler particles, thermal percolation normally occurs around 40 wt% particle filling and high performance materials require filler concentrations greater than 50 wt%. Alternatively, composites can achieve significantly enhanced thermal conduction at reduced filler concentrations when the particles are aligned in the direction of heat flow.[23-25] For example, Polymatech manufactures high performance TIMs using a process developed by Uetani et al., in which electrostatic force is used to align carbon fibers in a polymer matrix, resulting in directional effective thermal conductivities greater than 20 W/m-K at less than 20 vol% fiber filling.[18] Other state of the art TIM technologies include vertically aligned carbon nanotube forests infiltrated with polymer, which have demonstrated thermal resistances less than 10 mm^2-K/W.[26]

However, certain applications limit the use of carbon based fillers as it is often necessary for TIMs to be electrically insulating and high quality carbon fibers, graphene, and carbon nanotubes can be expensive to manufacture. Some of the most commonly used electrically insulating fillers are aluminum oxide and silicon carbide,[27, 28] as well as boron, aluminum, and silicon nitride.[4, 24, 29-31] Commercially available (excluding diamond based

composites because of extremely high cost) electrically insulating composites with high thermal conductivity typically have peak thermal conductivities below their electrically conducting counterparts because of lower thermal conductivity of filler particles (30-300 W/m-K for boron nitride flakes and 150-220 W/m-K for aluminum nitride).[27] Boron nitride nanotubes (BNNTs) have potential to serve as the graphene/carbon nanotube equivalent for electrically insulating materials, but BNNT research is in its infancy and manufacturing costs are currently prohibitive.[32]

Three-dimensional foams with a thermally conductive skeletal network can overcome the challenge of particle dispersibility and contact resistance between particles in nanocomposite materials, resulting in high thermal conductivity at relatively low vol% conductive species.[33-37] Graphitic and other carbon based foams have demonstrated the highest potential due to high intrinsic ligament thermal conductivity (>1000 W/m-K). For example, carbon based foams have demonstrated extremely high effective thermal conductivity of 40-150 W/m-K for mesophase-pitch derived skeletal carbon structures[38] and up to 182 W/m-K for graphitic structures.[33] Foams are often grown as thin film films through CVD methods and have an ideal form-factor for use as thermal interface materials. Recent works on polymer infiltrated graphene foams have demonstrated extremely low thermal interface resistances of 4 mm^2-K/W[39] for PCM infiltrated composites and 14 mm^2-K/W for GF/PDMS composites.[40] Unfortunately, carbon based foams are often fabricated through high temperature CVD methods where a metal foam is used as a sacrificial growth scaffold, which result in excessive costs for thermal interface applications.

1.2.2 Aligning Polymer Chains

As previously mentioned, bulk polymer films have notoriously low thermal conductivity. However, it is well known that individual polymer chains are capable of extremely high levels of thermal transport, which is lost in the bulk due to system disorder.[39, 41, 42] In general, phonon vibrational modes can easily propagate along the covalently bonded polymer backbone, whereas the weaker interchain van der Waals bonding between chains results in phonon scattering. Hence, improved polymer chain alignment can result in drastically improved thermal transport, without the need for conducting fillers that increase material cost and reduce processability.

Mechanical drawing methods to improve polymer chain alignment and thermal conductivity in polymers were explored as early as the 1970's.[43, 44] Drawing and fiber spinning techniques have continually improved, mostly driven by the market for high strength polymer fibers and films, and a wide variety of materials with greater than 100x the thermal conductivity of their bulk counterparts (15-40 W/m-K range) are commercially available.[45-47] These materials are fabricated from gel- or solution-spinning methods and often require costly processing steps including solvent extraction and multi-stage fiber drawing.[48, 49] In addition, commercial spinning methods result in the formation of microfibers or microfilms, which are still large enough to allow for voids, defects and imperfect crystal and chain alignment, as evidence by their inability to reach theoretical maximum yield stresses which would be expected for ideal crystals with perfect alignment.[50]

Hence, recent efforts have been focused on the fabrication of polymer based nanofibers and in 2010 the remarkable thermal conductivity of ~104 W/m-K was achieved for ultra-draw polyethylene (PE) nanofibers.[51] This drastic increase in thermal conductivity, more than 2x the thermal conductivity of commercial high strength PE microfibers, is attributed to reduced defects inherent to decreasing fiber diameter. This work paved the way for a plethora of publications exploring enhanced thermal transport in melt and solution drawn,[52] electrospun,[53-55] and template fabricated nanofibers[56-58] with enhanced chain alignment and thermal conductivity. Of the proposed methods, template fabrication using nanoporous aluminium oxide (AAO) templates is the only method where chain alignment is achieved "passively" with no external forces required. Preferential polymer chain alignment is attributed to nanoscale confinement effects and shear induced chain alignment that occurs during nanopore infiltration.[57, 59-61] In addition, templating methods are ideal for the application of thermal interface materials, where the resulting fibers take the form of a vertically aligned forest of nanofibers.[56, 62, 63]

1.3 Objectives and Overview

P3HT is one of the most widely studied polymers in the realm of organic electronics due to its ease of processing, promising electrical properties, relatively good stability at high temperatures, and potential for scalability due to straightforward synthesis techniques.[64] In addition, P3HT has the potential to demonstrate high chain thermal conductivity because of its relatively stiff conjugated backbone[39] and may provide improved composite thermal transport due to strong interaction with graphene and CNTs through π-π bonding.[65] Despite these promising properties, there are very few reports of

thermal conduction in P3HT and P3HT/carbon composites and the relationship between processing and thermal transport properties in these systems is relatively unknown.

The goal of this work is to further elucidate the processing, structure, and fundamental thermal transport mechanisms of P3HT nanostructures and carbon based composites for the potential application of thermal interface material. Chapter 2 and Chapter 3 investigates thermal transport in both solution and melt processed P3HT nanostructures, respectively. Chapter 4 explores a novel technique developed to fabricate composite P3HT/CNT fibers in AAO templates and their resulting thermal transport properties are reported. Finally, a recently invented laser induced graphene (LIG) foam[66] is incrementally infiltrated with P3HT and significantly enhanced thermal transport is demonstrated, paving the way for a new class of foam based thermal interface materials. **Table 1** below outlines the materials fabricated, significant findings, and status of public dissemination for each chapter in this work.

Table 1. Outline of the materials investigated, significant findings, and status of public dissemination for each chapter.

	Material System Explored	Significant Findings	Dissemination
Chapter 2	Vertically aligned solution processed P3HT nanotube arrays	• Super hydrophobic P3HT nanotubes surfaces created • Nanotube thermal conductivity of ~1 W/m-K achieved (5x improvement) • Surface thermal contact resistance quantified	Published in *ACS Nano*
Chapter 3	Vertically aligned melt processed P3HT and PE nanofiber arrays	• Highest P3HT nanofiber thermal conductivity achieved (~7 W/m-K) • First demonstration of P3HT nano-fiber chain alignment using Raman • Method to make NF TIM introduced	Published in *Proceeding of ITHERM* and in preparation for *Macromolecules*
Chapter 4	Vertically aligned composite P3HT/CNT nanofiber arrays	• First demonstration of P3HT/CNT composite nanofibers • Highest known filler wt% for templated nanofibers (>20 wt%) • 2x increase to nanofiber conductivity	Published in *ACS Applied Materials and Interfaces*
Chapter 5	Composite P3HT/laser induced graphene (LIG) foam thin films	• First thermal measurements of LIG and P3HT/LIG composite foams • Interesting foam “healing” observed which reduces skeletal thermal contact resistances	Published in *Applied Physics Letters*
Chapter 6	Doubled sided P3HT nanofiber arrays and commercial thermal interface materials	• Successful benchmarking of leading commercial TIMS • Doubled sided P3HT nanofiber array TIMs measured using 1D reference bar	Publication in preparation

CHAPTER 2. POLY (3-HEXYLTHIOPHENE) NANOTUBE ARRAY SURFACES WITH TUNABLE WETTING AND CONTACT THERMAL ENERGY TRANSPORT

2.1 Introduction

High aspect ratio, polymer nanotubes (PNTs) and nanowires exhibit remarkable electrical,[60, 67-69] thermal,[45, 46, 51, 57, 70, 71] and mechanical[48, 72, 73] properties that are attributed to preferential chain alignment and high surface area to volume ratios. Moreover, polymers can be processed quickly at low temperatures, offering the potential of inexpensive, high-throughput manufacturing.[74] These traits make solution-processed polymer nanotubes interesting for many potential commercial applications. For example, polythiophene nanotube array thermal interface materials[71] (TIMs) and polyethylene nanowire arrays[57, 75] that exhibit dramatically improved anisotropic thermal conductivity were recently reported, and there have been multiple reports on the use of vertically aligned, high-aspect-ratio polymer nanotubes to create surfaces with superhydrophobic and tunable wetting properties.[75-79] This study investigates the thermal transport and wetting properties of the polythiophene derivative regioregular poly(3-hexylthiophene) (rr-P3HT) PNT arrays. We choose this polymer because rr-P3HT is stable at high temperatures and can undergo solvation in organic solvents (solution processing) at room temperature, but is stable in aqueous environments.[71] These qualities make rr-P3HT ideal for harsh, high-temperature environments of which TIMs are commonly exposed and the stability in aqueous solutions

is also important for microfluidic applications. In addition, rr-P3HT is commercially available and is commonly used in organic electronic devices, but much less work has been done to investigate thermal transport properties.

For both wetting and thermal interface applications, nanotube arrays are often grown on a substrate where the bottom of the array is anchored and the other end consists of free tips. Due to wet processing conditions and because the densely packed tubes have high aspect ratios, the vertical arrays have the tendency to bundle and aggregate during processing through elastocapillary coalescence.[75, 76, 79-84] Elastocapillary coalescence occurs when capillary forces cause objects to elastically bend into contact with each other upon which the objects stick together through cohesion. Nanotube aggregation can dramatically alter the surface morphology and the corresponding interactions between the PNT array and a contacting liquid or substrate. For example, capillary effects can result in a surface with microstructures comprised of smaller nanostructures, achieving a hierarchical arrangement similar to surfaces often found in nature and that are known to display special wettability.[75, 85, 86] Although nanotube array surface morphology has been proven to influence surface wetting properties,[78, 79, 84, 87-89] no prior reports are found that correlate the degree of aggregation to the contact thermal energy transport of PNT array interfaces. Understanding this relationship is critical, because despite their high intrinsic thermal conductivities, thermal contact resistance (TCR) has been a major limitation of high aspect ratio structures such as carbon nanotube (CNT) array TIMs.[90-92] In addition, the favorable mechanical properties and strong adhesion of soft materials,[73] as compared to CNTs, further supports the hypothesis that PNTs could potentially reduce the high contact resistance associated with traditional nanotube interfaces. However, prior methods

to fabricate high aspect ratio nanostructures with tunable surface morphology and, thus, surface properties, are still relatively complex,[78, 79, 84, 87-89] often relying on lithographic processes, special drying conditions, or varying structure dimensions, so there is a need to develop simple approaches.

Here, a simple solution-based nanoporous template wetting technique[59, 61, 93] is replicated to fabricate rr-P3HT nanotube arrays, but the template etching process is modified to easily alter the array surface morphology as a function of released nanotube length. Distinct surface morphologies are then characterized by measuring their surface fractions and the surface fractions are correlated to the wetting and thermal transport properties. Additionally, the water contact angle (WCA) and contact angle hysteresis (CAH) are measured and array surface fractions are used to compare the measured surface wetting behavior to the theoretical Cassie-Baxter relationship.[94] In order to elucidate the relationship between array morphology and TCR, the photoacoustic method[90] (PA) is used to measure the change in the TCR as a function of the surface fraction. The PA technique is also used to measure array thermal conductivity as a function of morphology and to measure the improvement in thermal conductivity due to nanoscale confinement.

2.2 Fabrication and Structure of P3HT Nanotube Arrays

2.2.1 Nanotube Array Processing

A solution consisting of 2 mg/ml rr-P3HT dissolved in chlorobenzene was cast onto 60 μm thick nanoporous anodic aluminum oxide (AAO) templates with an estimated porosity of 40-50% and rated nominal pore diameter of 200 nm. The polymer solution infiltrated the nanopores spontaneously driven by wetting phenomena[61] and the solvent

was removed in ambient conditions through evaporation (Figure 4a step 1). After solvent evaporation, the infiltrated AAO-polymer composite structures were exposed to a 1 M KOH solution to remove the alumina and partially free the nanotubes (Figure 4a step 2). Partial template etching was achieved by placing a small drop on the surface of the AAO and therefore only exposing one side of the template to etchant. The longer the etch time, the greater the length of exposed nanotube and degree of nanotube clustering (Figure 4a step 3a-c).

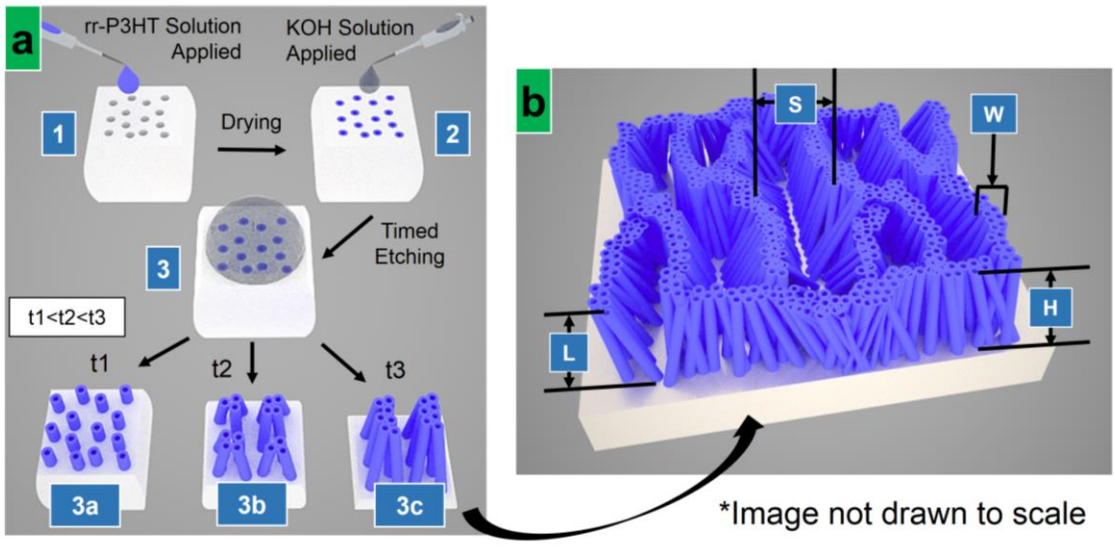

Figure 4. Solution process to fabricate arrays of vertically aligned polymer nanotubes and nanotube bundles. In step 1 of Figure 4a, the AAO nanoporous template is wetted with rr-P3HT solution. After drying, KOH is pipetted on top of the template to begin the top-down template etching process (step 3). For steps 3a, 3b and 3c, the increase in bundle size as the etch time increases from t1 to t3 is illustrated. Figure 4b highlights the formation of ridges for large surface area, densely packed nanopolymer arrays where S is the spacing between ridges, L is the nanotube length, H is the array height, and W is the ridge width.

A JEOL 100CX II transmission electron microscope (TEM) operating at 100kV was used to perform nanotube structural characterization on individual polymer nanotubes. As illustrated in Figure 5a-b, the resulting nanotubes had 150-300 nm diameters with wall thicknesses ranging from 20-40 nm. It was determined that their exact geometries vary due to template inconsistencies including variations in pore diameter, as illustrated in the scanning electron image of the AAO template pictured in Figure 5d.

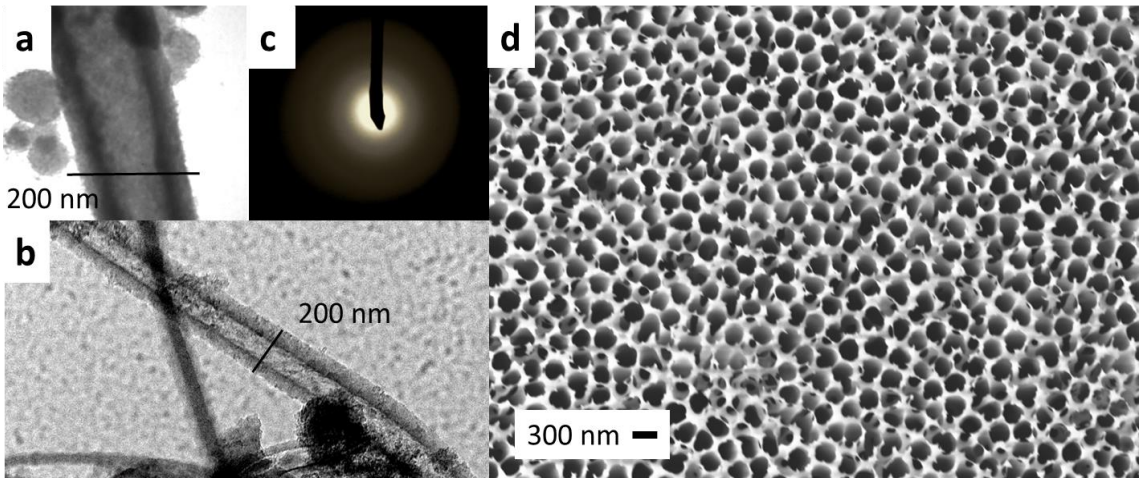

Figure 5. Images a and b are transmission electron micrographs of poly(3-hexylthiophene) nanotubes showing the variation in tube diameter and wall thickness. Image c displays a transmission electron diffraction pattern obtained for the nanotube pictured in image a and the scanning electron micrograph (image d) depicts the surface and pore diameter non-uniformity of the AAO templates as purchased from Whatman (200 nm nominal pore diameter). These templates are nominally rated to have 200 nm pore diameters; however, it is widely known that Whatman templates have a bell-shaped pore distribution with a measured mean pore diameter of ~230 nm.[95]

When the process in Figure 4 is applied to large area, high-density arrays of PNTs, interconnected ridges form that exhibit a constant width (W) (width becomes constant after

6 minutes of etching). However, the characteristic spacing between ridges (S) increases dramatically as the exposed nanotube length increases as illustrated in Figure 6. The ridge spacing parameter (S) and the ridge width parameter (W) are illustrated in Figure 4.

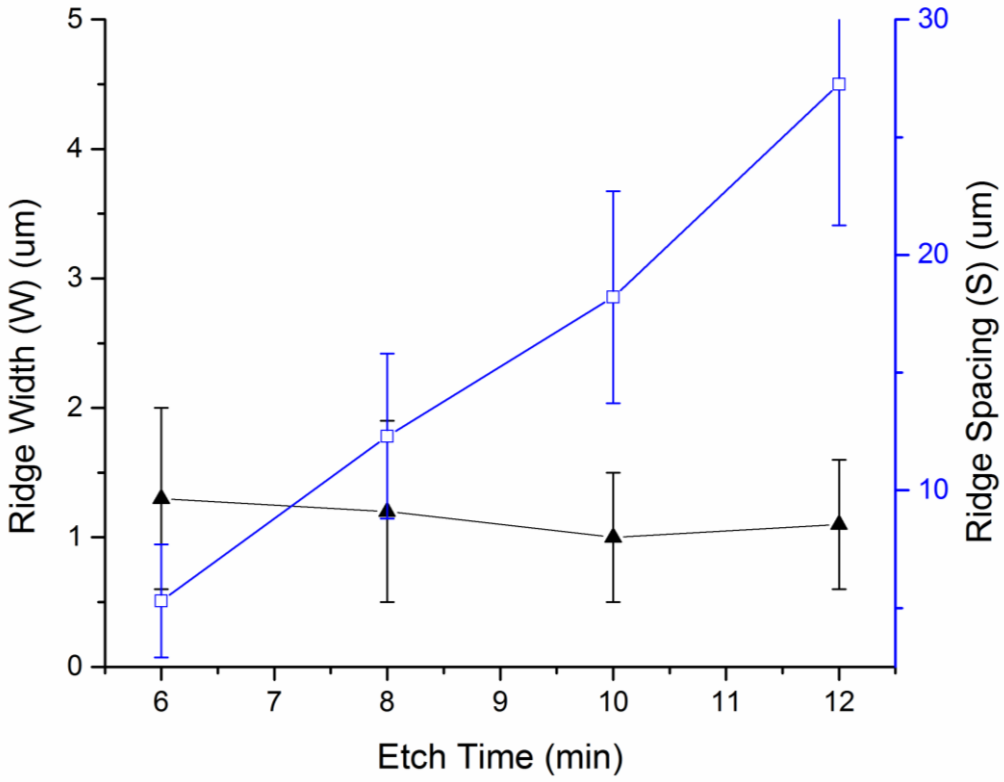

Figure 6. Ridge width (W) and ridge spacing (S) plotted as a function of etch time.

2.2.2 Nanotube Array Surface Morphology

In contrast to prior studies that focus on the nanostructure bundle size,[87, 88] it was found here that the ridge spacing directly relates to the surface fraction, which can be used to estimate wettability, assuming Cassie-Baxter behavior.[94] To fabricate several surfaces with unique and reproducible surface fractions, the etch time was varied from 2 to 12 minutes at 2 minute intervals. By placing the etchant drop so that it only contacted the top surface of the template, the length of freed nanotubes and the corresponding surface morphology of the PNT array was precisely controlled as illustrated in Figure 7a-f.

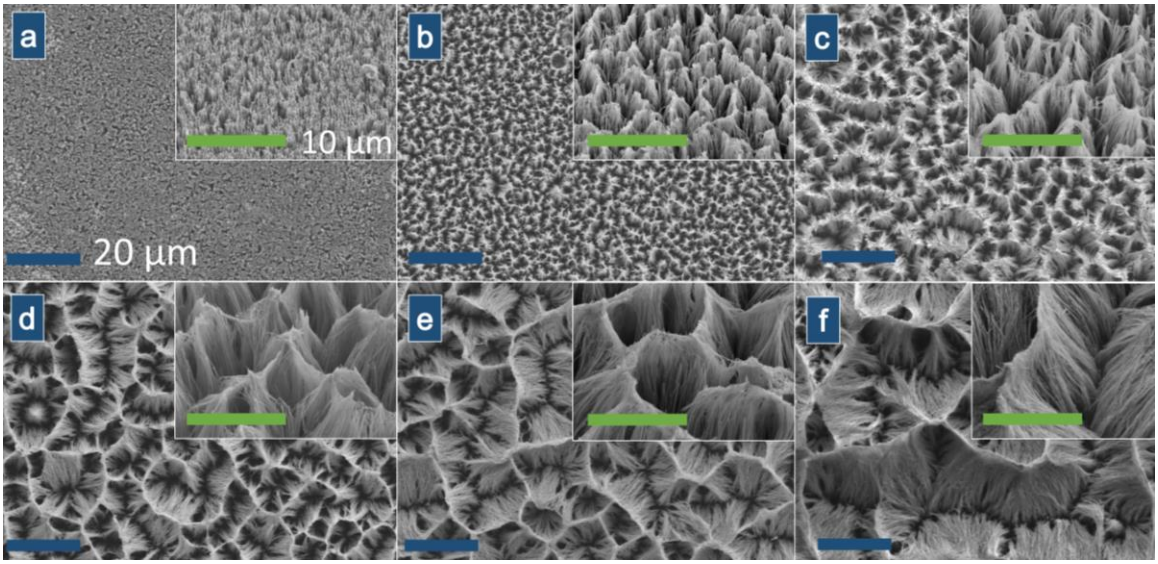

Figure 7. Scanning electron micrographs a-f represent the change in the surface morphology as the AAO etch time increases from 2 to 12 minutes at 2 minute intervals, respectively. The insets show the corresponding surfaces at an increased magnification. Scale bar 20 µm (inset 10 µm).

As the etch time is increased, the length of the exposed nanotubes and the degree of capillary driven bundling increases, resulting in distinct ridge formation. The ridging effect occurs when the elastocapillary forces pull the nanotubes together, and once capillary

forces are not present (i.e. after evaporation of the wetting agent), the nanotube clusters are preserved through inter-tube cohesion.[89] The initial clustering (of individual PNTs) and then subsequent bundling of clusters into ridges is driven by an imbalance between the bending stiffness of the PNTs and the capillary force that arises between PNTs, where the capillary force is greater than the nanotube bending stiffness. The capillary force is driven by the intramolecular forces between the liquid and the PNT surface (due to the interfacial surface energy) and the surface tension of the liquid. As etch time increases, the relative stiffness of the PNTs and PNT clusters is reduced allowing for increased deformation. For vertically aligned nanotube arrays, the relationship between nanotube length (*L*) and the number of nanotubes per bundle (*N*) has been approximated using a force balance equation (Equation 1) where the number of nanotubes in a discrete cluster is a function of the cube of the nanotube length and is inversely related to the Young's modulus.[87, 89]

$$N \approx \frac{E_C}{E_E} \approx \frac{\gamma_{la} L^3 \cos^2 \theta_0}{D\ (p-D)^2 E} \tag{1}$$

In Equation 1, E_C is the capillary interaction energy, E_E is the elastic energy of the tube, γ_{la} is the surface tension between the liquid and air, *D* is the diameter of the tube, *p* is the distance between the tubes, θ_0 is the equilibrium contact angle of a liquid on the surface of the tubes, E is the tube's Young's Modulus, and L is the nanotube length. In the present experiment, the nanotube length changes significantly as etch time increases, and consequently, tube clustering is predicted to increase dramatically due to the corresponding reduction in stiffness. However, instead of the discrete clusters predicted in Equation 1 and observed in previous studies,[87, 89] percolating ridges of PNTs form, and a close examination

of Figure 7 reveals that these ridges are present even at the shorter etch times (inset of Figure 7b). As illustrated in Figure 8, Equation 1 predicts extremely large cluster sizes and is not valid for this type of material system. For example, Equation 1 and a range of nanotube elastic moduli values (as illustrated in Table 2) were used to predict the degree of clustering for the 8 minute etched sample and found that the predicted bundle size is nearly 15,000 nanotubes for an assumed moduli of 1 GPa[96] (Figure 8). Although the percolating ridges could contain this large number of tubes, the surface clearly has much finer features as illustrated in the inset of Figure 8.

Table 2. Parameters used to predict nanotube clustering for the 8 minute etch time.

$\gamma_{l\ (mN/M)}$	*D (nm)*	*p(nm)*	θ_0 (degrees)	E (GPa)	*L (μm)*
73[87]	200	30	102° ± 2°	0.5 - 100	17.6

Additionally, the inset image in Figure 8 allows for an approximation of the maximum number of nanopores on a 30 μm by 30 μm surface of approximately 720 200 nm diameter nanopores. On the contrary, the model predicts that cluster sizes of over 500 nanotubes are expected even for tubes with elastic modulus above 10 GPa, which indicates that if the model fit this system the nanotube surface shown in the inset would be one large nanotube cluster and would provide a poor representation of the actual surface structure. The deviation from predicted clustering behavior at increased aspect ratios is attributed to the

relatively low elastic modulus of polymer nanotubes as similar behavior has been observed in other high aspect ratio systems.[97]

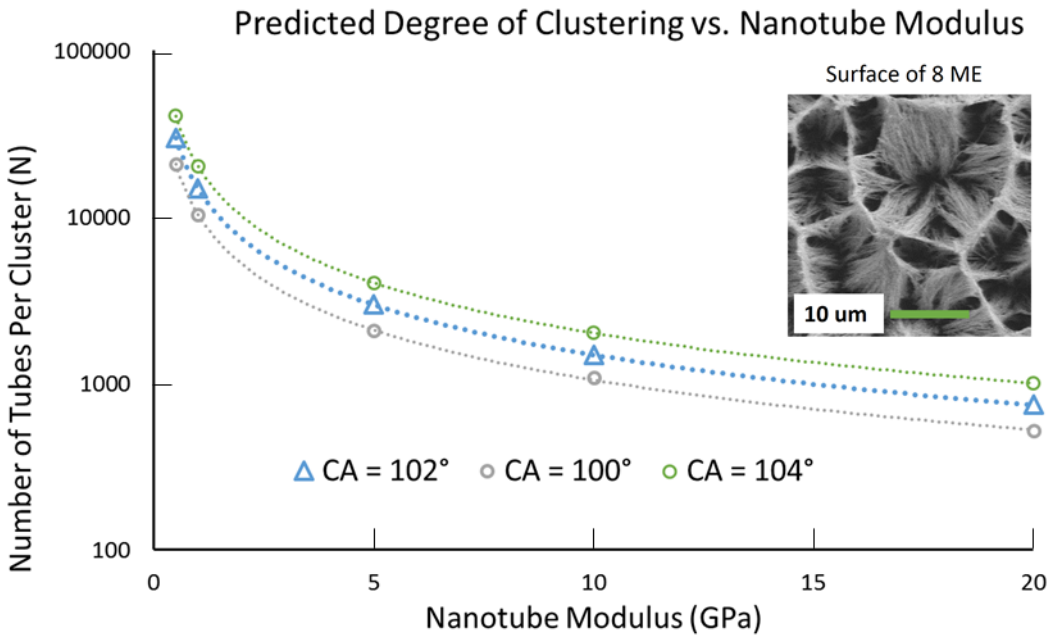

Figure 8. The predicted clustering behavior as a function of nanotube modulus calculated using Equation 1 and the parameters in Table 2. Each line represents the calculations assuming a Young's contact angle of 102° for the blue triangles, 104° for the green circles, and 100° for the grey circles. The inset SEM image represents a 30 µm by 30 µm section of rr-P3HT surface after an etching period of 8 minutes. Assuming a porosity of 50% and pore diameter of 200 nm the maximum number of nanopores over the inset surface area is estimated to be approximately 720.

It was found that the surface fraction of the PNT array decreases as etch time and ridge formation increases, in contrast to earlier studies that have found an increase in surface fraction with increasing Cu and Si nanowire bundling.[78, 87, 88] For etch times of 6 minutes and longer, there is no measurable change in the width of the PNT ridges while the spacing between the ridges increases considerably (Figure 7). Here, a SEM contrasting

method[87] is used to determine the surface fraction, *f*, as a function of etch time where heavily contrasted images were used to attain pixel counts for the ridged regions only. In Figure 9a-d, the ridges were traced to clearly illustrate ridge widening as the etch time increases from 6 to 12 minutes, respectively, and Figure 9e-h show the corresponding percolation ridge traces. The surface fraction, *f*, is reduced from 0.20 ± 0.02 for the 6 minute etch time to a minimum of 0.06 ± 0.01 for the 12 minute etch time.

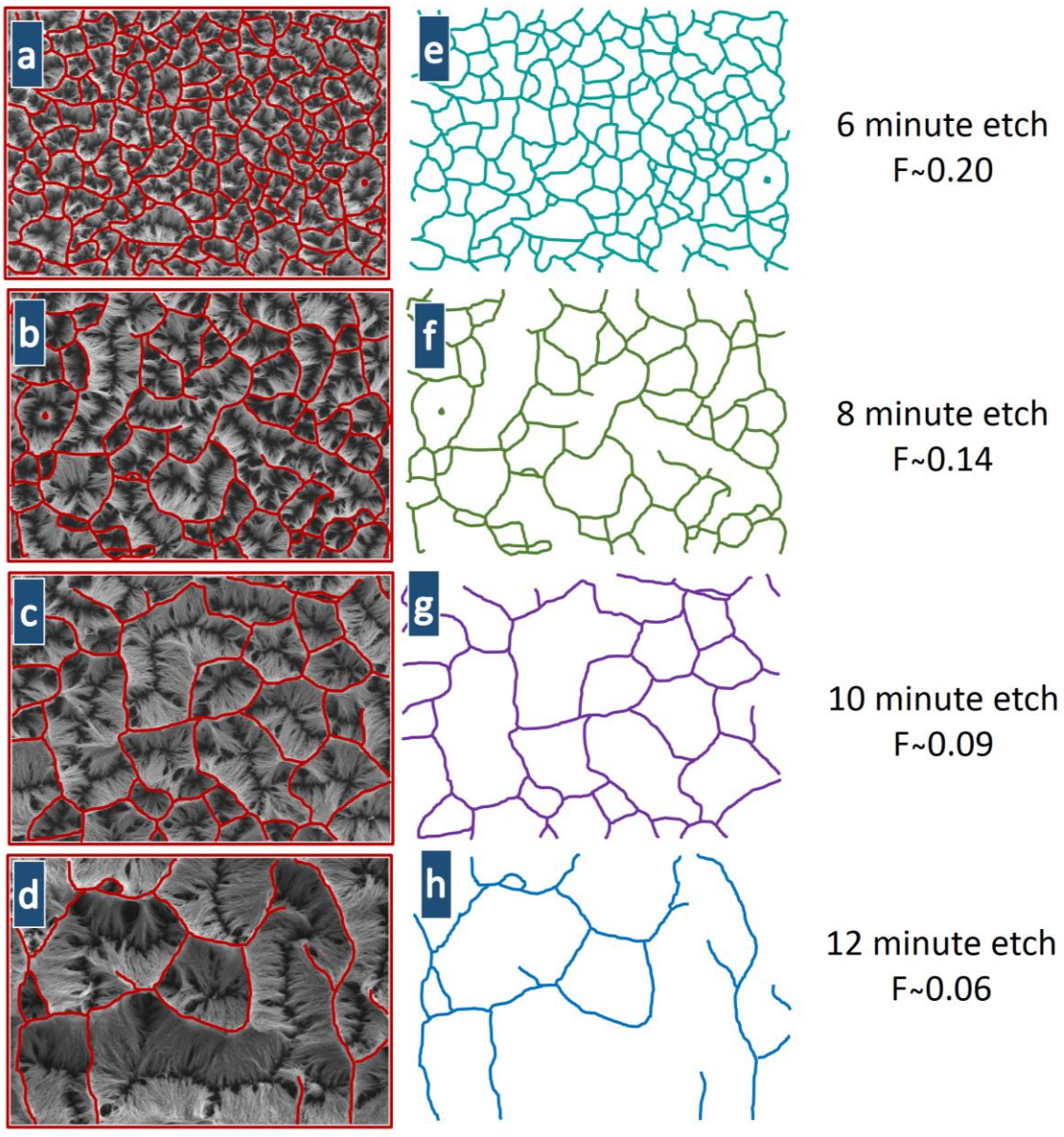

Figure 9. Scanning electron micrographs (a-d) illustrate the ridge tracing method as the etch time increased from 6-12 minutes at 2 minute intervals, respectively. Images (e-h) demonstrate the corresponding ridge trace areas and their calculated surface fractions, *f*.

The relationship between etch time and surface fraction appears to be non-linear since the magnitude of change in surface fraction decreases with etch time. Figure 10 presents the measured surface fraction as a function of etch time. The change in surface fraction from the 2 to 4 minute etch times is approximately 0.08 whereas the change in surface fraction from the 10 to 12 minute etching is approximately 0.03. The uncertainty varies from ± 0.02 for the 2 and 4 minute etch times, to ± 0.015 for the 6 and 8 minute etch times, to ± 0.01 for the 10 and 12 minute etch times and was determined by calculating the standard deviation of 10 measurements taken at 5 different spots on 2 similarly etched samples.

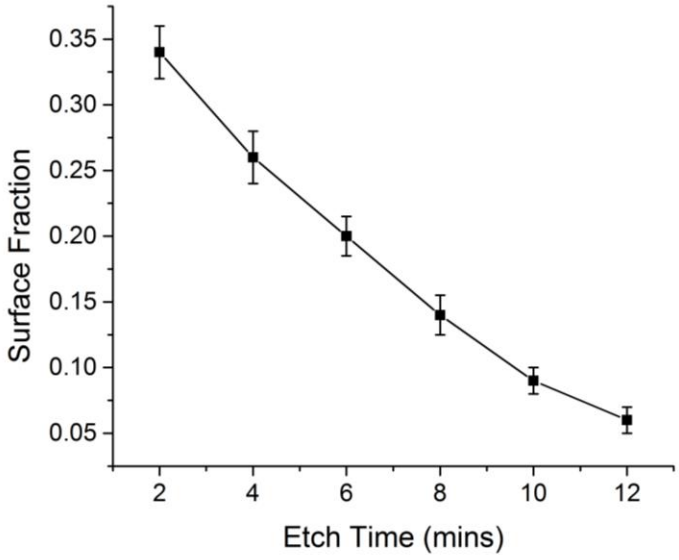

Figure 10. Poly(3-hexylthiophene) nanotube array surface fraction as a function of etch time.

A modified force balance equation was introduced to present a simple relationship between Equation 1 and a more useful parameter for this study, the surface fraction, *f*. Equation 2 is a semi-empirical expression that combines the theoretical force balance

equation (Equation 1), and the trend in the experimental data, to predict the surface fraction, *f*, where

$$f \approx \sqrt{500/N} \tag{2}$$

Here, *N* is the number of nanotubes per cluster as predicted using Equation 2 and 500 is a fitting constant. It is worth noting here that N is infinite in the real system, this is simply an empirical relationship to estimate surface fraction using Equation 1. This simple relationship agreed well with measured surface fraction values for etch times of 8 minutes and greater as demonstrated in Figure 11. In addition, Figure 11 illustrates the relationship between measured and theoretical surface fraction for the 6, 8, 10, and 12 minute etched samples over the bounding uncertainties associated with the contact angle measurement.

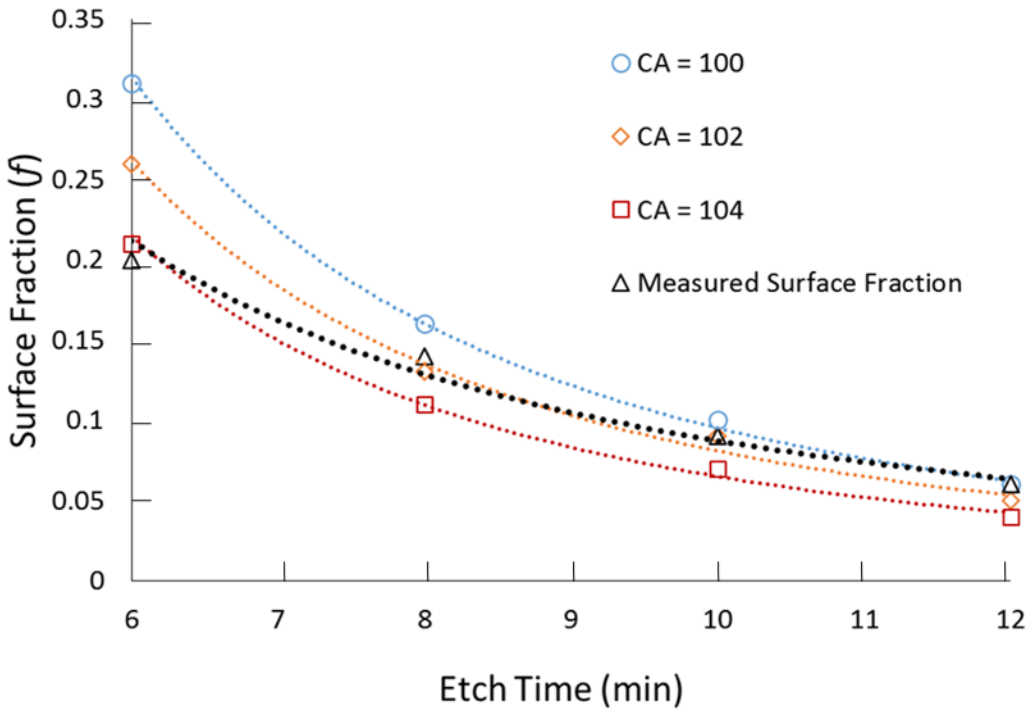

Figure 11. Predicted surface fraction calculated using Equation 2 assuming a nanotube elastic modulus of 0.5 GPa and a contact angle of 100°, 102°, and 104° to account for bounding uncertainties in the rr-P3HT film contact angle measurement. The measured surface fraction is represented by the triangle markers and black line.

Figure 12 illustrates a simple model to explain the morphological changes the surfaces undergo due to alterations to the partially released nanotube length. As the etch time increases, the length of exposed nanotube increases, and the elastic force required to bend the nanotubes is reduced.[83] At the early stages of the etching process, the nanotube tips bend together, and wide ridges form where the tip clusters are joined (Figure 12b). As the etch time increases further, the ridges continue to add additional nanotubes and they become more densely packed forming sharp ridge peaks (Figure 12c). The sharp ridges grow further apart and eventually begin to flatten and collapse into each other as they become more isolated (Figure 12e).

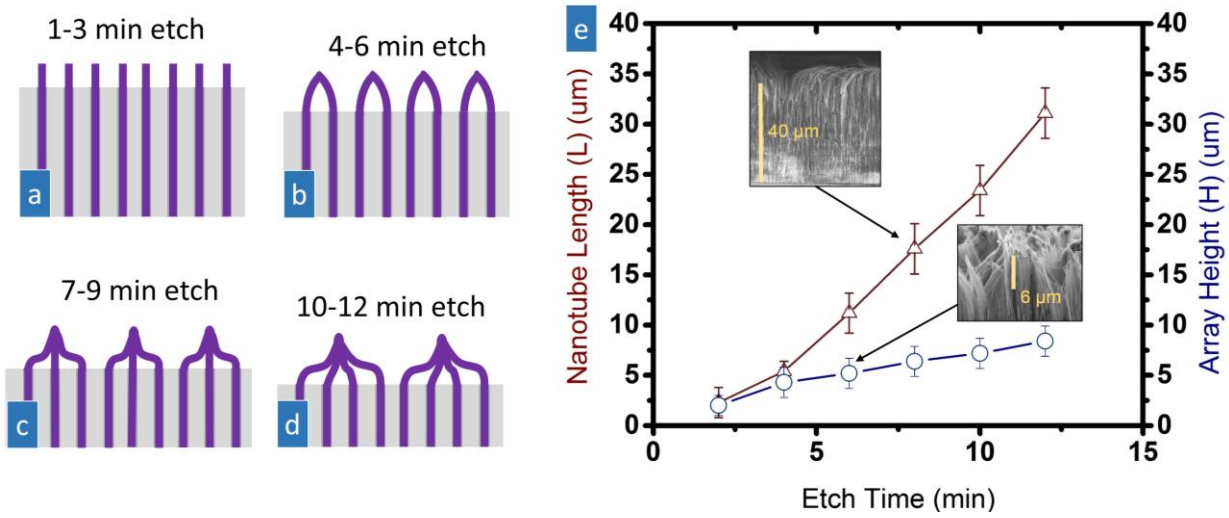

Figure 12. Illustrations a-d represent a simple model used to explain the formation of ridges and the increase in spacing between ridges with increasing etch times. Graph e illustrates the relationship between the length of exposed nanotube and the array height as the etch time increases. The blue circles represent H and correspond to the array height axis whereas the red triangles represent L and correspond to the nanotube length axis. The top inset depicts a cross sectional measurement of the template thickness after 8 minutes of etching and the lower inset is a cross sectional measurement of the nanotube array height after 6 minutes of etching. H and L were measured at 10 different locations along the sample cross-section and the uncertainty is a measure of the standard deviation of those measurements.

Throughout the etching process the relationship between array height (*H*) and the nanotube length (*L*) is also changing and as shown in Figure 12e. As the etch time increases at discrete 2 minute increments, the exposed nanotube length increases nearly linearly and the thickness of the etched alumina template decreases with time (at a rate of approximately 6 µm per 2 minute interval). Conversely, the array height first increases significantly and then begins to plateau and further etching past the 12 minute mark will eventually produce a collapsed mat of PNTs. Cross-sectional SEMs of the etched AAO templates (

Figure **12**e insets) were used to measure the change in nanotube array height and nanotube length. The height of exposed PNTs was also measured with tapping mode atomic force microscopy (AFM) (Figure 13) to confirm estimates from SEMs.

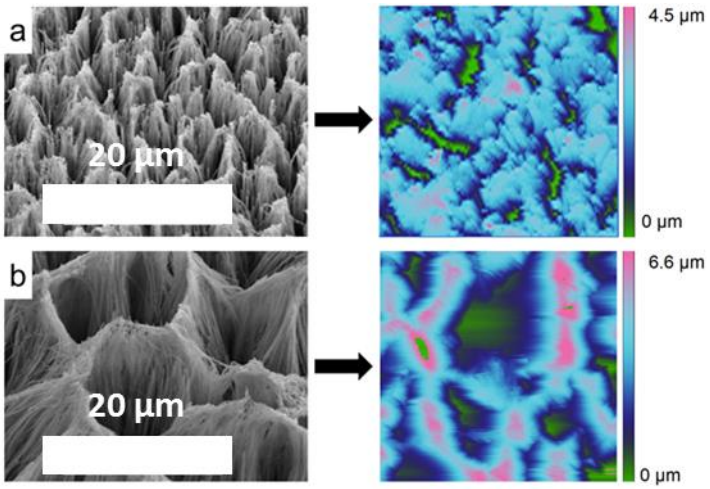

Figure 13. SEM and Atomic Force Microscopy (AFM) measurements depicting the array heights as a function of etch time for an etch time of 4 minutes (SEM Image a) and 10 minutes (SEM Image b). The AFM measurements were used to verify the array height and nanotube length measurements collected using the cross-sectional SEM images.

2.3 Surface Wetting Behavior of P3HT Nanotube Arrays

In general, surface wetting properties depend on the surface texturing and the intrinsic wetting properties of the material. If a smooth surface exhibits a contact angle (CA) greater than 90°, then the Cassie-Baxter (CB) model may predict the apparent CA of the textured version of this surface using the resulting surface fraction, *f*.[94] The apparent CA of the textured surface can be substantially larger than the smooth surface CA because

the wetting fluid may rest upon the surface peaks with air pockets trapped between the peaks and below the fluid. For example, after etching of 4 minutes or longer, we observed contact angles greater than 150° and posit that the wetting fluid rests on top of a composite surface consisting of rr-P3HT ridges and air. However, this wetting behavior was only observed after thermal treatment of the nanotube arrays (templates were placed on a hot plate at 250°C with the exposed nanotubes facing up for 10 seconds (the actually temperature reached by the nanotubes is unknown, but likely lower than 250 °C) and then rapidly cooled under ambient conditions), otherwise the surface contact angle is ~0°.

The thermally induced transition from wetting to non-wetting is likely due to thermal reconstruction effects where the polymer chains at the nanotube surface undergo accelerated compositional or conformational changes.[98] The nanotube surface will accumulate polar species as the n-hexyl side chains and sulfur species undergo radical oxidation in air upon drying.[99, 100] However, thermodynamically driven diffusion and chain conformational changes may redistribute the polar species away from the surface during heating, rendering the surface more hydrophobic. Therefore, the observed improvement in hydrophobicity suggests that the heating conditions used lead to molecular reorganization at the surface (including other segregation effects that may result in changes to surface energy) without reintroducing a significant level of surface oxidation. To support this, we measured the contact angle of 20 μm thick P3HT films processed under nitrogen atmosphere (102° ± 2°) and films fabricated under ambient conditions (94° ± 2°) where partial oxidation is expected. The contact angle of the partially oxidized films is near the 90° boundary between being hydrophobic and hydrophilic and this may explain the dramatic shift in nanotube wettability after heating. Future work should incorporate

EPS or other analytical methods to elucidate chemical changes. In addition, a change in the mechanical properties of the surface structures that prevents the release of capillary driven ridging upon rewetting may also contribute to the improved hydrophobicity (i.e. the water releases cohesive forces).[89] This change in surface mechanics may be attributed to a change in polymer crystallinity (due to rapid annealing on hot plate), which could enhance the tubes elastic modulus,[101] or lead to a nanotube welding phenomena where interdiffusion occurs at temperatures above Tg. The surfaces were imaged before and after thermal treatment and there was no detectable change in morphology, so the wetting transition is likely a direct result of either the thermal reconstruction, the thermal sintering effect (interdiffusion), or a combination of both.

The CA of a DI water drop on a smooth rr-P3HT film processed under nitrogen atmosphere measured ~102°, whereas the CA for 8 to 12 minute etched rr-P3HT nanotube arrays measured greater than 150°. The CA variations of a CB wetting system are dependent upon the surface fraction and can be described by[94] Equation 3 per follows;

$$\cos(\theta^*) = -1 + f(\cos(\theta_0) + 1) \qquad (3)$$

where θ* is the apparent CA that results from structuring, θ_0 is the contact angle on a smooth surface, and f is the surface fraction. However, it is important to note that this model is rather simplistic and other explanations for surface wetting are introduced below. Another important wetting property is the contact angle hysteresis (CAH), which is a measurement of the difference between the advancing contact angle (ACA) and receding contact angle (RCA) (CAH = ACA – RCA). The static contact angle was measured by

dispersing a 2 µl drop of water on the poly(3-hexylthiophene) nanotube array surface. The advancing and receding angles were measured by placing the dispensing needle near the sample surface and dispensing excess water or retracting the water, respectively. All three CA measurements are illustrated in Figure 14.

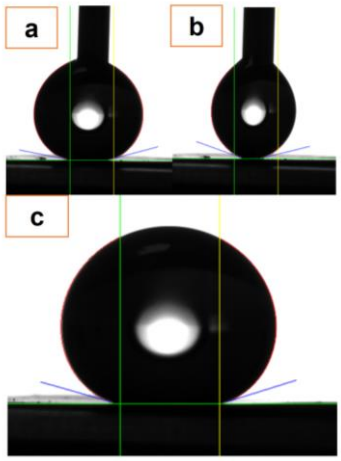

Figure 14. Measurement of the advancing (image a), receding (image b), and static (image c) water contact angles on the 10 minute etched surface.

The CAH quantifies the adhesiveness of a surface to a wetting fluid – the larger the CAH the more adhesive the surface is to that fluid.[94] The CA and the CAH as a function of template etch time as well as the CA values predicted using the CB model (using the experimentally determined surface fractions and the measured rr-P3HT film CA of 102°) are shown in Figure 15. The CA for the 2 minute etched surface is not included in Figure 5 because it was the only surface to demonstrate a contact angle well below the bulk P3HT film CA of ~102°. This finding suggests that the CA of the 2 minute etched surface is biased by wetting fluid interactions with the hydrophilic AAO surface.

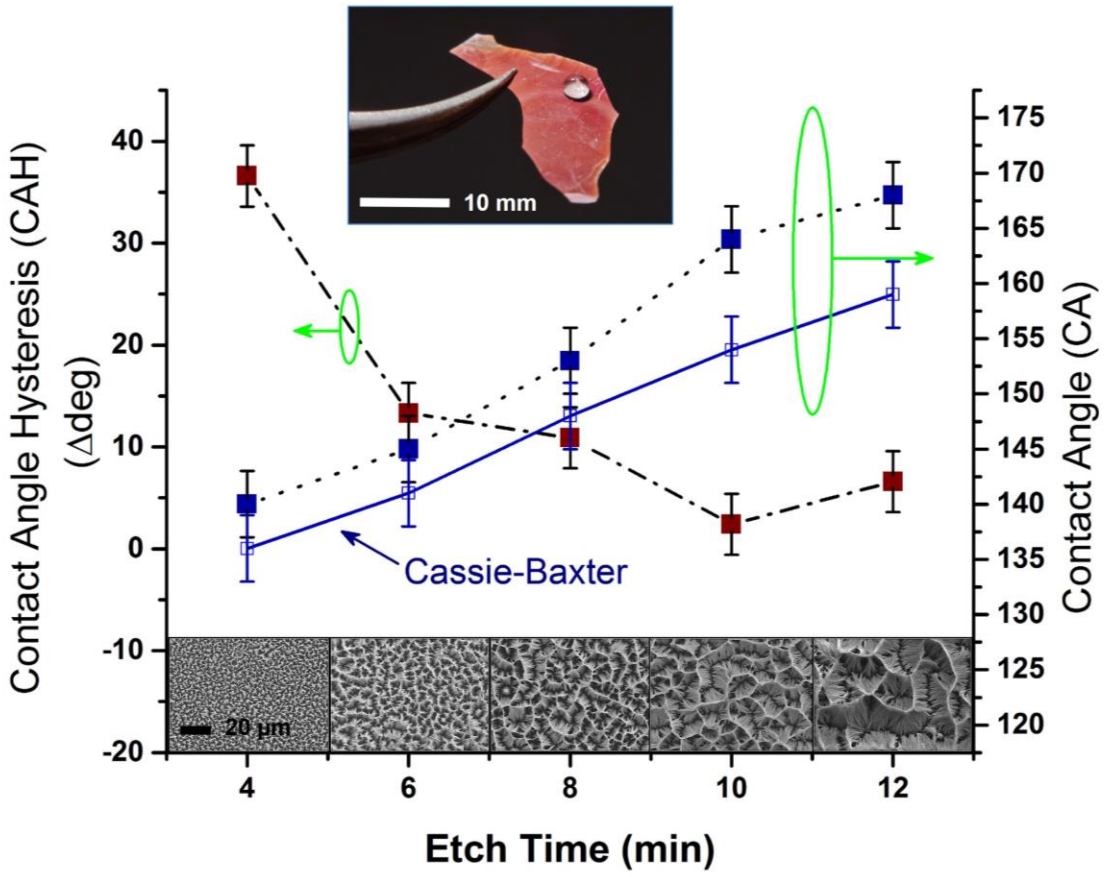

Figure 15. The top inset shows the superhydrophobicity exhibited by the 10 minute etched surface. The graph depicts the surface wetting properties as a function of increasing etch time from 4 to 12 minutes. The red squares correspond to the contact angle hysteresis (CAH) axis, the blue squares correspond to the contact angle (CA) axis, and the solid blue line with open squares represents the theoretical CB contact angle calculated using the measured surface fractions and the intrinsic CA of 102° and also corresponds to the CA axis. The inset images along the x-axis illustrate the changing surface morphology as the etch time increases from 4 to12 minutes at 2 minute intervals. The measurement uncertainty was derived from the standard deviation of 9 total measurements where 3 measurements were taken at three different spots on the sample surface.

A surface is superhydrophobic when its CA is greater than 150° and CAH is less than or equal to 10°.[102] As shown in Figure 15, the surfaces associated with 8, 10, and 12 minute etch times can be classified as superhydrophobic, where the maximum contact angle achieved is nearly 170° for the 12 minute etch time and the lowest hysteresis is less than

5° for the 10 minute etch time. The CA results correlate well to the Cassie-Baxter relation; a small surface fraction produces a large CA and a large surface fraction produces a smaller CA. The largest deviations from the model occur at the lowest surface fractions (i.e., longest etch times), but even at these values the experimental results are within 10° of the calculated values. The deviation from the CB model is likely due to the hypothesized partial oxidation of the nanotube surfaces, uncertainty in measuring the true surface fraction and intrinsic CA, and shortcomings of the CB model. The validity of the CB model is a current point of debate in the literature and works by Gao and McCarthy[103, 104] and Extrand[105] suggest that the model fails to accurately predict the apparent contact angle on a textured surface. In particular, the CB model fails to accurately predict CA and CAH when applied to surfaces with spatially heterogeneous asperities and recent works have attempted to modify the CB model for improved robustness.[106] However, an elementary CB comparison is useful here because it validates the predicated interaction between the surface and droplet and demonstrates the impact of inhomogeneous surfaces.

2.4 Thermal Contact Resistance and Conductivity of P3HT Nanotubes

2.4.1 Photoacoustic Characterization

We used the photoacoustic (PA) method to determine the array thermal conductivity, and the thermal contact resistance (TCR) between the tips of the rr-P3HT nanotubes and a surface as a function of the etch time. In brief, the PA method works by heating a sample with a modulated laser and as the sample surface temperature rises, heat is conducted into the surrounding gas and down into the sample. The thermal expansion

and contraction of heated gas results in the propagation of acoustic waves throughout the chamber. The amplitude and phase shift of the acoustic waves (as a function of laser modulation frequency) can be compared to that of a known reference sample in a 1D heat flow model and the multiple unknown material properties can be fitted to a theoretically generated curve using a non-linear fitting algorithm. The chamber is often pressurized with helium to increase the signal strength (helium has higher thermal conductivity than air) and to control contact pressure at an interface.[90]

Moreover, the photoacoustic (PA) technique has been used previously to measure nanostructure sample layer resistance[91] and polymer nanotube array thermal conductivity[71] and both measurement techniques are described in detail in the cited works. The laser used in this study is an 1100 nm continuous-wave fiber laser and the modulation frequency range was held at 300 – 4000 Hz to adequately measure the desired properties without penetrating through to the quartz layer. The acoustic fitting was carried out using the Levenberg-Marquardt method within a 1D heat flow model developed by Hu *et al*.[107] Only the acoustic phase data was used in the heat flow model because it has been demonstrated previously that the phase data, as opposed to wave amplitude data, provides more reliable measurements.[108] The sample configuration used to probe the nanotube array thermal conductivity is demonstrated in Figure 16a and the configuration used to probe the layer resistance is depicted in Figure 16b. The top Ti-Ag foil was used to measure thermal contact resistance between the nanotube tips and the contacting Ag surface and was removed when measuring the nanotube thermal conductivity.

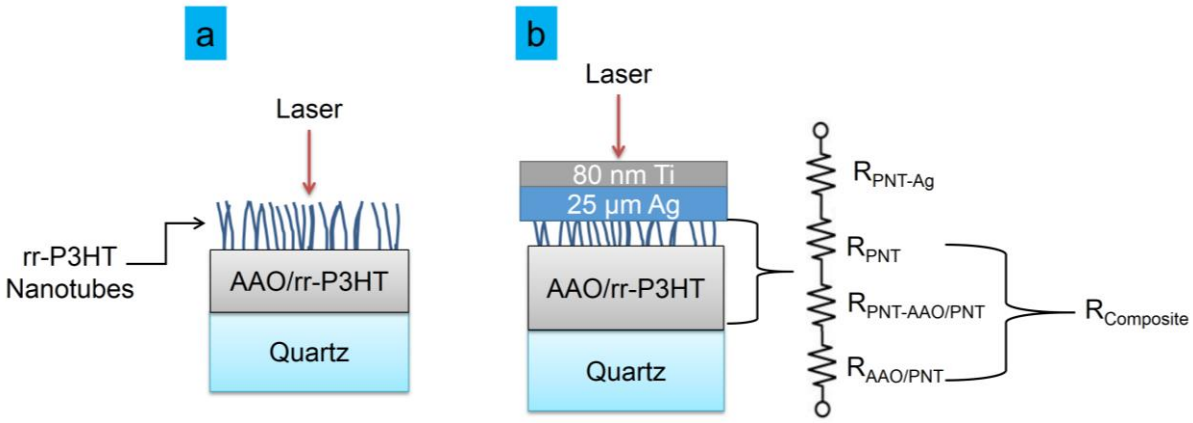

Figure 16. Sample configuration used to measure array thermal conductivity (a) and the total thermal resistance (b). The total thermal resistance measure in b is comprised of the contact resistance between the nanotube array and the contacting Ag foil ($R_{PNT\text{-}Ag}$) and the resistance of the composite layer, $R_{Composite}$. The composite layer consists of the array resistance (R_{PNT}), the contact resistance between the array and AAO/rr-P3HT composite layer ($R_{PNT\text{-}AAO/PNT}$), and the resistance of AAO/rr-P3HT composite layer ($R_{AAO/PNT}$).

Figure 17 illustrates the sensitivity of the thermal conductivity measurement for the bare rr-P3HT layer with and without the top metal foil. The sensitivity (S_i) is calculated by perturbing a property (P) of value i by ±1% and then determining the corresponding phase shift (Equation 4).

$$S_i = p_i \frac{\partial \phi}{\partial p_i} \tag{4}$$

In Figure 17, it is clear that the system is at least three times more sensitive to the nanotube thermal conductivity measurements when the measurements are made without the top foil.

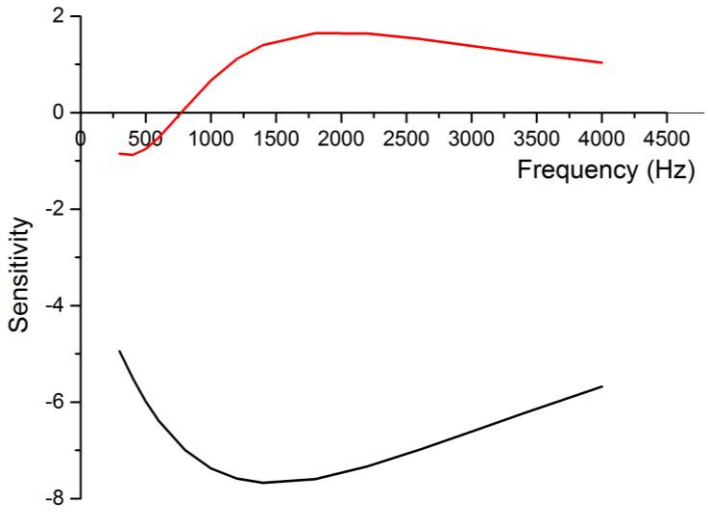

Figure 17. Sensitivity of the PA thermal conductivity measurement with (red line) and without (black line) the top foil.

The model fitting parameters used to determine the thermal conductivity of the 12 minute etched array are outlined in Table 3. For the thermal conductivity measurement, the unknown fitting parameters are the nanotube array (rr-P3HT 200 nm) thermal conductivity, the nanotube array density, the contact resistance between the quartz and AAO/rr-P3HT layer and the contact resistance between the nanotube array and AAO/rr-P3HT layer.

Table 3. Photoacoustic fitting parameters to determine the thermal conductivity of the 12 minute etched array. The fitted unknown values are in bold.

	Density	Thermal Conductivity	Specific Heat	Thickness	Optical Absorption Length	Contact Resistance	Layer Resistance
	kg/m³	W/m-K	J/kg-K	µm	µm	mm²-K/W	mm²-K/W
Quartz	2200	1.38	753	5000	0.001	**4.30 ± 0.8**	3623
AAO/rr-P3HT	800	1.30	900	25	0.001	**0.10 ± 1.1**	19.23
rr-P3HT 200 nm	**405 ± 23**	**0.91 ± 0.2**	1100	8	1.6	0.01	8.84

He	0.273	0.152	5190	0.00	0.001	0	0

The calculated uncertainty of the thermal conductivity measurements considers both the measurement and data fitting uncertainties. The measurement uncertainty for the unknown parameters was found by altering their properties by 5, 20, 1/5, and 1/20 the estimated values and the thermal conductivity uncertainty was found by calculating the standard deviation of data fits with similarly low residuals. The fitting uncertainty was found by shifting the phase data ±1° and the resulting bounding uncertainties and data fits are illustrated below in Figure 18.

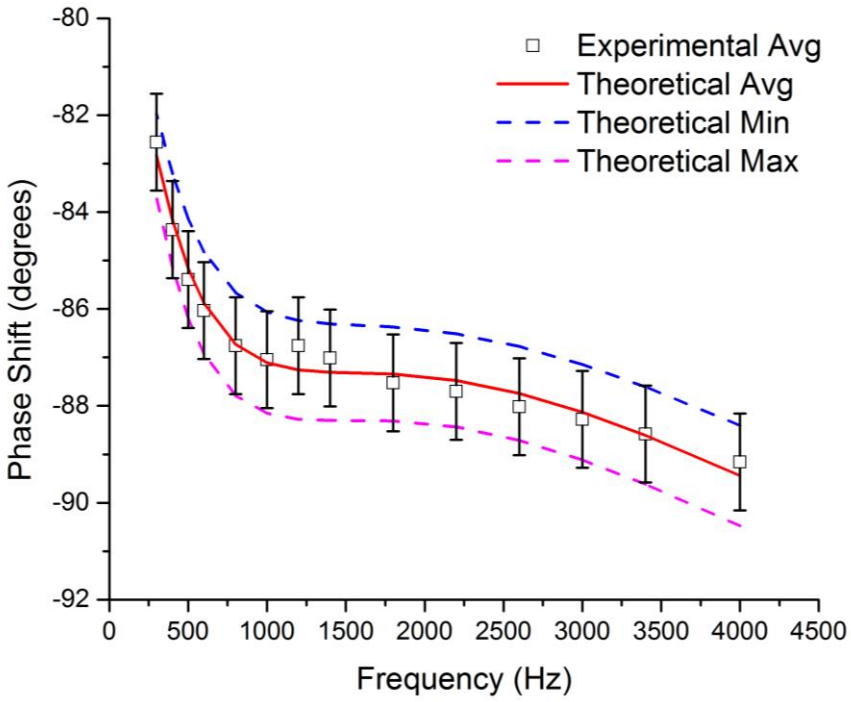

Figure 18. Representative PA data for thermal conductivity measurement on samples etched for 12 minutes, fitting data is included in Table 3. The plot shows the bounding uncertainty associated with a phase shift of plus or minus one degree.

The total uncertainty was then calculated using Equation 5 where Δ_{meas} is the measurement uncertainty and Δ_{fit} is the data fitting uncertainty.

$$D_{total} = \sqrt{D_{meas}^2 + D_{fit}^2} \tag{5}$$

The uncertainty analysis indicates that the confidence intervals for the contact resistance values are too large to accurately resolve these properties individually. This result motivated the sample configuration used to measure the total thermal resistance where the total layer resistance was measured and then we took the difference in these measurements to measure the impact of nanotube array morphology. Figure 19 below illustrates the model sensitivity to the unknown fitting parameters from **Table 3**.

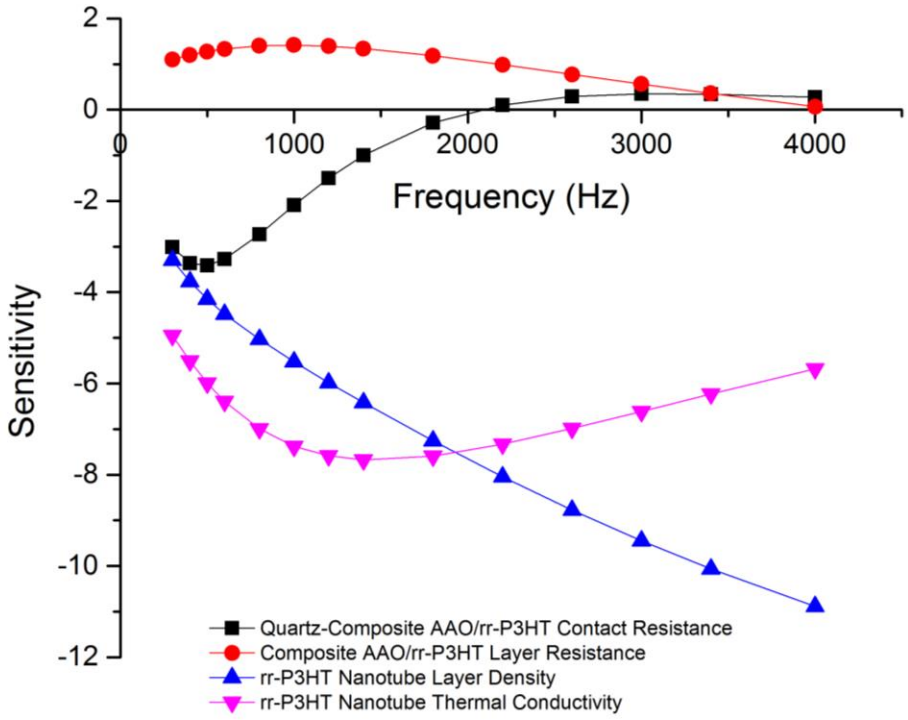

Figure 19. Representative sensitivity plot of unknown fit parameters when measuring array thermal conductivity. The measurement is most sensitive to the rr-P3HT density, quartz composite contact resistance, and thermal conductivity.

2.4.2 Nanotube Thermal Conductivity

Our recent modification to the PA method[71] and the methods described above were used to measure the rr-P3HT array thermal conductivities as a function of etch time (Figure 20). The sample configuration for measuring the array thermal conductivity is shown in Figure 20b, where the nanotube array is exposed directly to the PA laser to increase the sensitivity of the measurement to array thermal conductivity.[71]

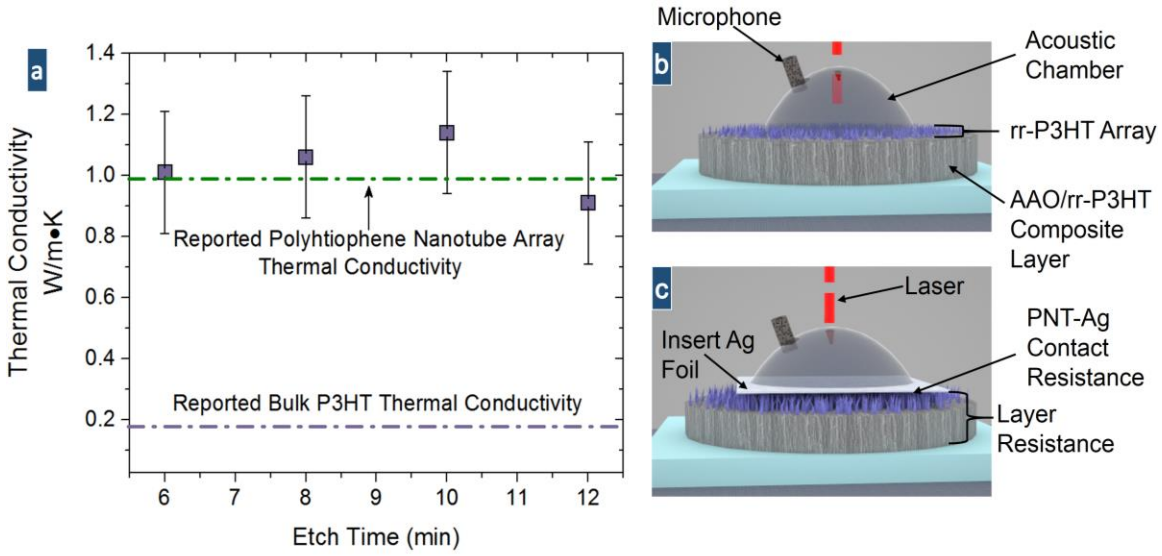

Figure 20. Graph a shows that as the etch time increases from 6 to 12 min the array thermal conductivity (indicated by the purple square markers) remains nearly constant within the range of uncertainty and is similar to values reported previously by Singh et al.[56] Illustrations b and c show the photoacoustic array thermal conductivity and interface resistance measurement assemblies, respectively.

The measured thermal conductivity of the rr-P3HT nanotube arrays is approximately 1 W/m·K, independent of etch time. These results are similar to the thermal conductivities reported for polythiophene nanotube arrays made through electropolymerization using the same nanoporous alumina templates.[71] Using the template porosity of ~50% reported by the manufacturer (and confirmed through SEM imaging), we estimate the thermal conductivity of individual rr-P3HT nanotubes to be ~2 W/m·K, which is about an order of magnitude higher than the reported bulk film value[109] and agrees well with the reported thermal conductivity of melt processed semi-crystalline P3HT nanowires with similar diameters.[110] Directional chain alignment has been shown to enhance thermal conductivity in amorphous polymer nanostructures[71] and crystallinity may also improve thermal transport.[110] Therefore, the results of the present work suggest that anisotropic

chain alignment (confirmed through Polarized Raman Spectroscopy in Chapter 3) is promoted in this system as well, because the rr-P3HT nanotubes appear to be amorphous from electron diffraction analysis on several samples (Figure 5).

To isolate the impact of the surface fraction on thermal transport, the total thermal resistance of the rr-P3HT nanotube array-AAO template composites in contact with silver foil was measured as a function of etch time. Since the array thermal conductivity does not change with etch time, and thermal transport through the composite AAO/rr-P3HT layer is limited by contact resistance between the template walls and the part of the nanotubes that is still in the template (i.e., the path of lest thermal resistances is from the tip to the base of the PNTs), the change in total thermal resistance is likely dominated by the change in the PNT-Ag contact resistance. The reported total resistance value corresponds to the sum of the resistance between the PNT tips and the silver foil (R_{PNT-AG}), the layer resistance of the nanotube array, the PNT-AAO composite layer resistance, and the interface resistance between the nanotubes and the composite structure.

2.4.3 Nanotube Array Thermal Contact Resistance

The total thermal resistance was measured after 6 minutes of etching and Figure 21 shows the relationship between etch time and the change in R_{PNT-Ag}, determined by subtracting the total resistance for the surfaces with 8, 10, and 12 minute etch times from the total resistance of the surface after 6 minutes of etching. One potential artifact of this type of measurement is that the surface fraction may be changing during photoacoustic testing due to compression forces (the silver foil placed onto the PNT surfaces is under 138 kPa). However, the sample surface undergoes no noticeable change in morphology when

imaged after testing, and any surface fraction change due to normal compression is expected to be similar for all samples. If bending of the ridges occurs, we do not expect the degree of bending to be significant because the ridge formation distributes the load over the entire array resulting in a high effective resistance to bending, and any increase in surface fraction is expected to scale based on the initial fraction, similar to the scaling expected for normal compression.

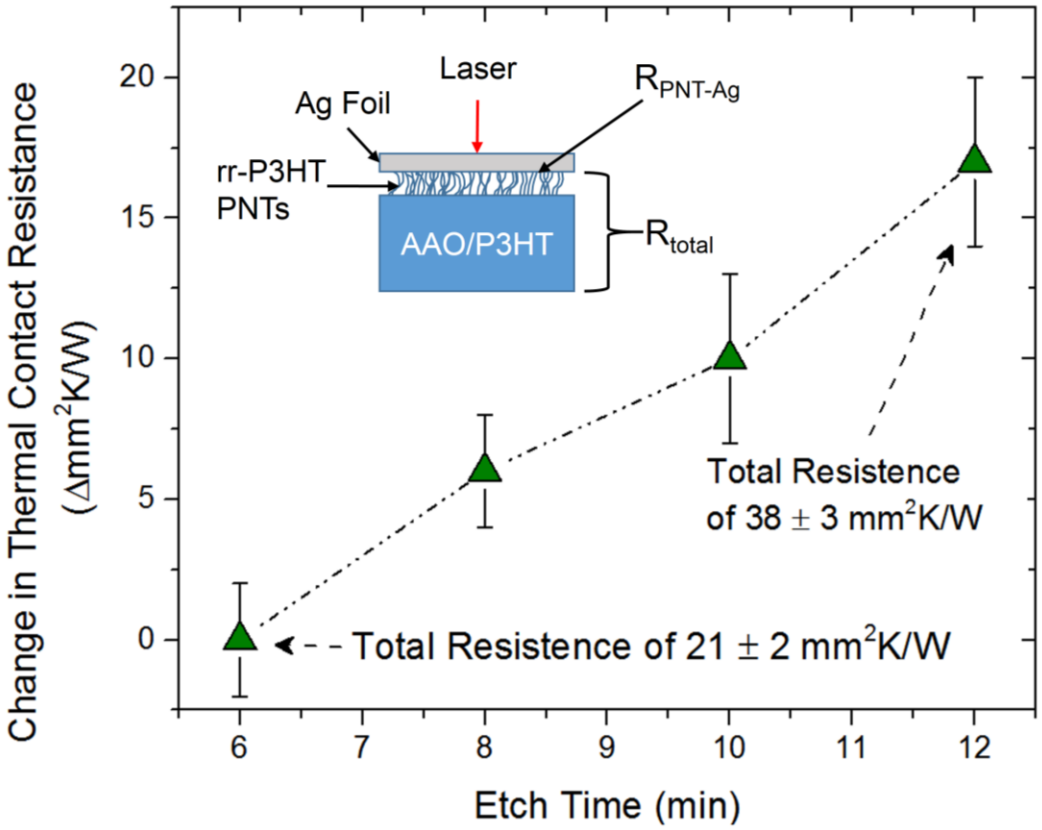

Figure 21. The total thermal interface resistance, which is the measured sum of the resistance between the PNT tips and the silver foil (R_{PNT-AG}), the layer resistance of the nanotube array, the PNT-AAO composite layer resistance, and the interface resistance between the nanotubes and the composite structure, for the surfaces with 6, 8, 10, and 12 minute etch times is indicated by the green line with triangular markers. Each data point represents the average of three measurements taken at different spots on the surface.

As the etch time increases the total thermal resistance increases from the initial minimum of 21 ± 2 mm^2K/W measured after an etch time of 6 minutes to a final value of 38 ± 3 mm^2K/W measured for the 12 minute etch time at a rate of approximately 6 mm^2K/W per 2 minute interval. The increase in thermal resistance is due to a decrease in the number of nanotube tips in contact with the surface and possibly due to a slight decrease in the array thermal conductivity as nanotubes collapse and lose their vertical alignment. We note that the collapse of nanotubes decreases the thickness of the sample (i.e., the exposed array plus the remaining template), which likely reduces the combined layer resistances with increased etch times. Thus, the increase in contact resistance with etch time is likely even larger than what can be concluded directly from the measurements of total thermal resistance. The resistance values for the 2 and 4 minute etched samples were not measured due to template and etching inconsistencies including height variations that could lead to artificially high contact resistance values.

2.5 Conclusions

We developed a two-step solution processing technique to fabricate vertically aligned arrays of regioregular poly(3-hexylthiophene) nanotubes with tunable surface morphologies and thus tunable properties, including wetting (contact angle and contact angle hysteresis) and thermal contact resistance as two important candidate applications. The surface morphologies are dictated by the length of nanotubes freed in a template etching process, with longer etch times resulting in larger exposed lengths, larger spacing between the nanotube surface ridges, and smaller surface fractions, in contrast to prior

reports of increased surface fractions with capillary bundling of vertical nanowires.[78, 87, 88] The self-assembled poly(3-hexylthiophene) nanotube array surfaces roughly follow Cassie-Baxter wetting trends and are superhydrophobic with static contact angles greater than 150° and contact angle hysteresis less than or equal to 10° when the surface fraction is below 0.15. The total thermal resistance of an interface assembled with the poly(3-hexylthiophene) nanotube arrays increases from a minimum of 21 ± 2 mm^2K/W to a maximum of 38 ± 3 mm^2K/W as the etch time increased from 6 to 12 minutes, which is likely caused by the reduction in surface fraction and contact area at the interface. The thermal conductivity of the poly(3-hexylthiophene) nanotube arrays is 5-fold larger than the bulk film value because of molecular chain alignment in the direction of heat transfer, which enables the material to produce very low thermal transport resistances for a pure polymer. Our results demonstrate the achievement of tunable superhydrophobic surfaces through a novel solution processing method and illustrate the impact of array morphology on the thermal contact resistance of vertically aligned, high aspect ratio polymer nanostructures, which could emerge as tunable materials to meet the needs of a variety of important applications.

CHAPTER 3. DIAMETER AND MOLECULAR WEIGHT DEPENDANCE OF MELT-PROCESSED POLYMER NANOFIBER THERMAL CONDUCTIVITY

.

3.1 Introduction

Nearly all commercially available polymer based thermal interface materials (TIMs) rely on the use of conductive fillers including nitride, oxide, carbon and metal particles. Polymer composite materials can achieve high thermal conductivity, but filler particles tend to be expensive and result in large processing and material costs. Improved chain alignment through mechanical drawing of polyethylene (PE) has been established as a method to enhance polymer thermal conductivity since the late 1970's.[42, 111, 112] More recent efforts have achieved thermal conductivity values as high as ~40 W/m-K in a drawn film,[113] and ~100 W/m-K in a drawn nanofiber.[114] Simulations have shown that while the highest thermal conductivity is realized in a 1D polymer chain, even bulk 3D crystals of PE will have thermal conductivity of ~50 W/m-K in the direction of the polymer backbone (c crystal direction).[115] In contrast, Choy et al. demonstrated experimentally that the thermal conductivity perpendicular to the polymer chain in a PE crystal is even lower than bulk semi-crystalline PE.[113] Nanoconfinement within nanoporous templates is known to promote polymer chain elongation and alignment in polymer nanofibers, passively enhancing thermal transport anisotropically without the need for mechanical drawing. We find only one nanoporous template based effort to create high thermal conductivity PE

where Cao et al. infiltrated 100 nm and 200 nm AAO templates with high-density polyethylene (HDPE) using a vibration assisted nanoporous template melt technique and estimated the resulting single fiber thermal conductivity to be a remarkable 26.5 W/m-K and 20.5 W/m-K, respectively.[57] Cao et al. extended their work by measuring low-density polyethylene (LDPE) nanofibers and found the thermal conductivity to be ~5 W/m-K at 200 nm diameter.[75] Polyethylene is interesting from a commercial perspective due to low cost and ease of processing, however, it's low temperature stability (relatively low melt temperature) may limit the use of PE in high temperature applications.

Polythiophene derivative poly(3-hexylthiophene-2,5-diyl) (P3HT) is one of the most thoroughly investigated conjugated polymers due to ease of processing and favorable properties for organic electronics (and it was relatively cheap to synthesize). Moreover, P3HT is also promising for thermal management applications because of its relatively high temperature stability and predicted high thermal energy transport in the direction of polymer chain backbone.[39] In bulk form, P3HT exhibits isotropic thermal conductivity of 0.19 W/m-K, but electrochemically processed polythiophene nanotubes and nanofibers,[116] solution processed P3HT nanotubes,[117] and melt processed then annealed P3HT nanofibers[110] have all demonstrated at least an order of magnitude improvement in thermal conductivity. Specifically, the electrochemically processed nanofibers exhibited increased thermal conductivity with decreasing diameter, with values peaking at 4.4 W/m-K for the 70 nm diameter fibers. In contrast, Rojo et al. found that melt processed (and annealed) P3HT nanofiber's thermal conductivity increased with fiber diameter with a maximum value of 2.3 W/m-K for the 350 nm fibers and a relatively low value of 0.5 W/m-K for the 120 nm fibers. In addition, they suggested that the enhanced thermal conductivity was a

result of pi-pi stacking perpendicular to the long axis of the fiber (heat transport direction). Whereas a more recent report of thermal transport in spontaneously formed P3HT nanofibers with similar chain orientation (P3HT chain backbone is normal to the fibers long axis and fiber is formed through π-π stacking between chains) show exceptionally low thermal conductivity of 0.055 W/m-K.[118] These contradictory results demonstrate the need for further investigation into P3HT nanofiber thermal transport and processing trends.

Here we demonstrate a simple AAO template melt infiltration process to produce high density P3HT and PE nanofiber arrays. The photoacoustic method is used to measure their thermal conductivity as a function of both polymer molecular weight and nanofiber fiber. Polarized Raman Spectroscopy is employed to demonstrate preferential chain alignment in the direction of the long-axis of the fiber as a result of the template filing procedure. These nanofiber arrays exhibit high thermal conductivity and may be useful for thermal management applications including us as thermal interface materials in a broad range of technical applications.

3.2 Nanofiber Melt Fabrication

Nanoporous anodic aluminum oxide (AAO) templates with ~200 nm nominal pore diameter were purchased from SigmaAldrich (Whatman Anodisc) and templates with 100 nm and 55 nm were purchased from Synkera. The templates were infiltrated with PE and P3HT of various molecular weights and properties as outlined in **Table 4**. The high and low density polyethylene (HDPE and LDPE, respectively) and high and low molecular weight P3HT (H-P3HT and L-P3HT, respectively) samples were purchased from SigmaAldrich and used as received.

Table 4. List of polymers tested for melt infiltration and their properties in bulk form. Density, molecular weight, and melting point values were provided from manufacture (Sigma).

Polymer	Molecular Weight (Mw)	Melting Point (°C)	Density (kg/m^3)	Thermal Conductivity (W/m-K)
High Density Polyethylene (HDPE)	~120,000	125	950	0.44
High Mw P3HT (H-P3HT)	~65,000	~260	1060	0.19
Low Density Polyethylene (LDPE)	~30,000	110	920	0.30
Low Mw P3HT (L-P3HT)	~25,000	~230	920	0.19

The viscosity of the polymers at some elevated temperature is important to understanding the ability of a polymer to infiltrate the template pores at a given temperature, pressure (applied pressure between infiltrating polymer film and template), and pore diameter, but these data were not readily available. For the PE and L-P3HT samples we use only the 200 nm nominal pore diameter templates and for the H-P3HT sample we used the 55 nm, 100 nm, and 200 nm diameter templates. The fabrication process for a melt-processed NF array is shown Figure 22. The PE polymer film (made by melting down PE pellets from Sigma between two glass slides, typical film thickness was at least double the template thickness of 60 μm) is placed on the AAO template and then sandwiched between two glass slides. 25 kPa of pressure is applied and the stack is heated

for 4 h to 150 °C in a vacuum oven before cooling back down to room temperature passively for ~1 h. The template area is approximately 4.3 cm^2 with a porosity of ~50%.

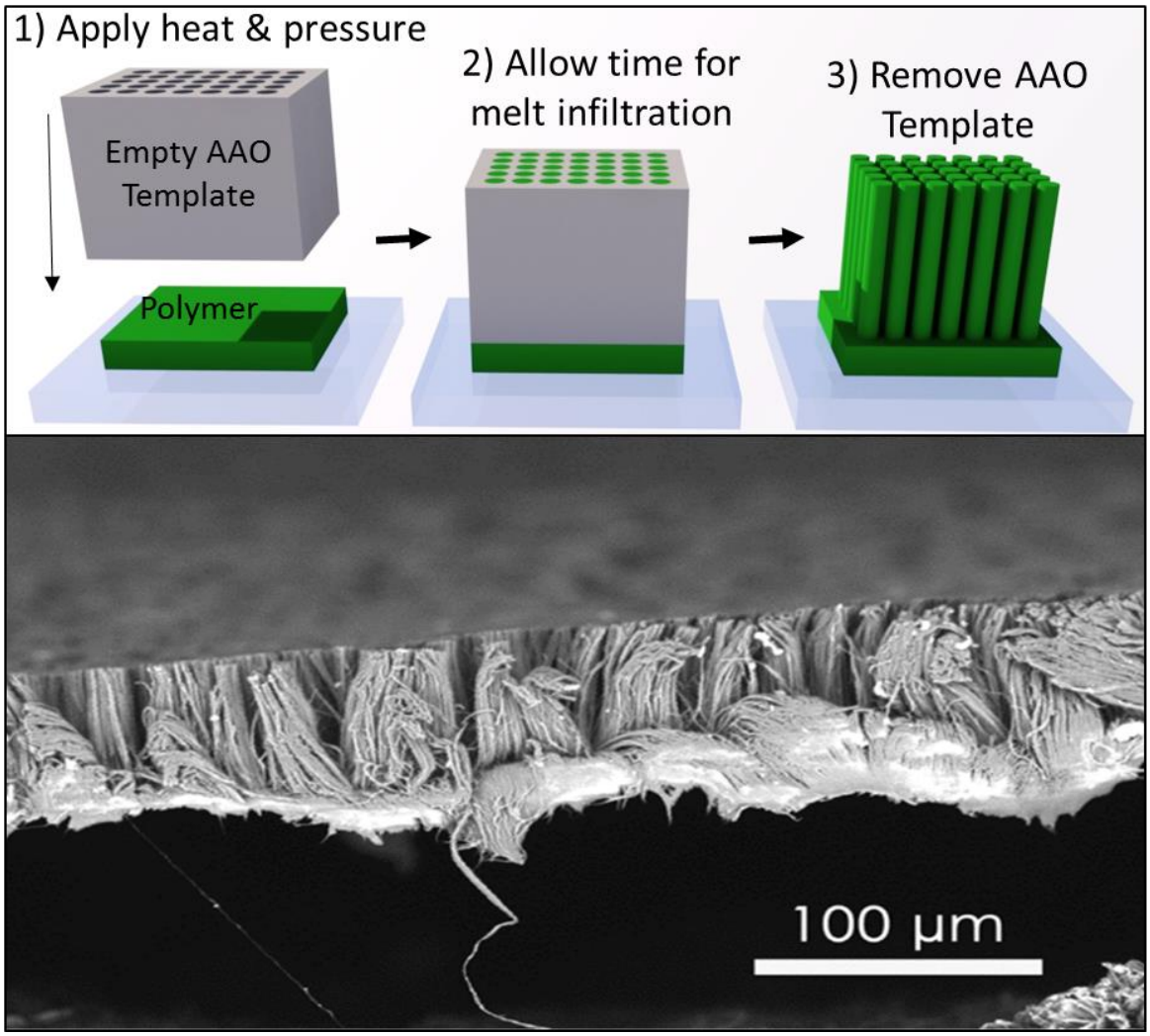

Figure 22. Steps to fabricate polymer nanofibers within the pores of nanoporous alumina templates. In step 1, empty AAO templates are placed on top of polymer film under 25 kPa of pressure and in step 2 the stack is placed in a vacuum oven for melt infiltration. Step 3 illustrates the free-standing nanofiber array after template removal in 1M KOH. A Cross-sectional SEM image of a free-standing PE nanofiber array is included at the end of the sequence.

The LDPE and HDPE samples were placed in vacuum oven at ~155°C, which is sufficient to melt the LDPE and HDPE. The P3HT samples need higher temperature to flow well and are prone to oxidation, thus were heated in a Heraeus vacuum oven with Nitrogen atmosphere set to 270°C. The P3HT samples were only placed in the oven for ~1.5 hours where the first hour the oven heats to 270°C at a rate of approximately 5°C/min and for the remaining 30 minutes, the polymer fully infiltrates the AAO template at 270°C. The samples were then removed from the oven and quenched in water to prevent oxidation and degradation of the nanofibers, as well as to preserve chain alignment. Once the sample is cooled back to room temperature it is immersed in a bath of KOH (1M) for a full template etch. After soaking in KOH for at least 3 h, the template is placed in DI water to wash away the residual KOH and AAO. For some applications, it may be desirable to fabricate nanofiber arrays with increased thickness and with nanofibers exposed on both sides of the polymer support film. Thickness is especially important to TIM applications because bond line tolerances in electronic packages are often at least 50 μm in thickness. Figure 23 illustrates a process that was developed to create two-sided nanofiber array with middle support film. We hypothesize that that the ridge formation observed in Chapter 2 was suppressed due to increased nanofiber stiffness as compared to less stiff nanotubes.

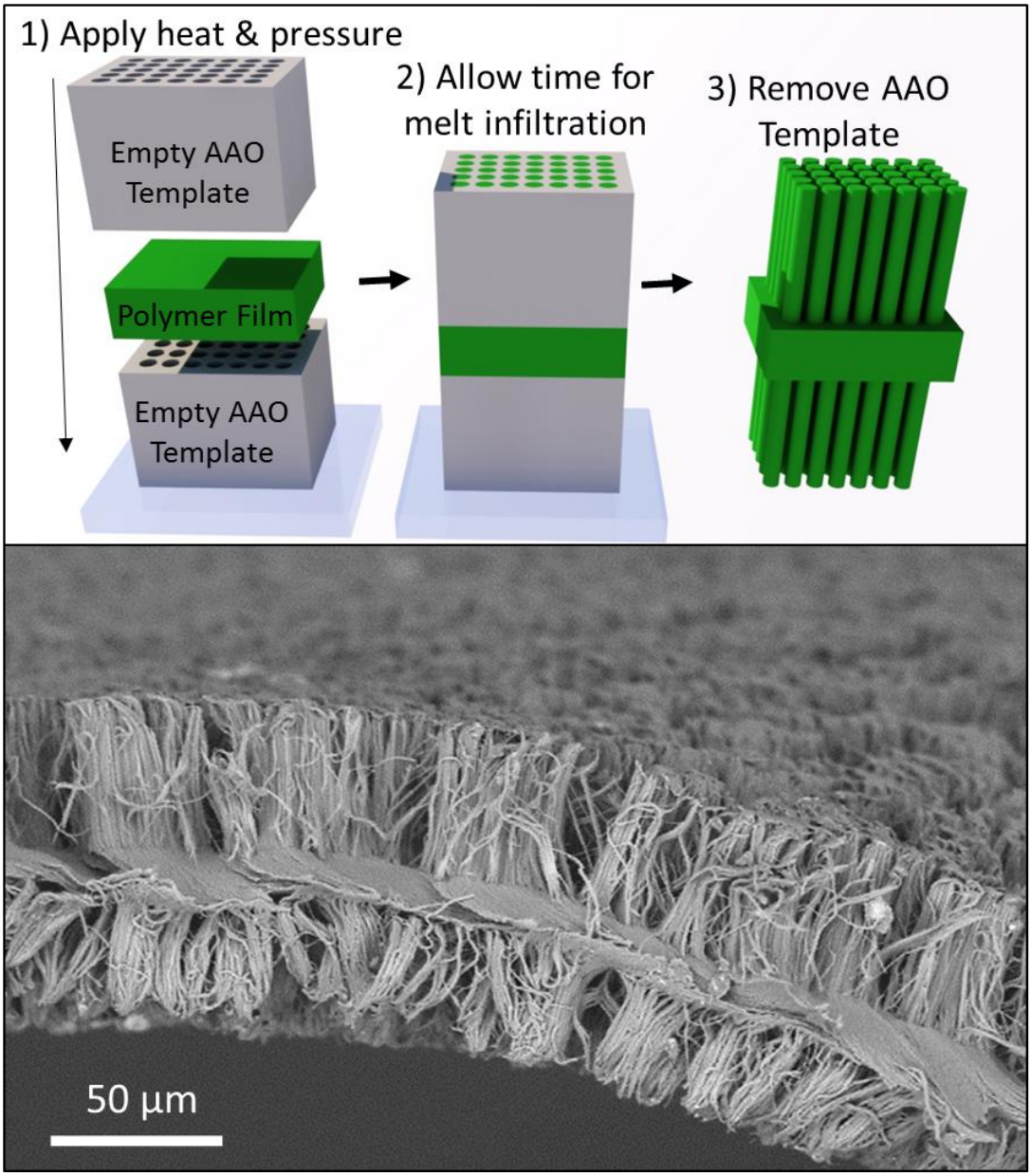

Figure 23. Steps to fabricate two-sided polymer nanofiber arrays using nanoporous alumina templates. In step 1, empty AAO templates are used to "sandwich" a polymer film under 25 kPa of pressure and in step 2 the stack is placed in a vacuum oven for melt infiltration. Step 3 illustrates the free-standing, two-sided nanofiber array after template removal in 1M KOH. A Cross-sectional SEM image of a P3HT two-sided nanofiber array is included at the end of the sequence. The middle film in the illustration is not draw to scale and should have reduced thickness after infiltration.

3.3 Nanofiber Photoacoustic Thermal Characterization

The photoacoustic method is a photo-thermal technique to measure the thermal conductivity of thin films and nanostructures and has been explained in detail elsewhere.[119] In short, a sample is placed in a sealed chamber of helium atmosphere and a modulated laser of chosen modulation frequency strikes the sample surface. As the sample temperature rises heat is conducted into the helium gas near the sample surface and the gas expands sending acoustic pressure waves through the chamber. The acoustic signal's phase shift as a function of laser modulation frequency is compared to a reference sample of known properties through a one dimensional heat transfer model to determine the unknown thermal conductivity and interface resistences in a multi-layer material.[120] and a theoretically generated non-linear fitting algorithm is used to fit for multiple unknown material properties. Here we measure the thermal conductivity of polymer and template together with a top Ti layer and extract the polymer thermal conductivity based upon a separate measurement of the AAO thermal conductivity. Because PE does not absorb strongly at 1100 nm, it was not possible to make bare array measurements as has been done in previous studies [116] and metallizing the tips of the etched NF arrays caused them to soften and deform somewhat due to the high temperature during metal evaporation. Instead the top of the AAO template is coated with 150 nm Ti, which formed a continuous layer and absorbed the laser energy.

Because the template is thick (60 μm) and the effective conductivity is relatively low (~1-5 W/m-K), we employ extremely low modulation frequencies to fully penetrate

the AAO-polymer composite. Measurements are performed over a range of 5-300 Hz, which is much lower than typically used. To verify the operation over this low range, we measure a 25-μm thick LDPE film to be 0.3 W/m-K over the same frequency range, in good agreement with the expected value. In addition, we calibrate the testing configuration by measuring the thermal conductivity of metal films with known conductivity. The sensitivity of the model to each fitting parameter is determined by perturbing the property value by ± 1% and then recalculating the phase. The thermal conductivity of the PE-AAO and P3HT-AAO composites is the most sensitive parameter in the PA thermal model over the 5-300 Hz frequency range (Figure 24a), and the only other highly sensitive parameter is the density of the composite. We fit for these two parameters along with the contact resistance on either side of the AAO. The density is not set as a fixed parameter because the AAO templates can have closed pores filled with air, and other areas could have incomplete polymer infiltration, so we allow this to be an unknown and monitor the result to make sure it falls between the value for just AAO and air and AAO and polymer. Local template filling variability is accounted for by measuring multiple spots across a sample for each reported value. The phase shift of the PA measurement for the PE samples clearly shows the difference in thermal conductivity between the AAO-LDPE and AAO-HDPE (Figure 24b). For the 200 nm diameter PE nanofibers, a total of 12 samples are measured, six of each type of polymer. Four measurements are recorded for each of the P3HT samples with 200 nm diameter fibers and then four each for the H-P3HT samples with both 100 nm and 55 nm diameters.

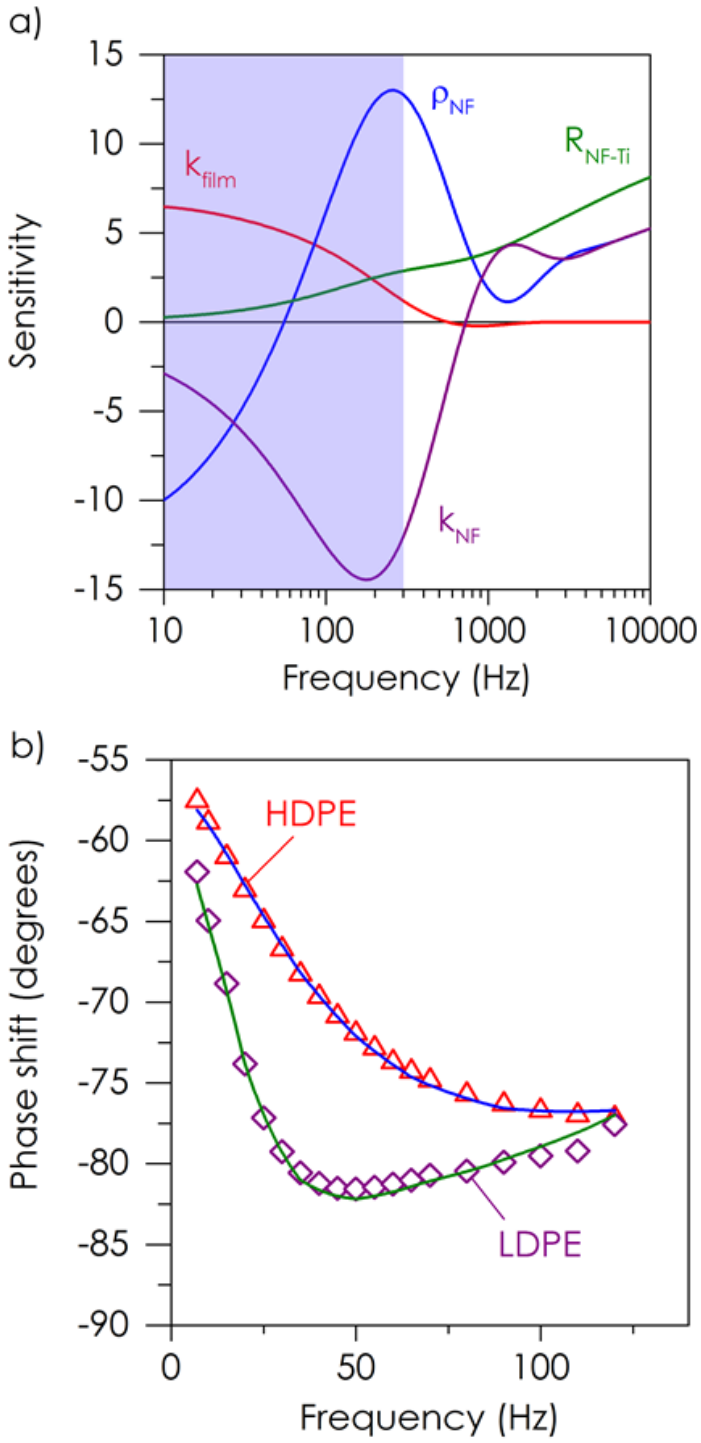

Figure 24. Photoacoustic measurements of PE in AAO. a) Sensitivity to sample properties (shaded area was test frequency range) where K_{NF} is nanofiber thermal conductivity, K_{film} is PE film thermal conductivity, ρ_{NF} is nanofiber density, and R_{NF-Ti} is the contact resistance between the Ti film and NF tips. b) Phase shift for LDPE and HDPE in AAO data (markers) fitted to thermal model (lines).

3.4 Nanofiber Polarized Raman Spectroscopy

Polarized Raman has been used extensively to characterize orientation of PE chains,[121-124] usually in drawn films, but also in microfibers.[124] More recently, polarized Raman has also been used to characterize polymer chain alignment in thin P3HT films.[125] We find no previous reports of polarized Raman or polarized IR used to determine chain orientation in PE or P3HT nanofibers. In general, the ratio of the scattering intensity of light polarized parallel and perpendicular to the fiber's long axis can serve as an indication of relative orientation of chemical bonds. Moreover, scattering intensity is greater in symmetrically vibrating bonds when the excitation light is polarized parallel to the bond direction. Hence, in an aligned polymer fiber, the scattering intensities for the symmetric vibrational modes along the chain backbone are larger when the excitation light is polarized parallel to the fibers long axis. In contrast, when chain orientation is isotropic, the scattering intensity of symmetric backbone bonds should not be significantly different for horizontally and vertically polarized excitations. A Renishaw inVia confocal Raman microscope featuring a 1200 or 3000 gr/mm grating selection with a linearly polarized 532 nm laser line was used in backscattering mode with a 20x objective. The laser was focused on the cross section of a template filled with polymer fibers in a position with the fiber's long axis either parallel or perpendicular to the polarization of the incoming laser beam (Figure 25A) (this was achieved by rotating the sample 90°). The intensity of the parallel scattering after parallel excitation I_{zz} and orthogonal scattering after orthogonal excitation I_{xx} were recorded to demonstrate polymer chain orientation, where parallel and orthogonal are directions relative to the fiber's long axis.

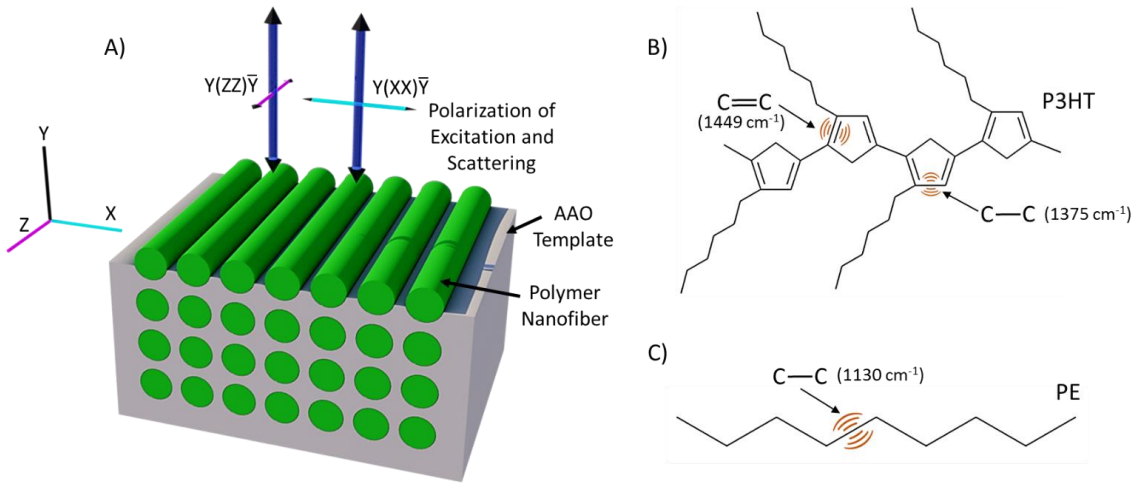

Figure 25. A) Experimental sample configuration for Polarized Raman measurements of exposed polymer nanofibers. Porto's notation is used to illustrated the excitation and scattering beam propagation directions as well as the excitation and scattering polarization directions for the I_{zz} (parallel to fiber's long axis) and I_{xx} (perpendicular to fiber's long axis). B) Vibration band assignments for the P3HT C=C symmetric stretch vibration of the thiophene ring at 1449 cm^{-1} and the backbone C-C intra-ring stretch at 1375 cm^{-1}. C) Vibrational band assignment for the C-C symmetric stretch vibration along the PE chain backbone at 1130 cm^{-1}.

The investigated vibrational band assignments are illustrated for P3HT in Figure 25B. Numerous studies have demonstrated the use of polarized Raman spectroscopy to investigate anisotropic P3HT chain alignment.[126-128] The primary bands of interest are the thiophene ring's C=C symmetric stretch vibration at 1449 cm^{-1} and the backbone C-C intra-ring stretch at 1375 cm^{-1}, both of which produce increased Raman intensity when the polarization of the excitation laser is parallel to the stretching direction. Likewise, the C-C symmetric stretch vibration at 1130 cm^{-1} can be used to determine chain orientation in aligned PE and are illustrated in Figure 25C.[121, 123]

3.5 Results and Discussion

3.5.1 Nanofiber Thermal Conductivity and Molecular Weight

The values of NF thermal conductivity measured for LDPE peaked at 3.8 W/m-K with an average uncertainty of 33%. The HDPE NF thermal conductivity varied from 2.9 W/m-K to 9.1 W/m-K with an average uncertainty of 27%. It should be noted that besides a single sample with a value of 2.9 W/m-K all of the other HDPE samples had a thermal conductivity of above 4 W/m-K. The range of thermal conductivity values observed here are plotted along with the P3HT results for solid 200 nm fibers in Figure 26. The mean thermal conductivity for the 200 nm P3HT nanofibers was approximately 2.5 W/m-K for the L-P3HT samples and 2.3 W/m-K for the H-P3HT samples with no significant statistical difference between the two considering measurement uncertainties. The high variability in the thermal conductivity of HDPE NF compared to other polymers was not clear, although it could be due to small differences in thermal treatment or difficulties in achieving uniform template infiltration. Because the HDPE molecular weight (and chain length) is significantly larger than the other polymers (higher viscosity) this makes melt infiltration in the nanopores more difficult. It is expected that locally there may be more voids in the pores with HDPE although this was difficult to assess.

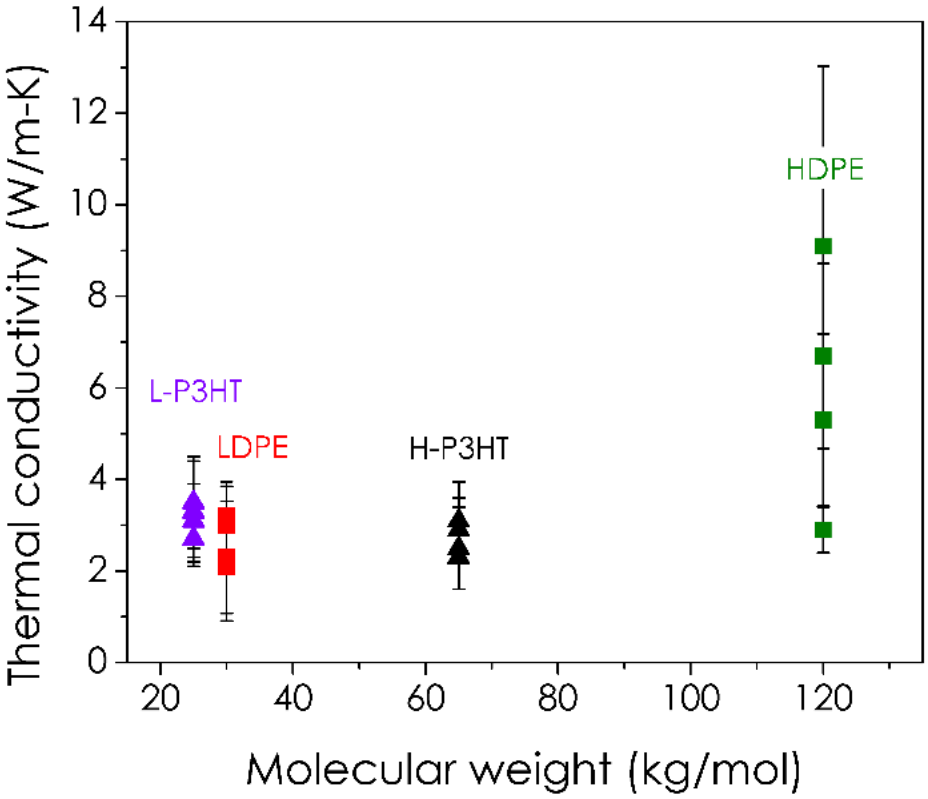

Figure 26. Thermal conductivity as a function of polymer molecular weight for the 200 nm PE and P3HT nanofibers with high and low molecular weight samples for each.

The average HDPE NF thermal conductivity is approximately 6.0 W/m-K in comparison to the report of Cao et al. of 20.5 W/m-K [57]. Both nanofibers are created using melt infiltration of an AAO template of 200 nm in diameter, although the molecular weight of the polymers used by Cao is not known which could have a dramatic effect on the thermal conductivity. However, the major difference in the previous work is they used kHz oscillations while infiltrating the template to create shear within the melt. It is possible that this process could lead to additional chain alignment along the pore axis, although no structural characterization of the fibers was reported. Lastly, there may be issues with the measurement since the sample includes a polymer film that is more than twice the thickness of the NF array being tested. The high single nanofiber thermal conductivity was estimated

from a measured total thermal conductivity on the order of 0.7 W/m-K assuming series resistance of the two segments of the sample. Here, our back film is on the order of 3-5 μm meaning most the thermal resistance in the sample is due to the NF array composite, although the backside film does contribute to the relatively high uncertainty (~30%) of our measurements. Ma et al. used electrospinning to create HDPE nanofibers ranging in thermal conductivity from 0.5 to 9.3 W/m-K with diameters between 150 and 50 nm [54], although it is difficult to directly compare the chain orientation resulting from the two different fabrication methods without further structural characterization.

The thermal conductivity of HDPE is significantly higher than P3HT and LDPE for the same dimensions (i.e. 200 nm solid fiber). The explanation for the higher thermal conductivity in HDPE compared with LDPE and P3HT could be the improved alignment due to strong confinement effects. However, a previous study reported that for 200 nm pores the crystallites tended to orient with the high conductivity perpendicular to the pore axis [129]. DSC measurements show that for both LDPE and HDPE fibers the crystallinity is low (i.e. 50% or less) and the intercrystalline amorphous regions will play an important role in heat transfer. Recent simulations have also shown that the thermal conductivity of polymer chains can increase with length[130] implying that HDPE could benefit not only from reduced van der Waals contacts (high M_w results in longer heat conduction pathways along the chain backbone and less interchain conduction), but from high conductivity chains as well (reduced intrachain scattering). The insignificant difference between thermal conductivity of the P3HT samples is difficult to explain and further structural analysis is being pursued. However, the higher H-P3HT molecular weight only equates to a transition from a contour chain length of ~60 nm for L-P3HT to ~140 nm for H-P3HT

(and their length in the fiber will always be closer to Rg even if partially aligned). Because the 140 nm chain length is still significantly less than the 200 nm nominal pore diameter, confinement effects may not be significant enough to alter thermal transport between these diameters. It should be noted that the different melt infiltration temperature and time for P3HT compared with PE may be playing a role in differences in conductivity observed here, although this was not quantified.

3.5.2 Nanofiber Thermal Conductivity and Diameter

H-P3HT nanofibers with diameters of 100 nm and 55 nm were fabricated to determine the impact of confinement on thermal conductivity. Figure 27 illustrates H-P3HT thermal conductivity as a function of nanofiber diameter with the 200 nm diameter L-P3HT, HDPE, and LDPE included for reference. In addition, a previous study measuring the thermal conductivity of electropolymerized polythiophene fibers is included.[116]

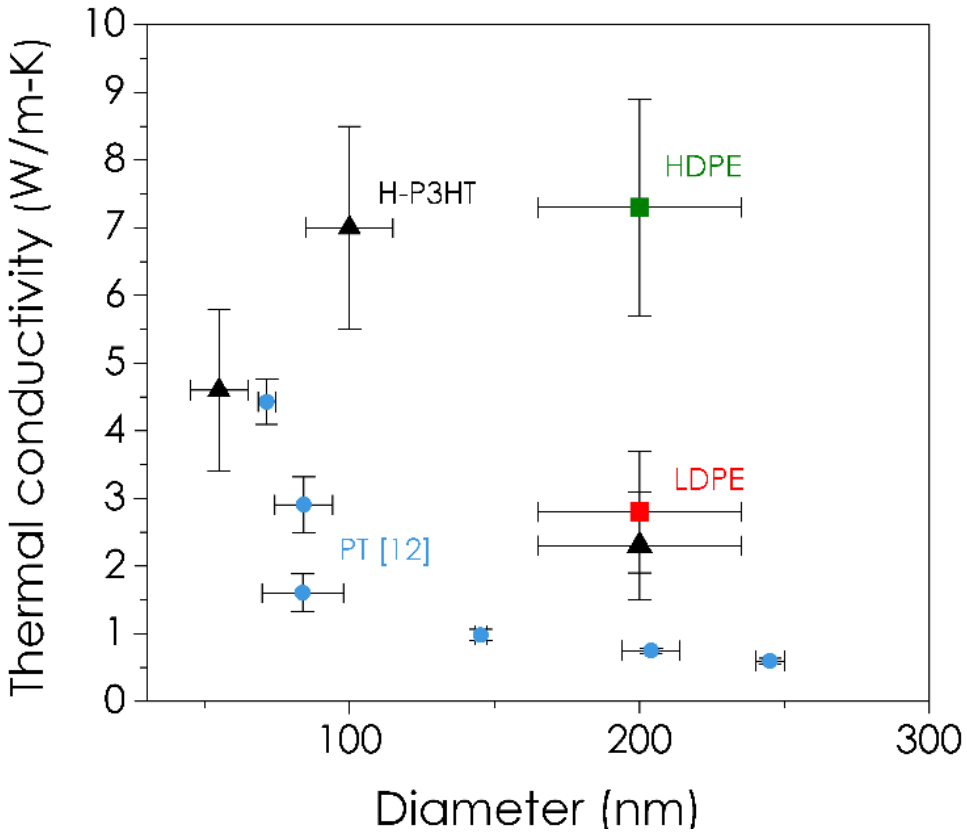

Figure 27. Thermal conductivity as a function of polymer nanofiber diameter: red square is LDPE, green square is HDPE, black triangles are high MW P3HT, and electrochemically fabricated (PT) [116] are blue circles. Data from this work represent at least three repeat measurements for each sample type with error bars including uncertainty and variability.

The thermal conductivity of the H-P3HT for the 100 nm and 55 nm diameter nanofibers is high with average measured values of ~7 W/m-K and ~4.5 W/m-K, respectively. The thermal conductivity reported here for the 100 nm diameter H-P3HT nanofibers are nearly three times greater than the previously reported high for any P3HT material. These results exhibit a trend that is different compared to the report of Rojo et al. [110] and suggest that polymer fiber thermal conductivity does increase with decreasing nanopore diameter under these processing conditions. The reason for this significant differentiation is still unknown, but is likely due to the difference in processing where Rojo

annealed their nanofibers and due to the molecular weight difference in the polymers used. Beside annealing, Regioregularity will also significantly impact crystallinity with higher regioregularity resulting in higher crystallinity. It is surprising that the thermal conductivity decreases to approximately 4.5 W/m-K for the 55 nm fibers, where polarized Raman studies show that chain alignment increases with decreasing diameter and thermal conductivity is expected to also increase. An explanation for the decreased thermal conductivity for the smallest pore diameter could be that the template is not completely filled with polymer due to increased viscous effects, as will be discussed further in the proceeding sections.

3.5.3 Polarized Raman Measurements

Moreover, polarized Raman Spectroscopy is a proven method to measure polymer chain orientation (for both crystalline and amorphous regions) within polymer micro- and nanofibers. We measured the polarized Raman response of the PE fibers compared with PE films to examine polymer chain alignment and the resulting intensity vs. wavenumber plots are included below in Figure 28. The LPDE film was used to confirm that the intensity of the symmetric C-C stretching signal along the PE backbone at 1130 cm^{-1} is similar for both polarization directions for an unoriented sample. The average of three measurements were taken for the Spectra fiber samples in each polarization direction. The large ratio (I_{zz}/I_{xx}) of the symmetric C-C stretching signal along the PE backbone at 1130 cm^{-1} indicates a high degree of molecular alignment in the direction of the Spectra fiber's long axis, which further supports the extremely high measured thermal conductivity.

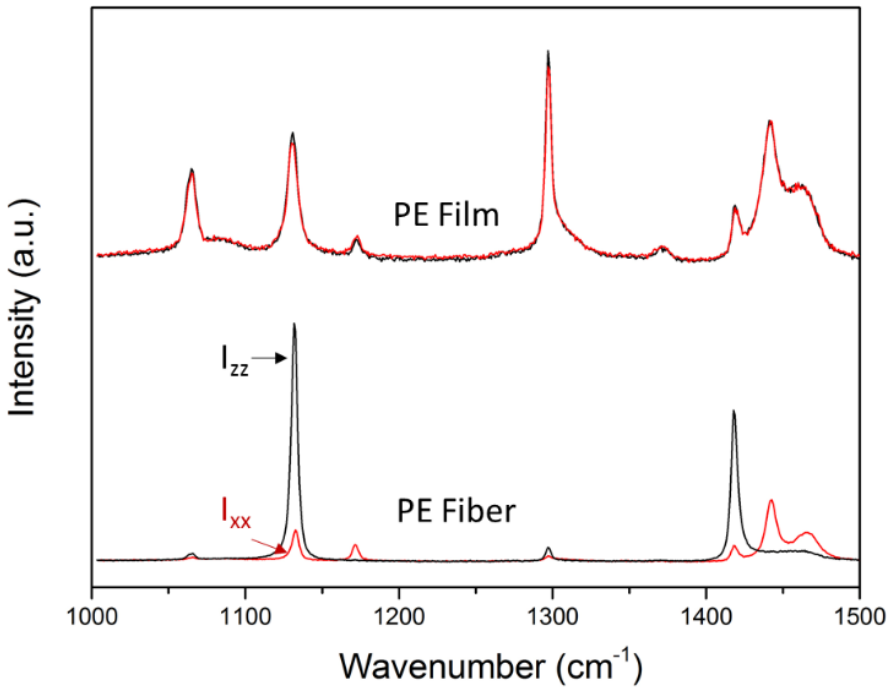

Figure 28. Comparison of intensity of I_{zz} and I_{xx} for isotropic PE film and highly aligned Spectra HDPE microfiber. The large intensity ratio (I_{zz}/I_{xx}) of the symmetric C-C stretching signal along the PE backbone at 1130 cm^{-1} indicates a high degree of molecular alignment in the direction of the fibers long axis.

Previously, the thermal conductivity of PE nanofibers fabricated through a simple solution drawing technique reached values as high as 8.8 W/m-K and Raman spectroscopy with a peak I_{1130}/I_{1060} ratio of ~5 was used to support the strong correlation between chain alignment and fiber thermal conductivity.[52] The highly drawn commercial PE fiber measured here demonstrates a significantly increased I_{1130}/I_{1060} ratio of over 40, suggesting much higher chain alignment and thermal conductivity.

As previously mentioned, the 1440-1450 cm^{-1} peak in the P3HT spectrum is associated with the symmetric C=C stretch vibration along the thiophene ring.[125] The

Raman Spectra for the 55 nm, 100 nm, and 200 nm P3HT nanofibers is included in Figure 29 below. General trends show an increase in polymer chain alignment with a decrease in nanofiber diameter. These results suggest that the I_{zz}/I_{xx} ratio increase from approximately 1.4 to 2.5 for the 200 nm to 55 nm fibers, respectively. This result further supports the trend that fiber thermal conductivity improves with decreasing diameter and the notion that the measured 55 nm fiber thermal conductivity is lower because of inadequate template filling, not because the fibers are lower thermal conductivity.

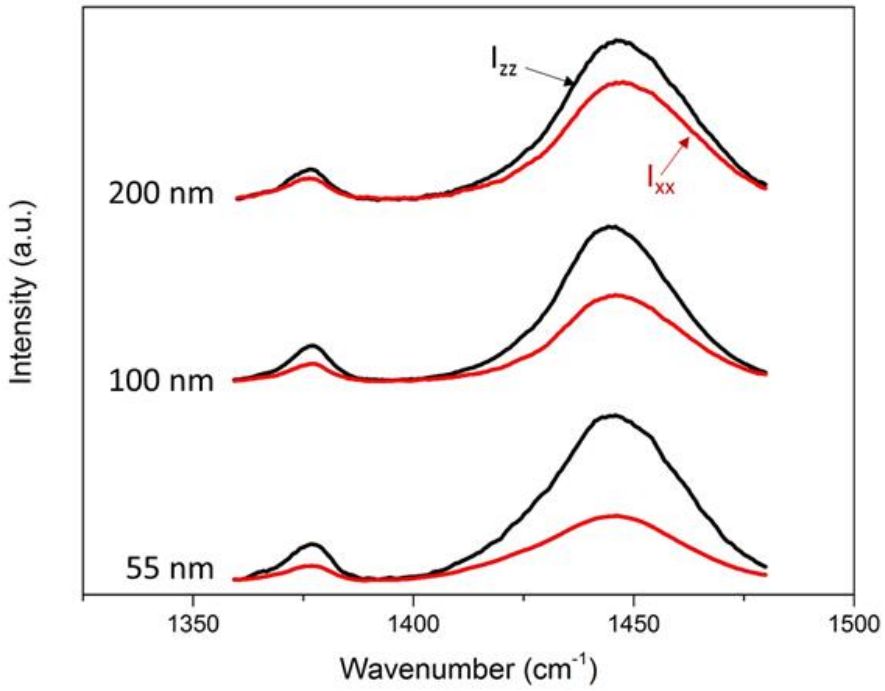

Figure 29. Polarized Raman Spectra for light polarized parallel (I_{zz}) and perpendicular (I_{xx}) to the long axis of the polymer nanofibers as a function of fiber diameter. An increase in the I_{zz} peak relative to the I_{xx} peak is an indication of increasing polymer chain alignment.

3.6 Conclusions

Here we demonstrate a straightforward method to achieve high thermal conductivity polymer nanofibers using melt infiltration of AAO templates. The upper end of the thermal conductivity of HDPE NF, ~9 W/m-K, is more than twenty times higher than bulk HDPE. The value of ~7 W/m-K is the highest known reported thermal conductivity for a conjugated polymer, which are promising for use in high temperature thermal management applications. LDPE provides a useful test material, although it should be noted that the poor thermal stability of LDPE makes it impractical for many real applications. It was observed that temperatures as low at 80°C will cause enough softening to deform the NFs. HDPE may provide sufficient thermal stability for certain low temperature applications and infiltrating the array with a second higher temperature polymer may extend the operating range even higher. Future studies will focus on the continued parameterizations to maximize thermal conductivity and structural studies to explain these interesting properties.

CHAPTER 4. HIGH THERMAL AND ELECTRICAL CONDUCTIVITY OF TEMPLATE FABRICATED P3HT/MWCNT COMPOSITE NANOFIBERS

4.1 Introduction

The trend of increasing power density in microelectronic components has accelerated the need for advanced thermal management materials. With heat fluxes ranging from 0.1-3 $kW \cdot cm^{-2}$ being expected in next generation silicon and wide band gap semiconductor electronics, the reduction of thermal resistances between interface joints is necessary to maintain lower device operational temperatures and to ensure system reliability.[131] This challenge is further escalated by the growing use of electronics in high temperature environments where the associated thermal stresses are extreme (automobiles, defense equipment, oil excavation, etc.). The ideal property combination for reducing interfacial resistance and maintaining system reliability is a mechanically compliant material with high thermal conductivity and chemical stability. In general, polymers, despite their favorable mechanical properties, suffer from drastically reduced thermal transport and isotropic bulk film polymers typically exhibit thermal conductivities in the range of 0.1-0.3 $Wm^{-1} \cdot K^{-1}$.[112] However, it is well known that polymer chain orientation impacts bulk properties and many techniques have been developed to improve chain alignment. Mechanical drawing, one of the earliest of these methods, was used to induce anisotropic thermal conductivity in bulk polymer systems as early as the 1960's.[132] More

recently, researchers have been investigating the use of nanoscale confinement to improve chain alignment through spatial restrictions and polymer-template surface interactions.[57, 68] For example, nanoporous anodic alumina oxide (AAO) templates, consisting of a nanoporous thin film of alumina filled with through-pores ranging from ~15-300 nm in diameter, can serve as a mold to create vertically aligned arrays of confined nanostructures.[56, 68, 117] Polymer nanotubes (PNTs) and nanofibers fabricated using nanoporous templates may display special microstructure orientation and enhanced electrical[68] and thermal[51, 56, 57] properties. Recently, highly conductive thermal interface materials (TIMs) were fabricated using electrochemically grown polythiophene nanotube arrays[56] and nanoconfined high density polyethylene nanofibers[57] with high thermal conductivity were fabricated using a unique melt technique assisted by mechanical vibration. The polythiophene derivative poly(3-hexylthiophene-2,5-diyl) (P3HT) is one of the most commonly studied conducting polymers due to its ease of processing and potential use in organic electronics. P3HT also exhibits a melting temperature above 200°C and is commercially available, enhancing suitability for commercial thermal management applications. Moreover, solution cast P3HT nanotubes[117] and melt processed nanofibers[58] have both demonstrated enhanced thermal conductivity.

Carbon nanotubes (CNTs) are one of the most widely studied materials of the past 20 years due to their phenomenal electrical, thermal, and mechanical properties.[133-135] The thermal conductivity of a carbon nanotube can be several orders of magnitude greater than polymers, in the range of 3000 $Wm^{-1}K^{-1}$.[136] Consequently, researchers have fabricated composite polymer/CNT materials with the goal of improving matrix transport and conjugated polymer/multiwall carbon nanotube (MWCNT) composites are actively being

developed for use in thermoelectrics,[137] organic photovoltaics,[138] and biomedical applications.[139] Similarly to the macromolecular chains confined in nanoporous templates, confined composite systems demonstrate anisotropic alignment of the MWCNTs that contributes to property enhancement in the direction of alignment.[140-142] The thermal conductivity of template confined composite nanofibers has not been reported, despite evidence that electrospun composite nanofibers may have thermal conductivities up to or greater than 20 $Wm^{-1}K^{-1}$.[143, 144] The primary advantage of template fabricated nanofibers as opposed to electro- and gel-spinning methods is that template methods produce large area, vertically aligned nanofiber arrays, whereas spinning methods generally result in disordered mats that need post-processing to achieve vertical alignment.[145]

Here we demonstrate a new method to fabricate composite nanofiber arrays with large concentration of high aspect ratio fillers, which has remained a significant challenge due to pore blocking of filler material and the difficulty in completely penetrating templates with small pore diameters. Our approach enables substantial enhancement to the thermal conductivity of nanoconfined polymer nanofibers. Using a simple sonication process, nanoporous alumina membranes are infiltrated with MWCNTs followed by polymer melt. The processing parameters can be altered to control the MWCNT wt% in the composite nanofiber and the array thermal conductivity and electrical transport properties are evaluated as a function of MWCNT content. An electrical two-point probe method is used to determine the current voltage behavior of the nanofiber array as a function of MWCNT content and thermal conductivity is measured using the photoacoustic (PA) technique.[107, 119, 146] Carbon nanotube % content and composite fiber thermal stability is determined using thermogravimetric analysis (TGA) and transmission electron microscopy (TEM) is

used to visualize the MWCNTs within the nanofibers. A range of approximately 3 wt% to 55 wt% MWCNT content is achieved with a peak nanofiber thermal conductivity of approximately 4.7 ± 1.1 $Wm^{-1}K^{-1}$ at 24 wt% MWCNT, which is more than double the thermal conductivity of pure polymer nanofiber[6, 7] and is nearly a 25-fold improvement over bulk film P3HT.[109] Although there is a growing body of literature exploring thermal conductivity in template fabricated polymer nanostructures, this is the first known report on the enhanced thermal conductivity of template fabricated composite nanofibers with carbon nanotube filler.

4.2 MWCNT/P3HT Composite Nanofiber Fabrication

A novel bath sonication process was developed to fabricate composite nanofibers with high filler loading dispersed throughout the length of the fiber. EmptyWhatman200 nm nominal pore diameter and 60 μm thick AAO templates are placed directly into a MWCNT/chlorobenzene dispersion under bath sonication (Figure 30a). The purchased Whatman AAO templates have a nominal pore diameter of 200nm and a rated porosity of 35-50%. However, it has previously been determined that the porosity and nominal pore diameter can be as large as 60% and 220 nm, respectively.[56] The templates were dipped in 1M KOH solution for 20 seconds before sonication to remove any residual surface films that may block pore openings. SEM images revealed insignificant pore widening after the 20 second etching process. The templates were then rinsed in DI water and allowed to dry in vacuum oven. The 1.5 wt% MWCNT/chlorobenzene dispersion was sonicated for 1 hour and then the dried AAO template was placed in the dispersion to undergo sonication for the prescribed time intervals. The MWCNTs were purchased from US Research

Nanomaterials, Inc. and used as purchased. Their specified diameter and length is less than 7 nm and 0.5-2 µm, respectively.

The sonication energy forces MWCNTs into the template nanopores and the sonication time and dispersion concentration are altered to control pore filling. Sonication is likely to break the MWCNTs into even smaller lengths[147] and forces both the short and long aspect ratio nanotubes into the small pore openings and disperses the nanotubes along the length of the nanopore (Figure 30c). Several other reports have explored the use of AAO templates to fabricate composite nanostructures,[140, 141] but this is the first study that presents a method to achieve a seemingly high weight percent filling (TGA results discussed later) and high MWCNT loading along the length of the nanofiber.

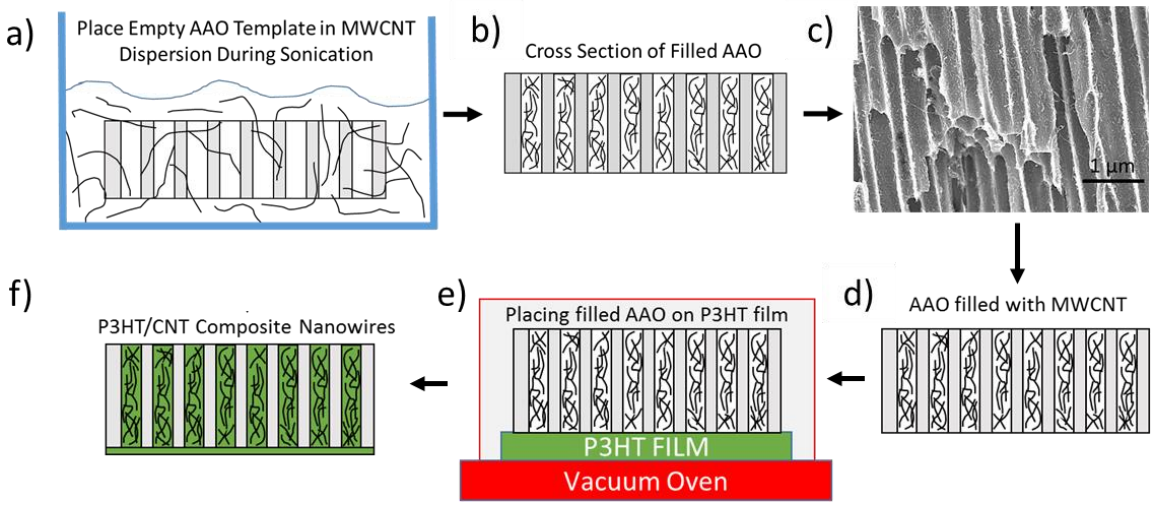

Figure 30. a)-c) displays the AAO sonication process and cross section after a 0.5 hour sonication in 1.5 wt% MWCNT dispersion. Steps d)-f) show the process used to melt infiltrate polymer into the MWCNT filled AAO template, illustrations b and d are the same.

Magnified SEM images along the entire length of the AAO cross section demonstrate the presence of MWCNTs throughout as illustrated in Figure 31. Although Figure 31c clearly illustrate the presence of MWCNTs on the AAO walls, a variation in

SEM contrast along the length of the cross section suggests a non-uniform MWCNT distribution. The contrast variation is due to arrangement of MWCNTs within the confining pores, where the MWCNTs have the tendency to bundle into clusters toward the middle of the template, as illustrated in Figure 31c. However, near the top and bottom of the template (about 15 µm into each side), the MWCNTs appear to demonstrate less clumping behavior.

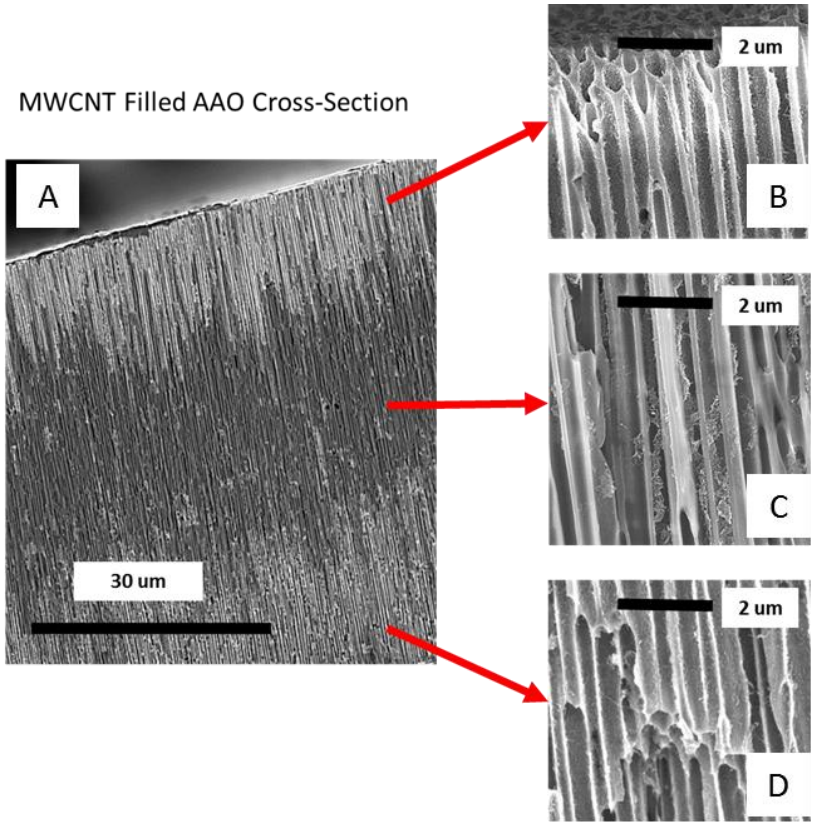

Figure 31. Image A displays the AAO cross section after a 3 hour sonication in 2.5 wt% MWCNT dispersion and images B, C, and D show the high magnification images on the top, middle, and bottom of the AAO template, respectively. MWCNTs can be seen throughout the length of the template.

The mechanism behind this unusual distribution is still not fully understood, but it may be due to the dynamics of the sonication method, where MWCNTs that penetrate deeper into the template are likely to bundle as sonication energy becomes less pronounced or upon drying where a liquid meniscus might pull MWCNTs into the middle of the AAO. TEM of the composite nanostructures could not resolve the same bundling effect and it is possible that the MWCNTs become better dispersed during polymer infiltration.

Figure 30d-f demonstrates the subsequent filling of the MWCNT infiltrated AAO templates with P3HT melt and SEM and TEM images of the released nanostructures before and after polymer filling are included in Figure 32. An SEM image of the released MWCNT bundle is included in Figure 32a and the corresponding TEM image is illustrated in Figure 32b. Likewise, SEM and TEM images are included in Figure 32c-d for the composite nanofibers after P3HT melt infiltration.

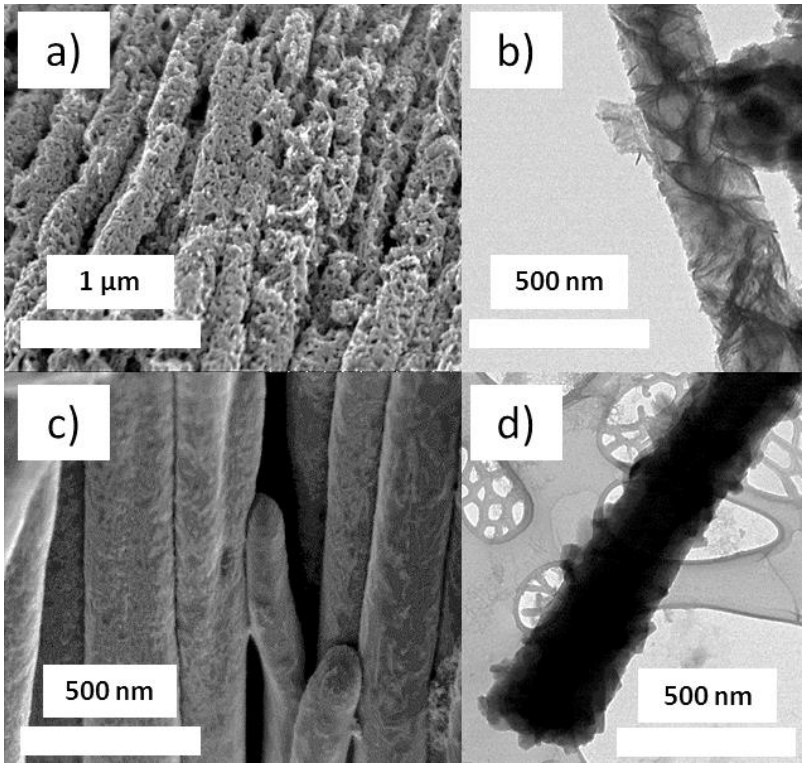

Figure 32. Nanostructure SEM and TEM images after removing the AAO template before melt infiltration (a-b) and after the AAO is melt infiltrated with P3HT in a vacuum oven (c-d).

The polymer melt process is performed by placing the MWCNT filled AAO template on top of bulk P3HT flakes in a vacuum oven at 260 °C (N_2 atmosphere). After 45 minutes the template is removed and quenched in deionized water to minimize thermal degradation and to preserve molecular alignment. The 45 minute infiltration time is the minimum required time for sufficient infiltration. It was selected through initial experimentation where it was found that impartial nanopore filling could occur at lower infiltration times, especially in the composite samples where MWCNTs partially block the pores. During the quenching process, the bulk of nanofibers are protected from water exposure by the AAO template and back polymer film, which is later removed. The samples were not annealed after melt infiltration in contrast to methods previously

reported.[54, 110] Annealing is avoided purposely under the anticipation that recrystallization may undo confinement induced alignment, which has been reported to significantly reduce thermal transport in electrospun nanofibers.[54] Figure 32 illustrates the resulting nanostructures when the AAO template is removed before and after P3HT melt infiltration. Interestingly, pure MWCNT bundles can be released from the template and they maintain their structure without the need for a reinforcing polymer matrix (only for longer sonication times with significant MWCNT infiltration). This observation suggests potential for high composite thermal conductivity because values as high as 150 $W \cdot m^{-1}K^{-1}$ in MWCNT bundles have been reported.[148]

4.3 Thermal Gravimetric Analysis of Composite Fibers

A two-step thermogravimetric analysis (TGA) process is described to determine MWCNT content in wt% using a TA Instruments SDT Q600 thermogravimetric analysis system. The AAO/nanofiber composite samples were crushed and placed directly into the TGA pan for analysis. The composite nanofibers are cycled from 150°C to 700°C at a heat rate of $10°C min^{-1}$ first under nitrogen atmosphere and subsequently under air without removing the sample. P3HT flakes and MWCNT powder samples are measured individually to verify the percent weight loss of each under nitrogen and air atmosphere. P3HT lost approximately 73% mass in nitrogen (**33**), which agrees well with past reports of inert P3HT thermal decomposition.[149] The P3HT in air undergoes a decomposition process that involves an initial mass loss peak due to the degradation of the alkyl side chain

and the second mass loss peak is a result of the thermos-oxidative decomposition of the chain backbone.

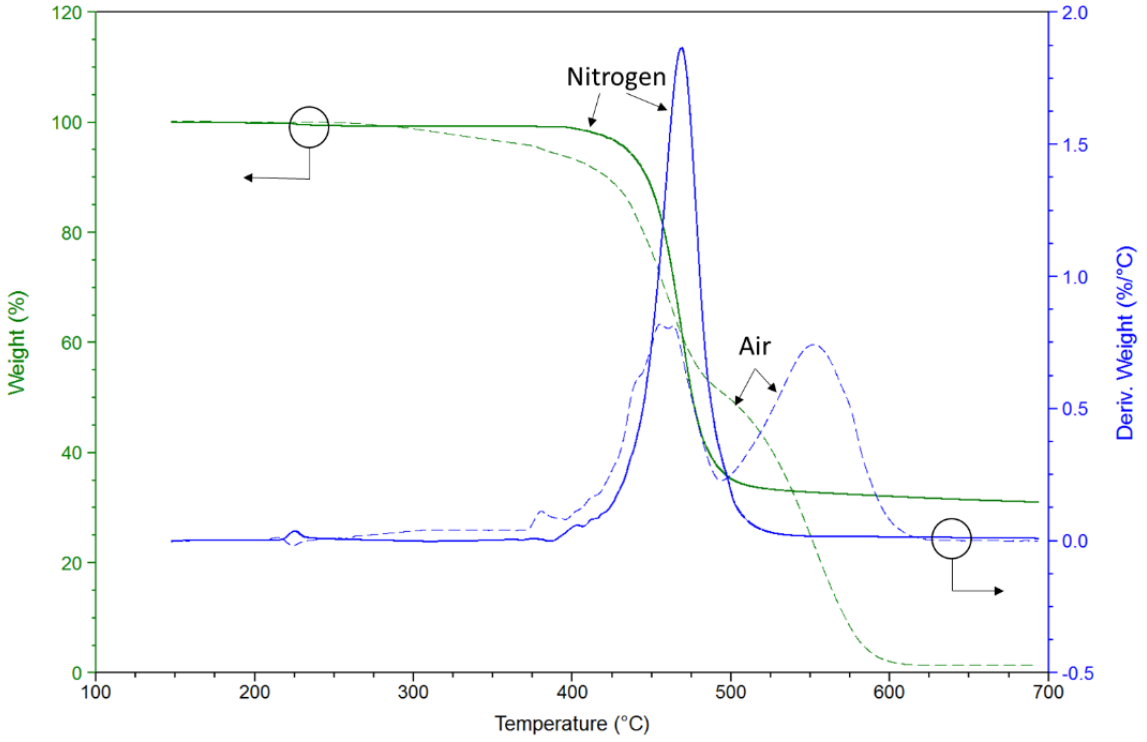

Figure 33. TGA plot of the P3HT flakes in both air (dashed) and nitrogen (solid) atmospheres. The weight loss percent and the derivative of the weight loss with respect to temperature is illustrated for both scans.

The MWCNTs are stable in inert conditions and only lose a small percentage (~5 wt%) of impurities (Figure 34) under nitrogen. Hence, the composite sample weight loss in nitrogen is primarily due to a single step polymer decomposition process where only ~30% residual mass (RM) of the polymer species is left when heated past 600°C.[150] Upon reheating the polymer RM and MWCNTs in air, approximately 95% of the remaining

weight is lost indicating full decomposition of both constituents. The residual mass of as received P3HT flakes and MWCNT powder after decomposition in each atmosphere was used to formulate Equation 6 and Equation 7.

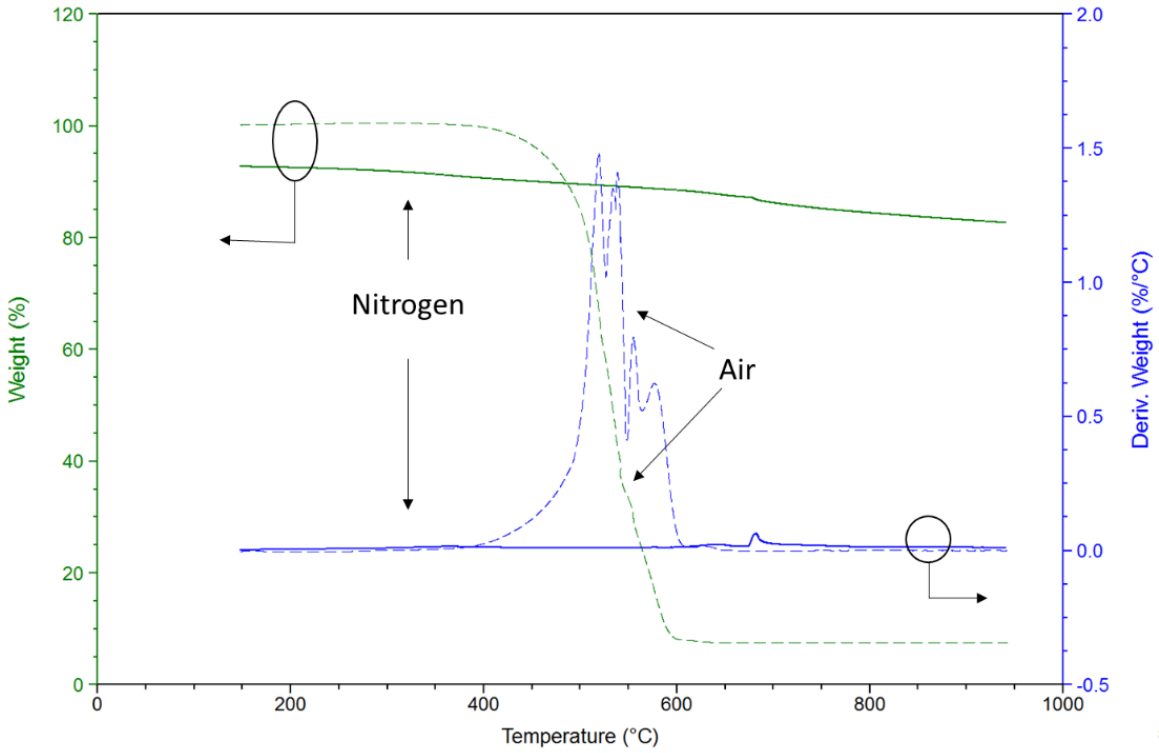

Figure 34. TGA plot of the MWCNT powder in both air (dashed) and nitrogen (solid) atmospheres. The weight loss percent and the derivative of the weight loss with respect to temperature is illustrated for both scans.

Figure 35 outlines the results of TGA analysis for P3HT nanofibers (Figure 35a) and for composite nanofibers (Figure 35b) fabricated using MWCNT infiltrated AAO template (AAO was placed in MWCNT dispersion for 50 minutes). As the wt% of MWCNTs is increased, more total mass is lost during the heating cycle in air atmosphere

relative to the mass lost during the initial heating cycle in nitrogen. For both samples, the large residual mass after TGA in air is the remaining weight of the AAO template. The derivative of weight with respect to temperature varies significantly between samples in air atmosphere (Figure 35a and Figure 35b) and Figure 35c illustrates this trend across all sonication times. In air atmosphere, the peak mass loss temperature shifts from approximately 525°C to 575°C as the sonication time increases. This shift occurs because a larger percentage of MWCNTs are present at the longer sonication times and hence the peak associated with maximum MWCNT mass loss rate becomes more pronounced.

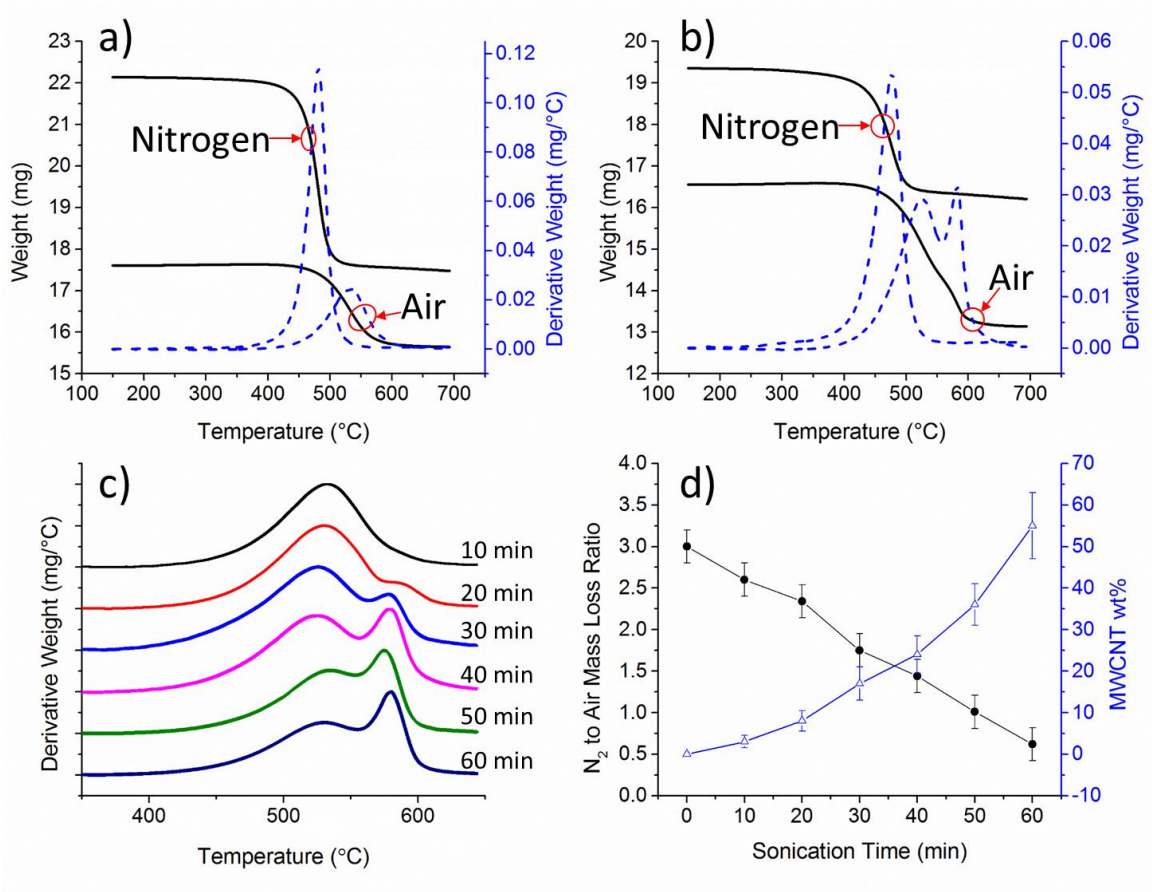

Figure 35. TGA weight loss and derivative of weight with respect to temperature for a) P3HT nanofibers and b) MWCNT/P3HT composite nanofibers fabricated after sonication for 50 minutes. c) The derivative of weight with respect to temperature for the 10 – 60 minute sonicated samples heated in air atmosphere. d) Weight loss ratio for mass loss in nitrogen to mass loss in air for the 10 – 60 minute sonicated samples and their calculated MWCNT wt%. Error bars represent the standard deviation of three trials.

Equation 6 and Equation 7 are derived experimentally through a series of TGA measurements and are used to determine the mass of P3HT (M_{P3HT}) and the mass of MWCNT (M_{MWCNT}) as a function of the composite mass loss under nitrogen atmosphere (ΔW_{N2}) and the corresponding mass loss in air atmosphere (ΔW_{Air}). The coefficients for the system of two linear equations are derived using the aforementioned TGA results for

mass loss of MWCNT powder in nitrogen (~5%) and air (~95%), as well as mass loss of P3HT flakes in nitrogen (~73%) and air (~27%). However, because only ~95% of total mass is lost in air for both samples (~5% residual mass remained), each coefficient is multiplied by 0.95 in Equation 7 to account for residual mass.

$$\Delta W_{N_2} = 0.73(M_{P3HT}) + 0.05(M_{MWCNT}) \quad (6)$$

$$\Delta W_{Air} = 0.95(1 - 0.73)(M_{P3HT}) + 0.95(1 - 0.05)(M_{MWCNT}) \quad (7)$$

Figure 35d displays the resulting calculations for each sonication time where the samples sonicated for 10 to 60 minutes demonstrate a MWCNT wt% of approximately 3 wt% to 55 wt%, respectively. The ratio of total weight lost in N_2 as compared to air is an indication of the presence of MWCNTs where a ratio of approximately 3 to 1 corresponds to polymer material with no MWCNTs and a ratio of ~ 0.5 corresponds to ~55 wt%. Assuming MWCNT density of 1.5 g/cm^3 and P3HT density of 1.1 g/cm^3,[151, 152] the estimated MWCNT to P3HT volume fraction ranges from approximately 2 vol% to 40 vol%. As the sonication time increases the MWCNT wt% increases significantly and begins to exhibit exponential growth behavior after a sonication time of 40 minutes. SEM images (Figure 36) indicate that the exponential growth occurs at longer sonication times because the MWCNTs begin to block the nanopores and prevent filling of polymer. Hence,

additional MWCNTs further block entry of the polymer species and the system of linear equations breaks down, resulting in artificially high wt% estimations.

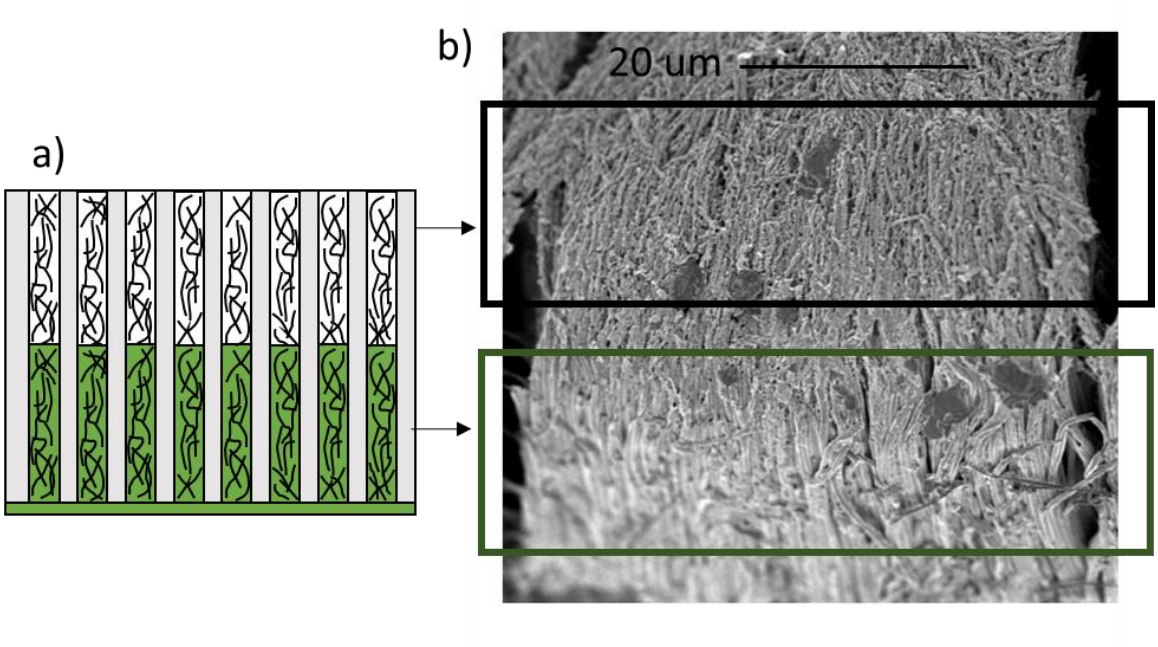

Figure 36. a) simple illustration to demonstrate partial P3HT filling into the MWCNT filled AAO template. b) SEM image demonstrating the presence of composite structures (green box) and MWCNT bundled structures (black box) along the material cross section.

It is worth noting that larger MWCNTs (5-15 μm long) resulted in insignificant pore penetration under identical processing conditions, although we do anticipate that higher aspect ratio fillers would further enhance the transport properties. In addition, a sonication time of greater than 2 hours resulted in the gradual destruction of the AAO template and small deviations from the prescribed processing conditions can result in little to no MWCNT filling of AAO template. For example, lower dispersion concentrations resulted in poor template filling.

4.4 Thermal and Electrical Transport Measurements

The photoacoustic (PA) method and a two-probe electrical method are utilized to measure the thermal conductivity and current-voltage characteristics of the composite nanofibers, respectively. The PA method is well established and has previously been used to measure the thermal conductivity of thin films and nanostructured materials.[107, 146] A further explanation of the thermal measurements and uncertainty can be found in our prior work[117, 119, 146] Here, the thermal conductivity of the composite nanofibers embedded in the AAO is measured and a simple rule of mixtures (ROM) calculation is performed to estimate fiber conductivity assuming 100% template filling and a template porosity of 50%, following methods reported previously.[110, 116] The assumption of 50% porosity is at the upper end of the manufacture specifications, but is similar to what has been verified using SEM image analysis software. Under the assumption of 100% template filling, the resulting volume fraction (V*f*) of the nanofibers is 50%. The ROM calculation is provided below as Equation 8,

$$k_{com} = k_{fiber}(Vf) + k_{AlO2}(1 - Vf) \quad (8)$$

where k_{com} is the measured composite thermal conductivity, k_{fiber} is the nanofiber thermal conductivity, and V*f* is the nanofiber fill fraction. To determine the alumina thermal conductivity (k_{AlO2}) an empty AAO template was measured (~0.65 ± 0.1W/m-K, **Figure 37**) using the PA technique resulting in a calculated alumina conductivity of 1.3 $Wm^{-1}K^{-1}$, which agrees well with the previously reported value of 1.38$Wm^{-1}K^{-1}$.[110]

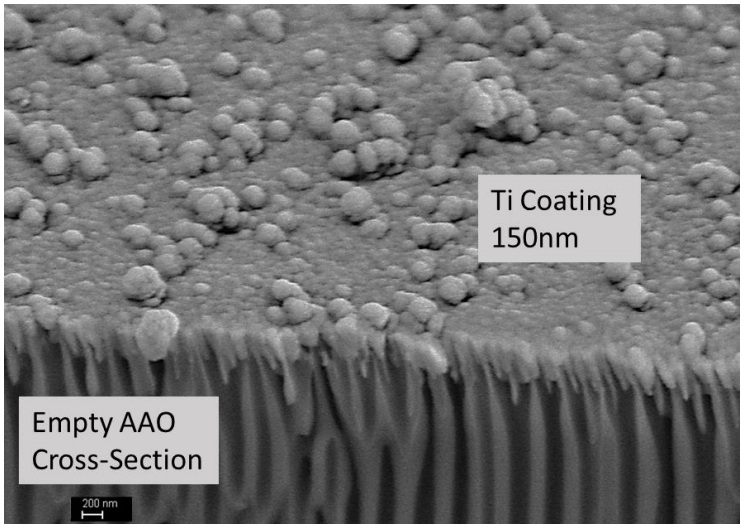

Figure 37. Cross section of empty AAO template with sputtered Ti coating used to measure the thermal conductivity of alumina template.

Figure 38 illustrates the acoustic phase shift of the 40 minute sonicated composite nanofiber/AAO sample as a function of modulation frequency. The experimental data is plotted in addition to the error bars corresponding to ± 0.5 degree phase shift to account for experimental error. The uncertainty for each thermal measurement in this manuscript (Δ_{total}) is derived from the data fitting uncertainty (Δ_{fit}) and the measurement uncertainty (Δ_{meas}) as described in section 2.4.

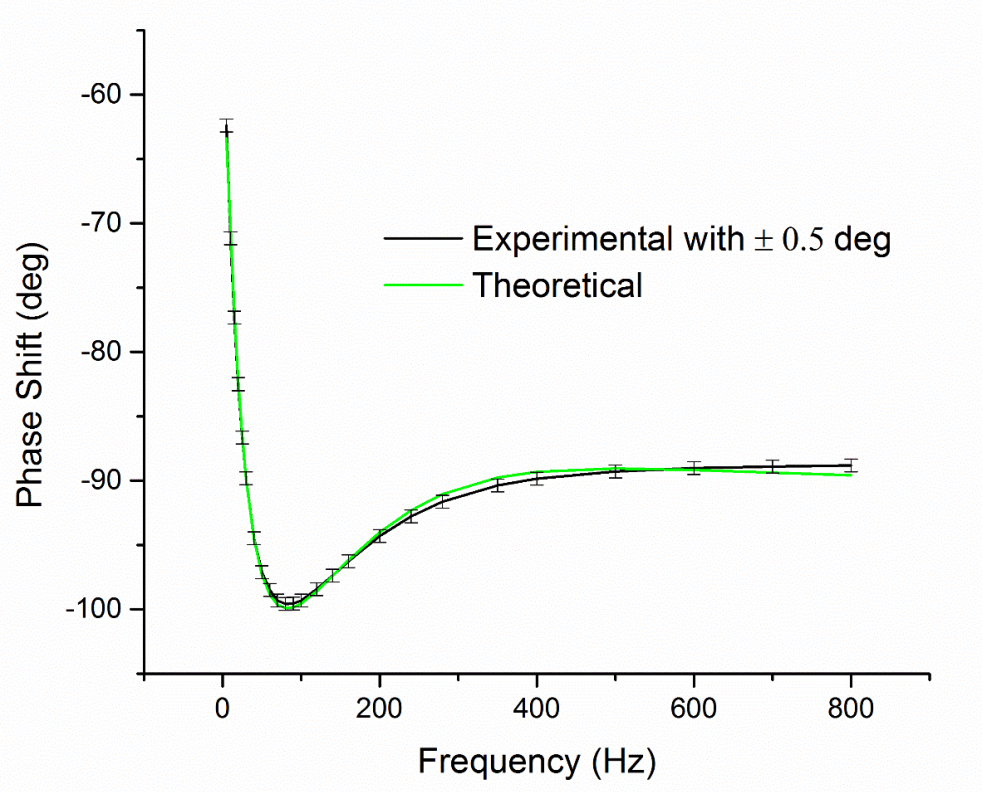

Figure 38. Theoretical and experimental phase shift of the 40 minute sonicated AAO/nanofiber composite sample with a ± 0.5 degree phase shift.

Table 5 provides the material properties and fitting parameters used in the photoacoustic measurements. In Table 5 *k* is thermal conductivity, *c* is the specific heat capacity, Thick is the layer thickness, OAL is the optical absorbance length, Con Res is the contact resistance between interfaces, and TD is thermal diffusivity. The four unknown values that were fit for in the model were the thermal conductivity of the nanofiber/AAO composite ($k_{NW\text{-}AAO}$), the specific heat of the nanofiber/AAO composite ($c_{NW\text{-}AAO}$), the contact resistance between the silicon and nanofiber/AAO composite ($R_{Si\_NW\text{-}AAO}$), and the contact resistance between nanofiber/AAO composite and the top layer of titanium that was sputtered onto the sample to help laser absorption ($R_{NW\text{-}AAO\_Ti}$).

Table 5. Fitting parameters and material properties used for photoacoustic data fitting. The green highlighted boxes represent the unknown values that were fit for in the model.

	Density	*k*	*c*	Thick	OAL	Con Res	Layer Res	TD
	kg/m³	W/m-K	J/kg-K	µm	µm	mm²-K/W	mm²-K/W	mm²/s
Si	2320	148	710	550	1.0E-03	37	3.72	89.85
Nanofiber /AAO	2450	2.97	950	60	1.0E-02	3.1E-02	20.21	1.28
Ti	4500	4.50	522	0.20	2.6E-02	1.0E-06	0.04	1.92
He	0.38	0.15	5190	0.00	1.0E-03	0.0E+00	0.00	76.27

The model sensitivity to perturbations in each of these parameters over the measurement frequency range is illustrated below in Figure 39. The sensitivity analysis was performed by changing a property value by ± 1% and then recalculating the phase. The larger the sensitivity, the larger the change in the phase in response to a change in a property value. As illustrated, our measurements have high sensitivity to the measured property values over the experimental frequency range.

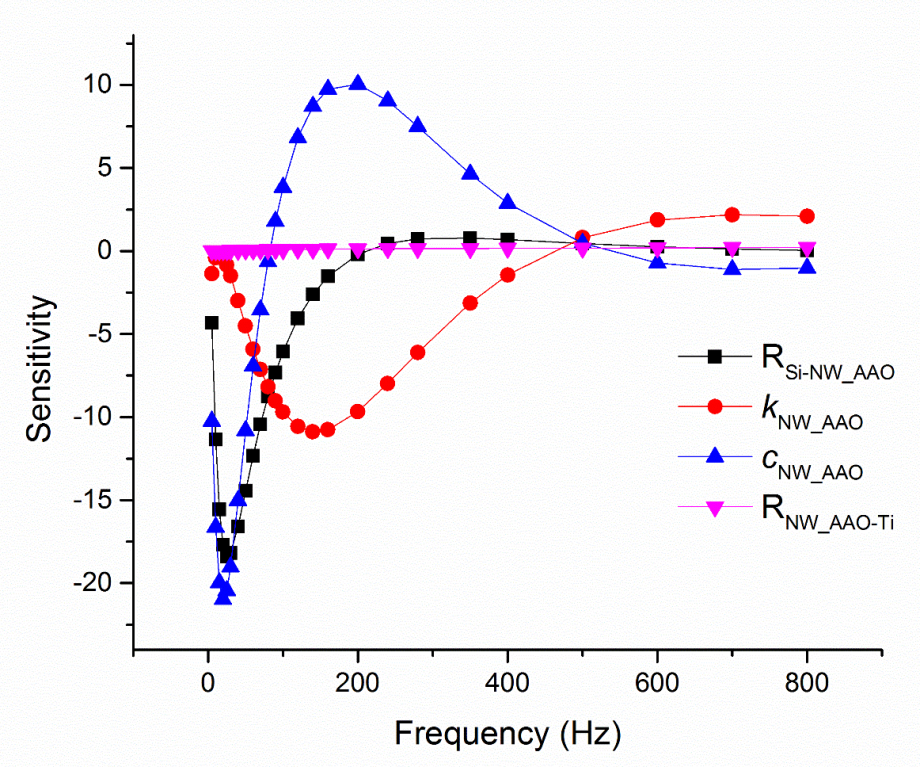

Figure 39. Sensitivity analysis to determine the model sensitivity to the unknown fitting parameters.

The DC current-voltage relations were measured at room temperature using a Keithley 2450 source meter connected to a DC electrical probing station. The infiltrated templates were patterned with 200nm thick gold contacts on both sides (top and bottom) and voltage of 0-2 volts was applied across the nanofibers. The resulting current response was measured and the current density was calculated using the contact surface area. The individual nanofiber electrical conductivity was then estimated assuming a fill fraction of 50%. The current density as a function of applied voltage was calculated using the gold contact diameter and the AAO nanopore fill fraction (~50%).

4.5 Results and Discussion

Figure 40 demonstrates the relationship between sonication time, dispersion concentration, thermal conductivity (Figure 40a) and the current density (Figure 40C) of the MWCNT/P3HT composite nanofibers. The AAO/nanofiber composite thermal conductivity increases with increasing MWCNT wt% and peaks at approximately 3 ± 0.5 $Wm^{-1}K^{-1}$ after a sonication time of 40 minutes and at 24 wt% MWCNT composite nanofibers. Without MWCNT the AAO/nanofiber composite thermal conductivity is approximately 1.8 ± 0.4 $Wm^{-1}K^{-1}$. The calculated nanofiber thermal conductivity ranges from 2.3 ± 0.5 $Wm^{-1}K^{-1}$ to 4.7±1.1 $Wm^{-1}K^{-1}$ for the 0 wt% and 24 wt% MWCNT samples, respectively. With a thermal conductivity of over 2 $Wm^{-1}K^{-1}$, our melt processed nanofibers are significantly more conductive than previously reported for similar P3HT nanofiber diameter.[110] As mentioned, this is likely because our process avoids thermal annealing, which has been shown to decrease chain alignment parallel to the tubes vertical axis and may greatly reduce nanofiber thermal conductivity.[54] In addition, the P3HT used in the current study has an estimated number average molecular weight of 88,000 g mol^{-1} whereas the authors in the aforementioned study report a Mn of 33, 405 g mol^{-1}, hence the increased chain length may result in more significant confinement effects and may have significantly different levels of crystallinity. Past 40 minutes of sonication the thermal conductivity drops significantly due to the previously discussed phenomenon of MWCNT pore blocking and partial polymer infiltration.

Previous studies indicate that phonon scattering at the interface between MWCNTs and polymer matrix limits thermal transport, which results in less significant improvements in thermal conductivity than would be expected through simple effective medium theory

analysis.[153] The P3HT matrix and MWCNTs are coupled strongly through π–π interactions, resulting in polymer chain wrapping around MWCNT in solution[154] and enhanced crystallinity and conjugation length in solid films.[155] However, the relationship between these effects and thermal conductivity in conjugated systems is not yet fully understood. On the other hand, polymer chain and MWCNT alignment parallel to the nanofibers long axis is expected to improve thermal conductivity and reduce the degree of interfacial phonon scattering in the composite system. Our results and previously reported orientation investigations in similar systems[140, 142] suggest that confinement induces polymer chain/MWCNT co-alignment along the backbone of the nanofiber, drastically improving thermal conductivity.

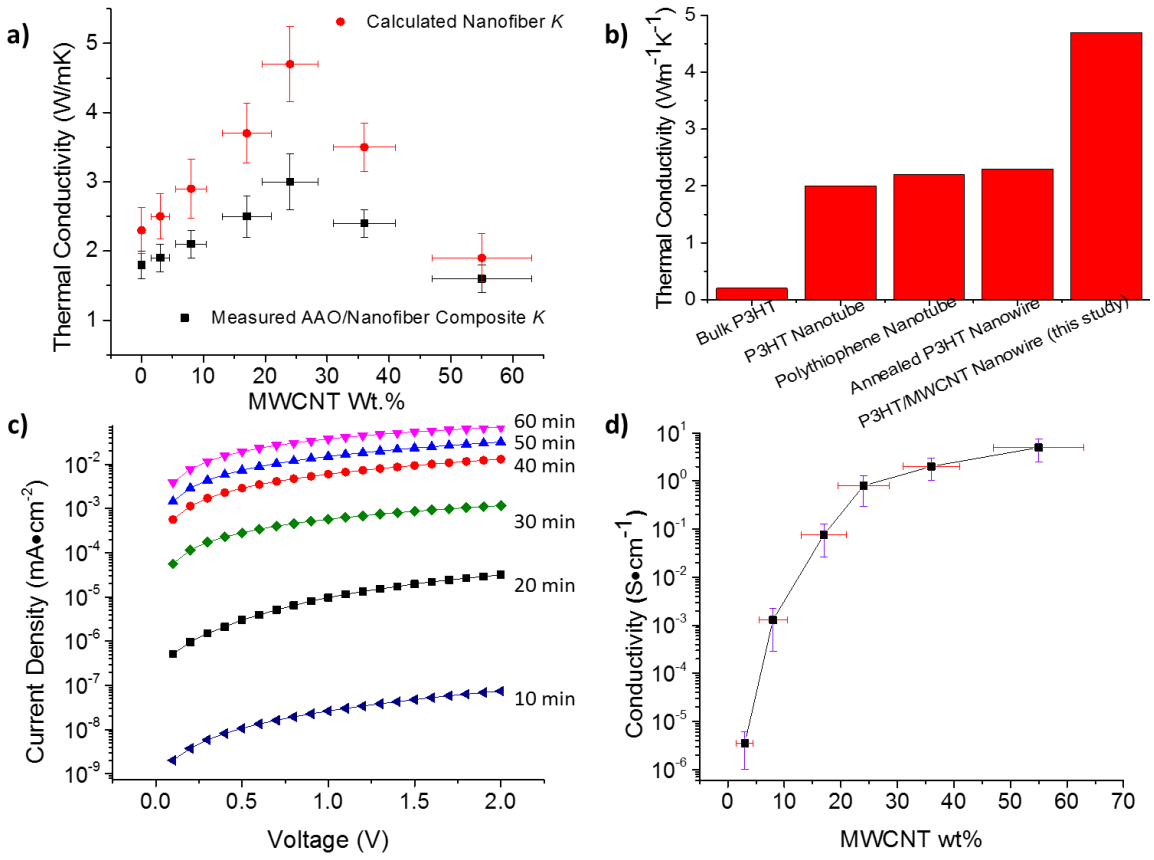

Figure 40. a) AAO/nanofiber composite and calculated nanofiber thermal conductivity as function of MWCNT wt%. b) Comparison of the thermal conductivity of published polythiophene (electrochemically processed) and derivative P3HT nanostructures (melt and solution processed) fabricated using template methods. c) Current density as a function of applied voltage for samples that were sonicated for 10-60 minutes at 10 minute intervals. d) Estimated electrical conductivity of composite nanofibers as a function of MWCNT wt% (based on approximated area density of nanofibers).

Figure 40b displays the reported thermal conductivity of bulk (isotropic) P3HT,[109] ~220 nm diameter rr-P3HT nanotube,[117] ~220 nm diameter polythiophene nanotube,[56] ~350 nm diameter annealed P3HT nanofiber array,[110] and the thermal conductivity of the ~220 nm diameter composite nanofibers made in this study. The calculated thermal conductivity of the 24 wt% composite nanofiber is greater than 2x the thermal conductivity

reported for polythiophene nanofibers. This result strongly contrasts a previously described trend of decreasing thermal conductivity of CNT/P3HT composite films with increasing CNT wt%.[137] This is most likely due to poor CNT dispersion in the referenced work. Here, the observed increase in thermal conductivity of composite fibers relative to pure polymer nanofiber is moderate considering the high MWCNT wt%. For example, it is common to observe a 3x improvement in composite conductivity at MWCNT fill fraction less than 10 vol%.[20] Our relatively moderate improvement is likely a result of the small aspect ratio of our fillers and sonication mediated defect formation. Also, the contribution of the highly conductive MWCNT species becomes less significant as the polymer matrix thermal conductivity improves.

The current and voltage relations of the composite nanofibers are measured using a simple two-probe method.[156] The current density increases with MWCNT content (Figure 40c), resulting in a current density range that spans over six orders of magnitude and agrees well with what has been reported for MWCNT/P3HT composites.[137, 157] The presence of MWCNTs significantly improves the electrical transport of the nanofibers as compared to pure P3HT nanofibers. The P3HT nanofibers demonstrated a current density of approximately 2 $nA \cdot cm^{-2}$ at 1 volt which is nearly 7 orders of magnitude lower than the most conductive composite samples. The composite nanofiber current density measurements suggest electrical percolation behavior occurs after approximately 40 minutes of sonication. The onset of percolation behavior coincides with the highest measured thermal conductivity values, however, the estimated fiber electrical conductivity continues to increase even as thermal conductivity begins to drop. The continued increase in electrical conductivity suggests that the polymer matrix plays an insignificant role in

charge transport at larger MWCNT content. In addition, the onset of electrical percolation behavior, observed above 20 wt% of MWCNTs, occurs at relatively high wt% compared to past studies.[137] The delayed occurrence of percolation indicates that at shorter sonication times the MWCNTs may infiltrate the AAO only near the top and bottom surfaces, as supported by SEM observations.

4.6 Conclusions

P3HT/MWCNT composite nanofibers are fabricated using the dispersive energy of a sonication bath and sonication time is manipulated to control MWCNT wt%. Nanofibers with approximately 24 wt% MWCNT exhibit a thermal conductivity of 4.7 ±1.1 $Wm^{-1}k^{-1}$, which is the highest measured thermal conductivity for P3HT/MWCNT composite material. Although CNT/polymer composite thermal conductivity is typically hindered by interfacial phonon scattering, the results of this study suggest interfacial scattering has been greatly reduced due to nanoconfinement induced alignment of both the MWCNT and the polymer chains. In addition, electrical percolation and high electrical conductivity are observed in nanofibers with greater than 20 wt% MWCNT, which serves as an indication that MWCNTs are present throughout the nanofiber length. The simple methods described here can be replicated to fabricate a wide variety of polymer composite nanostrucutres that may exhibit special mechanical and thermal properties as compared to their bulk or nanostructured counterparts. The observed enhancement in thermal conductivity may lead to the development of next generation thermal interface materials that exhibit "soft" mechanical properties and enhanced thermal transport, while the significantly improved electrical properties may be interesting for thermoelectric applications.

CHAPTER 5. THERMAL CONDUCTIVITY ENHANCEMENT OF LASER INDUCED GRAPHENE FOAM UPON P3HT INFILTRATION

5.1 Introduction

The trend of Thermal management of electronic devices is a burgeoning challenge due to their increased power consumption and reduced weight and size requirements, which ultimately result in high power density. In most electronic packages, there exists interfaces where heat generating components must be connected to heat sinking materials using thermal interface materials (TIMs). TIMs enhance the thermal conductance from one component to the other by filling in air gaps (caused by microscopic surface roughness and tolerance mismatch) that would otherwise form thermally insulating air pockets and most commercial TIMs are composed of polymer matrix infiltrated with high conductivity filler. While the specific application greatly influences the desired material properties, it is generally ideal for thermal interface materials to be mechanically compliant (soft) and have high thermal conductivity.[2] "Softness" (or the ability to deform under pressure) allows TIMs to fill in surface roughness crevices and improve the effective heat transfer between substrates; however, soft materials with high thermal conductivity are difficult to manufacture due to the low intrinsic thermal conductivity of polymers, typically between 0.1 - 0.5 W/m-K[112] (with the exception of recent efforts to increase the thermal conductivity of pure polymer, where up to 1.5 W/m-K has been achieved using engineered interchain, heat conducting bonds[158]). To overcome this challenge, commercial TIM manufacturers and academic researchers generally fill the polymer matrix with thermally conductive

particles such as boron nitride or aluminum oxide particles (for electrically insulating applications)[159, 160] or various forms of carbon such as carbon fibers,[18] carbon nanotubes,[161] and graphene flakes[162] and metals including Ag[163] (for applications where electrical isolation is less critical). Although the aforementioned filler particles exhibit large thermal conductivities, the effective increase in composite thermal conductivity can be low because of poor particle dispersion and contact resistance, which includes both phonon scattering at the polymer matrix and filler particle interface and voiding or incomplete wetting of the particle surface.[164] To achieve significantly enhanced through plane (z-axis) thermal conductivity, the resultant composite material requires high filler particle concentration, to the point where filling begins to compromise mechanical properties, processability, and greatly increases material cost. For example, even at filler particle volume fractions above 50 vol% the effective through plane thermal conductivity is still often an order of magnitude or more below the thermal conductivity of the filler particles.[165, 166]

Porous graphite and graphene foams (GF) with a three-dimensionally connected network of graphene (or graphite) ligaments have been investigated to provide high through plane thermal conduction as free standing foams or when combined with secondary polymer to form a composite.[34, 167] The percolated skeletal carbon ligaments (the 3D carbon network that comprises the graphene foam structure) provide heat transport pathways with no interfacial contact points and hence reduced interfacial phonon scattering, and graphene foam composite systems have demonstrated ligament thermal conductivities greater than 1600 W/m-K.[33] In addition, free standing graphene foams, with ligament thermal conductivity estimated to be 500 W/m-K, have demonstrated high effective thermal conductivity under compression and exceptional performance in thermal

interface applications.[39] However, expensive, high temperature and time consuming CVD or pyrolytic methods are often used to fabricated graphene foams, pricing graphene foam based TIMs out of the commercial market[33, 34, 39, 167] (high performance TIMs typically sell for between \$0.5-\$5.00/in^2 whereas graphene foams are currently sold for greater than \$50/in^2 (Graphene Supermarket)).

Here we investigate thermal transport in low cost laser induced graphene (LIG) foam and LIG/poly(3-hexylthiophene-2,5-diyl) (P3HT) composites fabricated through laser ablation and drop casting methods. The polymer P3HT has high temperature stability (melting point above 200 °C) and strong pi-pi interactions with graphene structures, which allows for good foam wetting and infiltration.[65] The thermal conductivity of bare LIG foam is measured as a function of laser power and then thin coatings of P3HT are incrementally added to the LIG foam network and an unusually high increase in thermal transport is observed. These interesting results serve to further the conversation of graphene foams and composites for thermal management applications.

5.2 LIG Foam Structural and Thermal Characterization

LIG foams are produced using a simple laser fabrication technique described previously.[66] In short, the foams are manufactured from commercially available 130 μm thick Kapton polyimide (PI) sheets using a CO_2 infrared laser where laser irradiation results in the photothermal conversion of sp^3-carbon atoms to sp^2-carbon atoms, and the formation of a 3-dimensional graphene network on the surface of the PI film. The CO_2 laser power is altered to control the degree of graphitization and resultant graphene foam thickness and

porosity.[66] The entire process is performed under ambient conditions for the conversion of PI films into porous graphene foam where the porosity originates from the outgassing during the high temperature laser process. The LIG process is unique to a small class of polymers, particularly those that bear the aromatic and imide repeat units due to an overlap of the 10.6 μm CO_2 laser line with an absorbance shoulder in the PI.

For this study, the laser duty cycle is adjusted from 4% to 10% in 2% increments using a 60 W peak laser, operating in pulse width modulation (PMW) at 6 kHz and laser spot size of 100 μm. As laser power density increases, the LIG thickness on the surface of PI film increases and the porosity increases. Figure 41 below illustrates the LIG foam surface as a function of laser power.

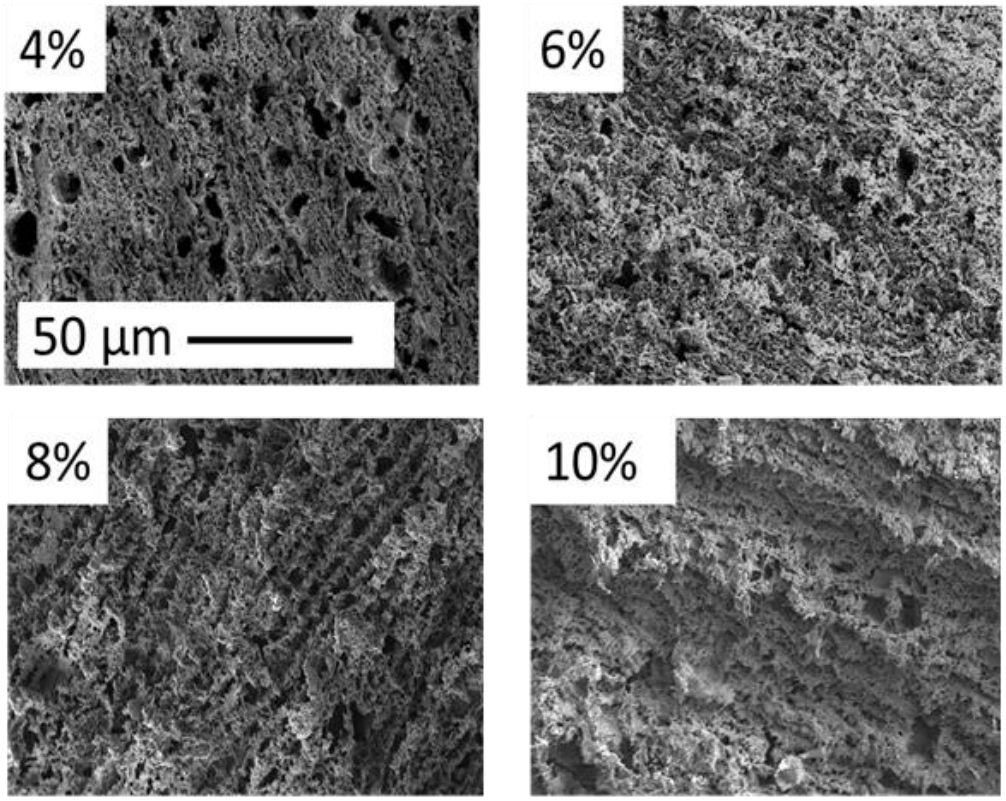

Figure 41. SEM images of the LIG surface as a function of laser duty cycle. These images illustrate that the PA thermal measurement is suitable for these samples as surface voids are significantly smaller than the PA laser spot size (1mm in diameter). Scale bar applies to all images.

The resultant LIG thermal conductivity is measured as a function of laser power using the photoacoustic (PA) method. The PA method (described in detail in Chapter 2) is a photothermal measurement procedure where a modulated laser strikes the surface of a material housed in a pressurized chamber and as the sample surface heats, it conducts heat into the gas near its surface and the gas expands sending acoustic waves throughout the chamber.[119] The phase and amplitude of the acoustic signal is then compared to a reference material and a one-dimensional heat conduction model is used to determine the materials

thermal properties.[168] Further information regarding the PA measurement technique, model fitting parameters, and sample preparation can be found in our previous publications.[62, 71, 117] For the PA measurement, the LIG and PI film thickness (LIG is formed on the surface of a PI film) were recorded as a function of laser power using cross-sectional SEM imaging, as demonstrated below in Figure 42.

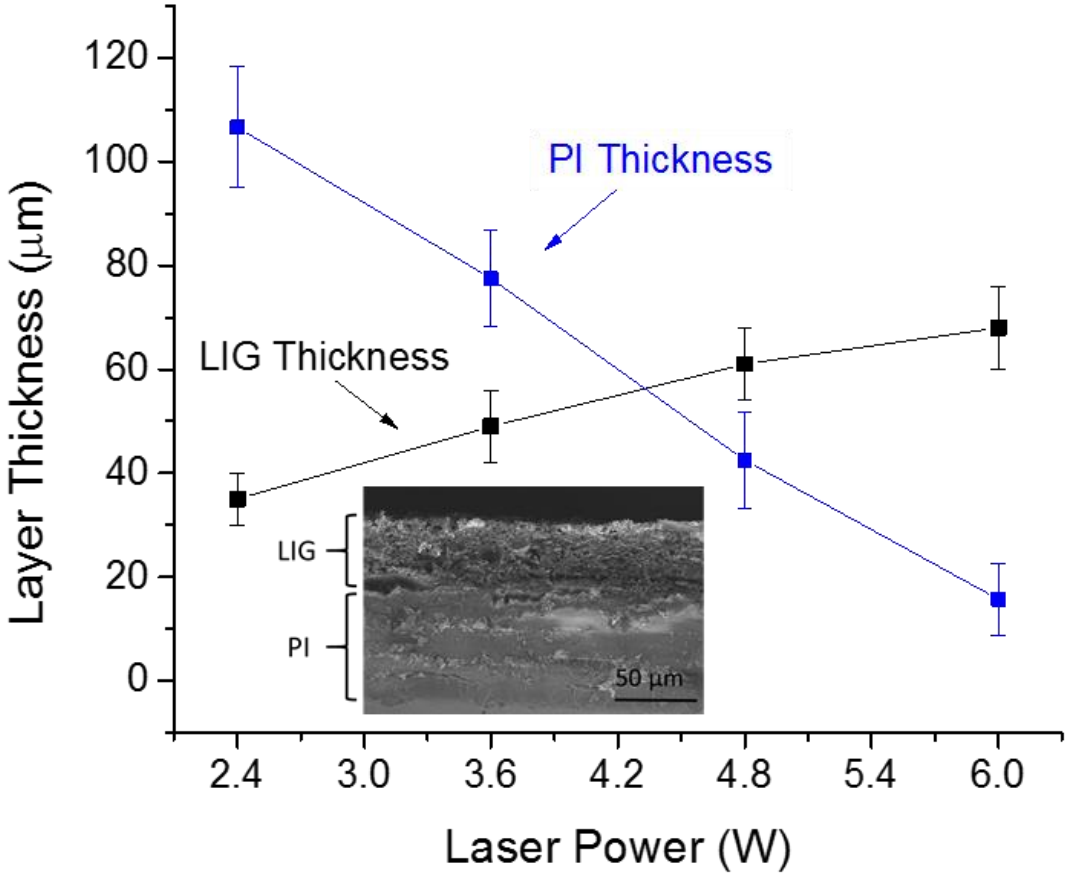

Figure 42. LIG and PI support film thickness as a function of laser power where 2.4, 3.6, 4.8, and 6 watts correspond to a duty cycle of 4, 6, 8, and 10 percent, respectively. Inset SEM image corresponds to the cross-section of the 3.6 W sample.

An illustration demonstrating the sample configuration for the LIG foam PA measurements is included in Figure 43. In addition, representative photoacoustic phase shift and model sensitivity to unknow parameters for the 6% duty cycle LIG are provided in Figure 44and Figure 45, respectively.

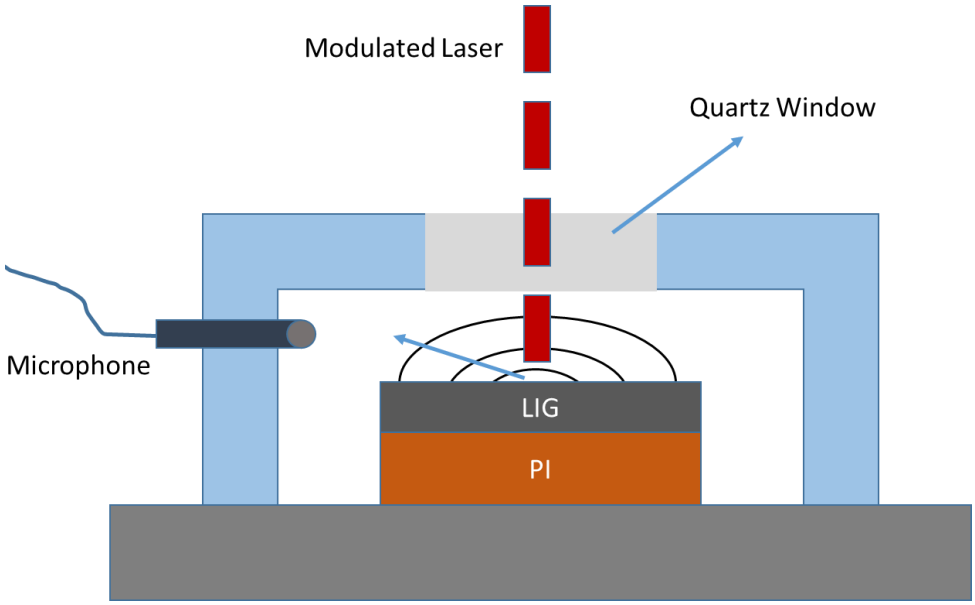

Figure 43. Illustration of the sample configuration and testing unit for the photoacoustic measurements on LIG foams.

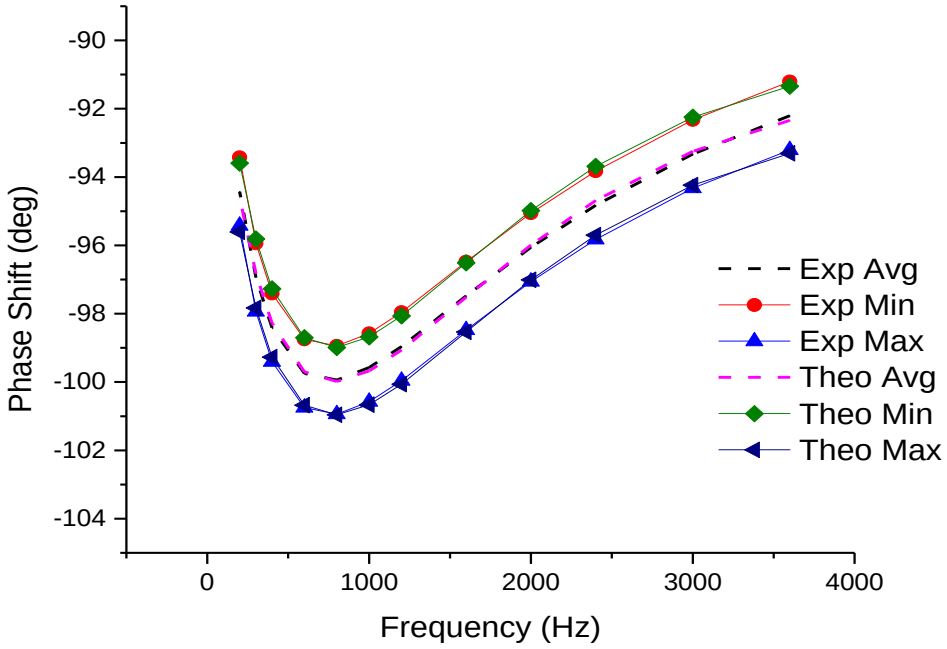

Figure 44. Theoretical and experimental photoacoustic phase shift as a function of laser modulation frequency including ± 1 degree phase shift minimum and maximum fits for uncertainty analysis. These data represent the 6% duty cycle LIG.

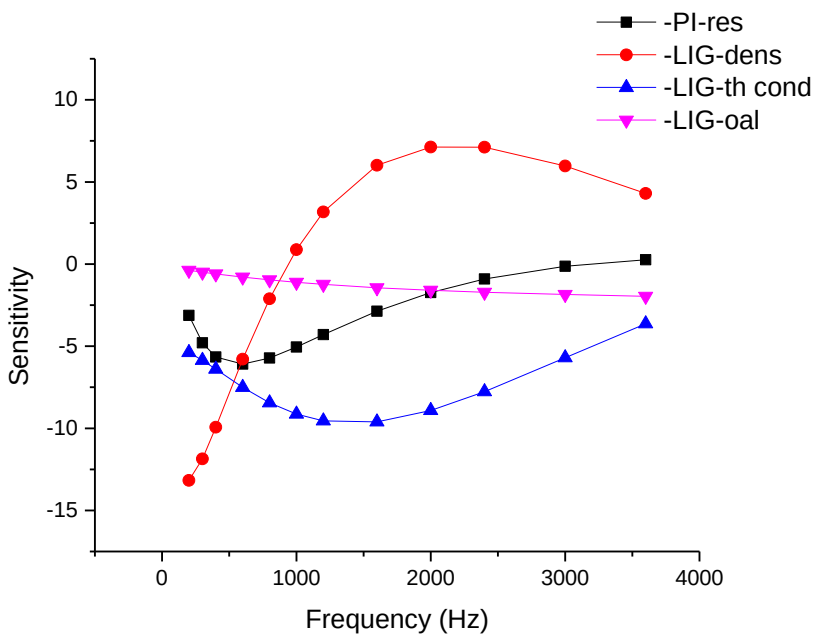

Figure 45. Photoacoustic model sensitivity as a function laser modulation frequency for the four unknown parameters that were fit for. Pi-res is the model sensitivity to the interface thermal resistance between the LIG and PI film, LIG-dens is the sensitivity to the LIG density, LIG-th cond is the sensitivity to the LIG/P3HT thermal conductivity, and LIG-oal is the sensitivity to the LIG/P3HT optical absorbance length. These data represent the 6% duty cycle LIG.

The thermal conductivity does not significantly change as a function of laser irradiation and a peak value of approximately 0.7 W/m-K is observed for foams fabricated at 4% duty cycle, as illustrated in Figure 46. Regardless, the LIG foam thermal conductivity is significantly larger than the PI thermal conductivity of 0.15 W/m-K reported by DuPont. The foam thickness increases gradually from a minimum of approximately 27 µm to a maximum of approximately 50 µm as laser duty cycle increases from 4% to 10%. Scanning electron micrographs of the LIG surface as a function of laser power (Figure 41) demonstrate that the characteristic surface porosity dimensions (the size

of surface voids) is well below the PA laser spot size of 1 mm in diameter (>97% of surface area of 6% sample exhibits pore size <9nm[66]), which is important for determining the applicability of this thermal testing method.

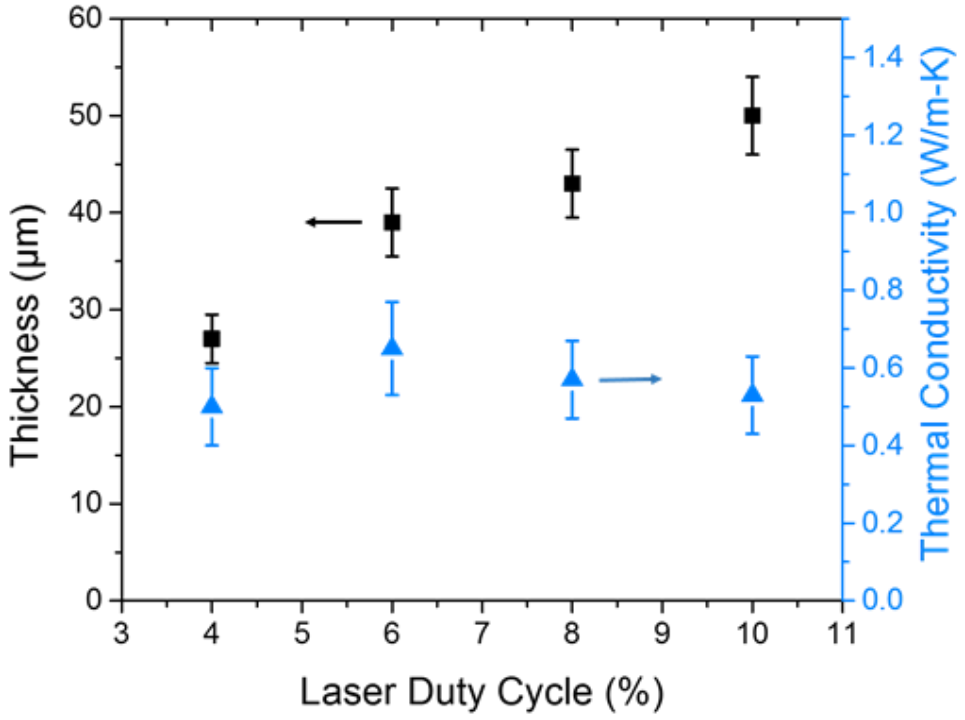

Figure 46. Graphene foam thickness (black squares) and thermal conductivity (blue triangles) as a function of laser power. The thickness error bars represent the standard deviation of three cross-sectional SEM images and the thermal conductivity errors bars represent the combined measurement and fitting uncertainty (see reference[62] and Chapter's 2-4 for more details on the PA method).

Although all thermal measurements fall within the same uncertainty bounds, the trend suggests that maximum foam thermal conductivity is achieved at a laser duty cycle of 6%, most probably due to competing material property modifications that occur as the

laser power is increased. It is expected (and has been confirmed by (Lin, J. *et al.*)) that at low laser power the foam will have the highest density and lowest porosity, but lower relative levels of graphitization; whereas at high laser power (8-10% duty cycle) the opposite is expected (high levels of graphitization, but lower graphene ligament density and high porosity).[66] This expectation is illustrated when comparing points for the 4% and 8% duty cycles Figure 46, where nearly identical thermal conductivity is achieved despite expected variance in density. The results of the PA measurements suggest that the 6% laser power provides an ideal medium where both graphitization and density are relatively high, resulting in peak LIG thermal conductivity. Hence, the 6% LIG is expected to produce the highest thermal conductivity when combined with polymer and was chosen as the base material to fabricate LIG/P3HT composites for thermal testing.

5.3 LIG/P3HT Composite Thermal Characterization

Regioregular P3HT (purchased from Sigma, product number 445703) is stirred into chlorobenzene (using a hot plate set at 60°C and for 1 hour of stirring) to form a 15 mg/mL P3HT solution. An adjustable volume micropipette is used to apply P3HT to the surface of 6% duty cycle GF in 75 μL increments and dried for 2 hours in ambient environment. The resulting P3HT vol% is calculated using the measured volume of the graphene foam and the known amount of P3HT added. The LIG becomes saturated with polymer and a P3HT film begins to develop on the sample surface at the highest P3HT vol% filling, as illustrated in the inset images in Figure 47. However, cross-sectional SEM images reveal the presence of voids that exist even after full sample saturation, resulting in a lower than expected peak P3HT filling of approximately 55 vol% of the total. Hence, the authors

believe the proposed method results in maximum achievable infiltration, as SEM imaging indicates the presence of P3HT films at the top, bottom, and through the entire sample thickness and the addition of more polymer will only result in further surface accumulation. The remaining voids are likely due to sections of the graphene foam that are impenetrable to polymer infiltration due to fully enclosed wall structures or substantially smaller feature sizes. Figure 47 shows that the GF thermal conductivity improves from approximately 0.7 W/m-K at no P3HT filling to an unexpectedly high value of approximately 1.7 W/m-K with maximum achievable infiltration.

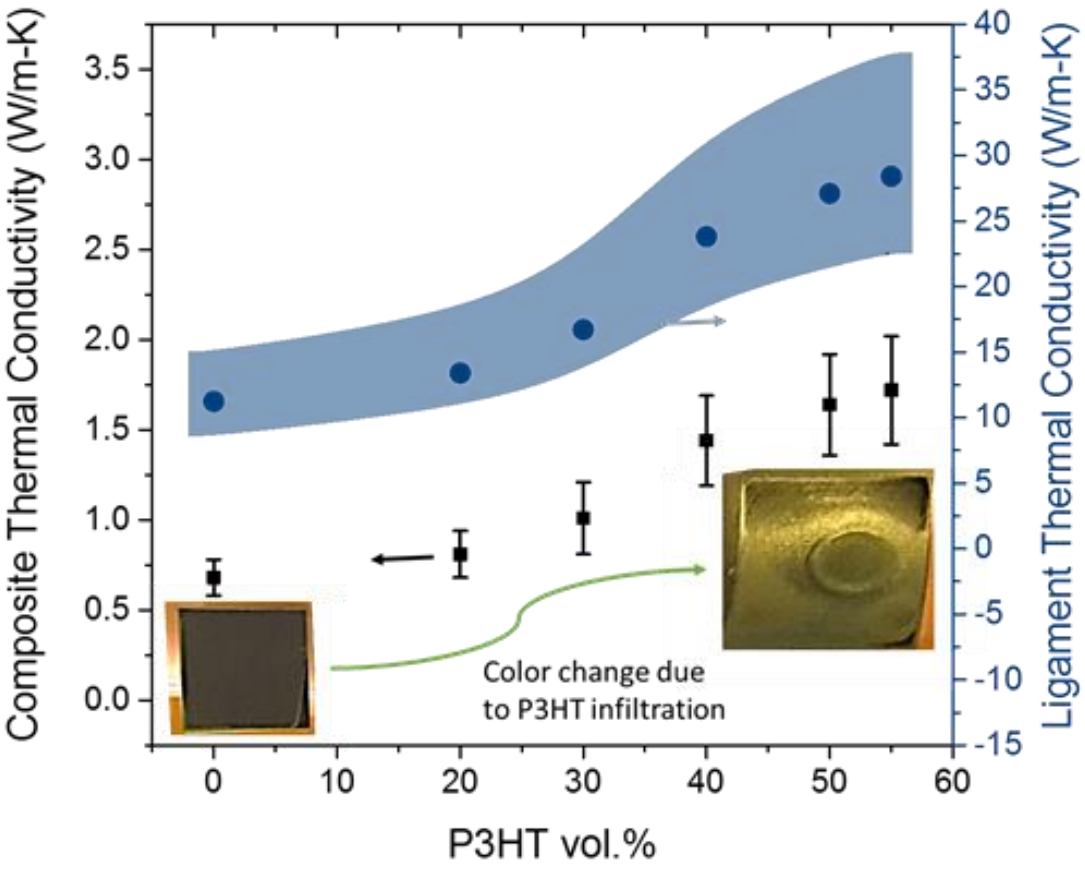

Figure 47. Thermal conductivity of graphene foam/P3HT composite as a function of P3HT vol% is illustrated by the black squares corresponding to the left vertical axis. The errors bars represent the uncertainty associated with the measurement and data fitting uncertainty. The blue shaded region corresponds to the right vertical axis and represents the theoretically calculated ligament thermal conductivity with upper and lower bounds represented by the uncertainty in LIG foam density measurements. The inset images display the LIG surface before and after maximum P3HT infiltration.

The dramatic increase in thermal conductivity is surprising considering the thermal conductivity of P3HT is approximately 0.28 W/m-K (measured by PA on dropcast films) and the thermal conductivity of the helium gas in the PA testing chamber is 0.15 W/m-K.[169] Hence, replacing the helium gas within the GF matrix with P3HT should not result in a significant increase in composite thermal conductivity above the ~ 0.7 W/m-K value

observed at no P3HT infiltration. A high precision scale is used to measure the weight of 1 cm^2 sections of LIG on PI and a scanning electron microscope is used to measure the thickness of each respective layer. These measured values and the manufacturer specified density of PI film (1.42 g/cm^3) are then used to calculate the LIG density. Using the measured 6% duty cycle LIG density and the measured bulk thermal conductivity as a function of polymer filling (λ_{Bulk}), the estimated ligament thermal conductivity (λ_{Solid}) is calculated and plotted in Figure 2 utilizing a simple analytical model to predict the thermal conductivity of connected graphite networks[33] (Equation 9).

$$\lambda_{Bulk} = \alpha \left(\frac{\rho_{Bulk}}{\rho_{Solid}} \right)^{M} \lambda_{Solid} \tag{9}$$

In Equation 9, α (the cellular structure coefficient, equal to 0.734) and *M* (equal to 1.427) are constants to account for the impact of both the pore shape and the volume ratio of ligaments to junctions on the path length of heat flow in GF, respectively. These constants were derived for CVD grown graphitic foam networks and may not exactly correlate to our material system; however, because our material has a relatively high density and low bulk thermal conductivity, simpler models (Equations 1 and 2 in reference[33]) with constants that are universally applied to all foam systems produce results within the uncertainty bounds associated with our density measurements. The bulk density (GF density) and the solid density (graphene ligament density) are both denoted by ρ where the bulk is measured to be 385 ± 70 mg/cm^3 and the ligament value (the backbone density,

not the foam density) is taken from literature as 2.2 g/cm^3.[33] The blue shaded region represents the upper and lower bounds of the estimated ligament conductivity as a function of GF density, where the bounds are determined by the uncertainty in the density measurements.

5.4 LIG/P3HT Theoretical Analysis and Results Discussion

The relatively low values of GF ligament thermal conductivity are likely due to the polycrystalline nature of the LIG foams and poor structural integrity (fractured ligaments), which will both contribute to enhanced interfacial phonon scattering and contact resistance. The dramatic increase in thermal conductivity with addition of P3HT is likely due to a significant enhancement of the graphene foam ligament network thermal conductivity, where effective ligament thermal conductivity increases from approximately 12 W/m-K to 28 W/m-K. We hypothesize that the addition of polymer solution results in capillary driven healing of broken ligament networks through elastocapillary coalescence[81, 97] allowing for an increase in the total number of thermal transport pathways and better adhesion between contact points of pathways in physical contact. Electrocapillary coalescence occurs when solvent induced capillary forces overcome LIG network elastic forces and draw LIG ligaments into contact (or coalescence) and then the surfaces remain in contact after removal of solvent due to adhesion or polymer binding forces. Multiple wetting events were recorded with solvent only and the resulting GF thermal conductivity did not change significantly, which suggest the polymer is essential due to its strong interaction with the graphene and is ability to serve as a binding material upon solvent evaporation.

The theoretically calculated ligament thermal conductivity values (λ_{Solid}), as well as the polymer thermal conductivity ($\lambda_{Polymer}$), are used in a normalized unit cube model developed by Yu et al.[170] (Equation 10) to calculate the bulk composite thermal conductivity (λ_{Bulk}).

$$\lambda_{Bulk} = (1 - 2n + 2n^2)\left(\frac{(1/n - 1)^2 + \sigma}{(1/n - 1)^2 + 1}\right)\lambda_{Polymer} + \frac{2n(1-n)}{(1-n)\sigma + n}\lambda_{Solid} \quad (10)$$

where σ is the ratio of solid ligament thermal conductivity to the polymer thermal conductivity (or fluid thermal conductivity (helium gas) is the case of no polymer infiltration) and n = 2c/H where c and H are the structural parameters determined by the foam porosity and pore diameter (further details are included in the original LIG fabrication publication's (Lin, J. *et al.*) supplemental material[66]). The theoretically calculated composite thermal conductivities are illustrated by the green shaded region in Figure 48 and the measured LIG/P3HT composite thermal conductivities are indicated by the black squares and are plotted again (these are the same values from Figure 47) for comparison.

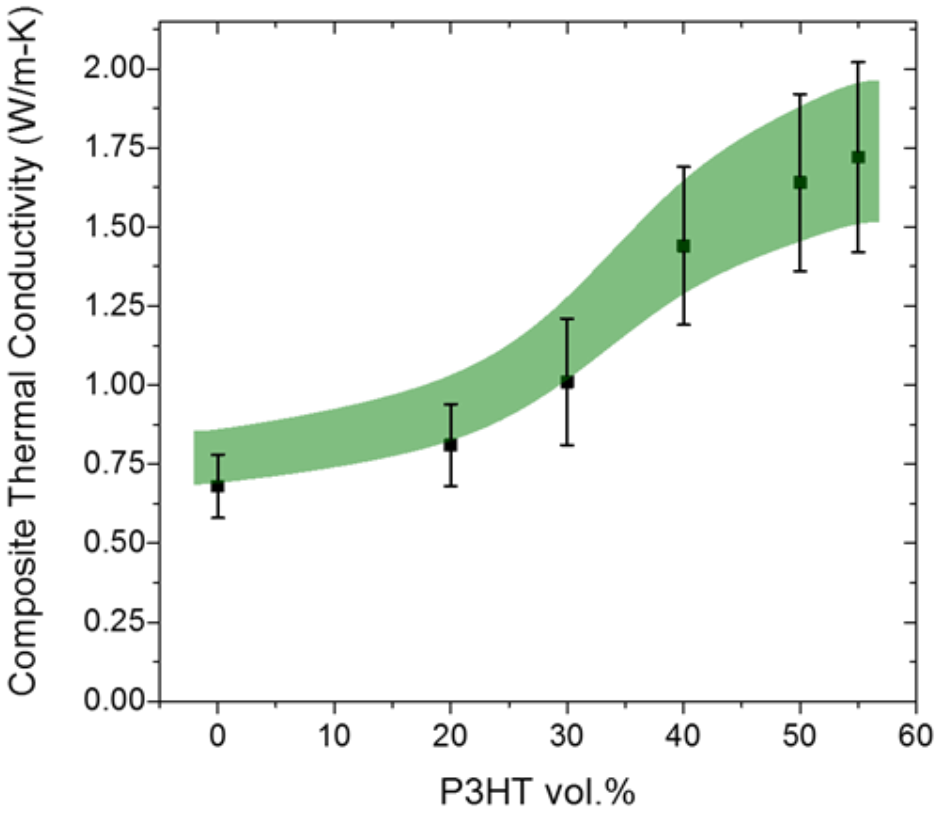

Figure 48. Experimental (black squares) and theoretical (green shaded region) LIG thermal conductivity as a function of P3HT filling vol%. The errors bars represent the combine measurement and fitting uncertainty associated with the PA method and the bounds on the shaded region are determine by the uncertainty in the LIG density measurements.

In general, good agreement is observed between the theoretically predicted values (calculated using the estimated LIG ligament thermal conductivities) and experimental photoacoustic measured values. However, at low filling volumes the model over-predicts the measured thermal conductivity whereas at the higher filling volumes the best agreement between theoretical and measured values is achieved. Less consistent agreement between the experimental and model results at low conductivities likely arises because the theoretically models where originally derived for foams with high ligament thermal

conductivity (>500 W/m-K). Regardless, these results support the previous finding that the effective ligament network thermal conductivity is improved at high P3HT vol% filling, resulting in improved composite thermal conductivity. Similar results were recently reported for graphene foam thermal conductivity as a function of temperature, where it was found that the GF thermal conductivity significantly increased with temperature due to a thermal expansion induced "tightening" of the foam network, which reduced contact resistance between ligaments.[171] Here we argue that elastocapillary coalescence during solution drying draws LIG ligaments into contact and the P3HT acts as a binding material to secure these contacts after full solvent evaporation, which results in a reduction in the effective skeletal thermal resistance, or an increase in the effective thermal conductivity.

Three-dimensional graphene foam fabricated through CVD methods on sacrificial nickel support have demonstrated ligament thermal conductivity as high as 995 W/m-K and foam conductivity of 1.70 W/m-K at very low vol% of 0.45 (or more than an order of magnitude lower density (11.6 mg/cm^3) as compared to LIG).[172] Although CVD methods are expected to be more costly, they demonstrate the high potential for graphene foams in thermal conduction applications and the potential room for improvement in cheaper LIG foams, assuming LIG quality can be improved. In another study, graphene nanoplatelets with high quality and low defect density (manufacturer specified thermal conductivity of 3000 W/m-K) were mixed into polymer matrix under high compression, resulting in composites with record high 12.4 W/m-K thermal conductivity at 25 vol%.[173] The observed 12.4 W/m-K value is impressive, but it is clear that the CVD graphene foam sample would achieve higher conductivity at an equivalent vol%, likely due to high thermal contact resistances in the randomly dispersed system. Hence, the LIG fabrication offers

the potential to fabricate graphene foam with high vol% and may also avoid the interfacial contact resistance problem associated with randomly dispersed systems.

5.5 Conclusions

The results presented here demonstrate a simple method to drastically improve thermal transport in LIG foam composites. Moreover, the remarkable thermal conductivity enhancement from approximately 0.7 W/m-K to greater than 1.7 W/m-K suggests this process could be interesting for commercial thermal interface applications, as well as electrical applications not discussed in this report. If the LIG manufacturing process can be optimized to attain higher quality graphene ligaments, the effective thermal conductivity of LIG/polymer composites may achieve significantly enhanced thermal conductivities to the point of viability in certain commercial thermal applications.

CHAPTER 6. 1D REFERENCE BAR MEASURMENTS OF NANOSTRUCTURED TIMS AND LEADING INDUSTRY MATERIALS

6.1 Introduction to the 1D Reference Bar

The 1D reference bar method (ASTM D5470) is the industry standard for measuring and benchmarking thermal interface materials. The primary advantages of this method in comparison to the photoacoustic and laser flash methods in that the TIM material can be tested under application specific compression forces and the contact resistance is accounted for, resulting in an effective thermal conductivity similar to what would be expected in application.[174] The reference bar method can also be used to test a materials long-term performance under cyclic loading. In this Chapter, we investigate the thermal performance of double-sided melt-processed P3HT nanofiber films (describe in Chapter 3) using a modified 1D reference bar testing method described previously.[26, 175] In addition, we benchmark several high performing commercial thermal interface materials in the categories of phase change materials (PCMs), pads, and metal TIMs.

In short, a TIM material is placed between two thermally conductive bars (typically steel or aluminum) and a controlled power source maintains the upper reference bar (URB) at a set high temperature and a cooling bath is used to keep the lower reference bar (LRB) at a set low temperature. Thermocouples are place along the length of the bars at a known spacing and a least squares regression is used to determine the heat flux (Q) and reference

bar surface temperatures. The change in bar temperature as a function of distance (*dT/dz*), the bar cross-section area (*A*), and the bar thermal conductivity (*K*) are used to calculate *Q* in Equation 11.

$$Q = -KA\left(\frac{dT}{dz}\right) \tag{11}$$

The calculated heat flux, the measured temperature drop across the TIM interface, and the TIM cross-sectional area are then used to determine thermal resistance in units of mm^2-K/W. The image in Figure 49 illustrated the custom 1D reference bar measurement system located in the Georgia Tech Heat Lab. This system has been modified to include a top bar with a larger surface area to prevent errors associated with top and bottom bar alignment mismatch, and a second order curve fitting method is employed to account for heat constriction at the interface.[175]

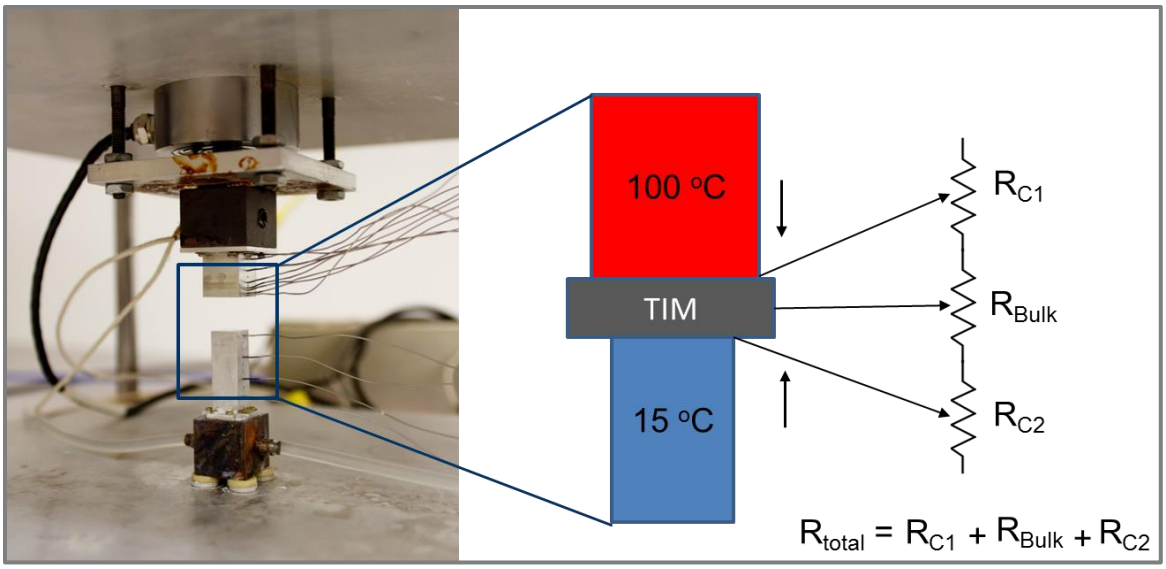

Figure 49. Image of the custom 1D reference bar measurement system located in the Georgia Tech Heat lab. A diagram for the equivalent thermal circuit for TIM measurement is also included.

6.2 Summary of Commercial TIMs Tested

Figure 50 below illustrates SEM cross-sectional images for two industry leading materials, Fujipoly Sacron XR-m filler pad and the Polymatech Japan Co.,Ltd Manion50 pad (both materials are re-sold under various trade names). The XR-m pad is rated at 17 W/m-K (advertised resistance of ~40 mm^2-K/W at 40 psi), is electrically insulating and is filled with a high weight percent of alumina and other unknown filler particles, within a silicone polymer matrix. The Manion50 product boasts an extremely high thermal conductivity of 50 W/m-K (advertised resistance of 48 mm^2-K/W at 30 psi) and uses proprietary technology to achieve vertical alignment of high conductivity carbon fibers, embedded in a silicone matrix that appears to be filled with a secondary conductive filler.[18] These materials are representative of the highest performing TIMs in both the electrically

insulating and conducting pad applications. In this work their thermal resistance as a function of thickness and applied pressure was determined using the reference bar method.

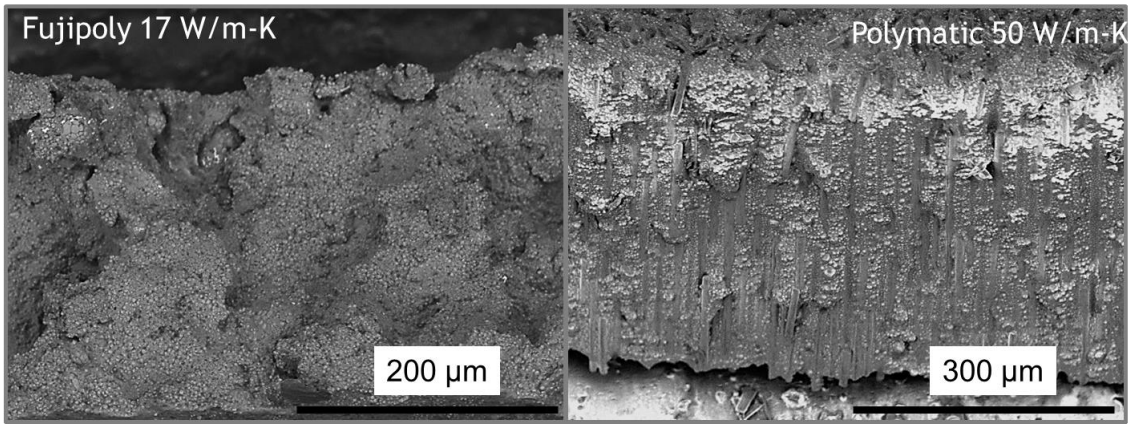

Figure 50. SEM cross-sectional images of high performance commercial thermal interface materials.

Additionally, the thermal resistance of high performance Indium metal foil Heat-Spring materials with thicknesses of 170 µm and 70 µm (advertised resistance below 10 mm^2-K/W at 40 psi), Graftech HT-2505 graphite pads with thickness of 125 µm (advertised resistance of ~40 mm^2-K/W at 30 psi), and Laird TCPM 580 series phase change material with a thickness of 127 µm (advertised resistance below 10 mm^2-K/W at 50 psi) were measured to fully evaluate the performance of several commercial TIM options. As will be discussed, the commercial materials performance was often significantly reduced in comparison to the advertised specifications.

6.3 1D Reference Bar Results and Discussion

Figure 51 includes the thermal resistance as a function of material thickness and applied pressure for the Fujipoly and Polymatic materials. For comparison, a lower performance Fujipolymer material rated at 13 W/m-K and 500 µm in thickness is included.

At similar thickness of 500 µm, the Polymatic material shows enhanced performance across all pressure ranges. It is worth noting even under the unlikely assumption of zero compression, the higher performing Polymatic material is only able to achieve an effective thermal conductivity of ~ 10 W/m-K. This surprising result (manufacture specified 50 W/m-K) is likely due to high contact resistance associated with the vertically aligned carbon fiber structure and the advertise thermal resistance at 30 psi (48 mm^2-K/W) is in good agreement with the measured value of 57 mm^2-K/W. For all the materials tested, the thermal resistance becomes less sensitive to applied pressure as the sample thickness decreases, which is likely due to a reduction in compression.

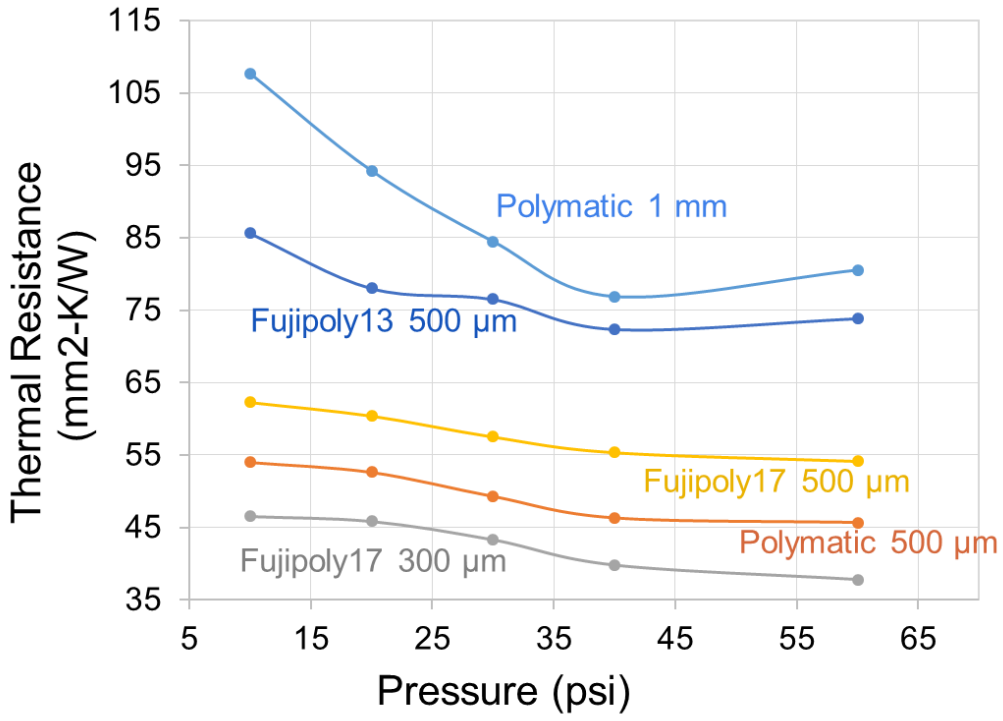

Figure 51. Thermal resistance as a function of pressure for high performance Polymatic and Fujipoly TIMs.

Figure 52 includes the plot of the thermal resistance as a function of pressure for two additional materials, Indium metal foil and Graftech graphite pad (the results for the thin Polymatic and Fujipoly materials are included for comparison). The Graftech pad exhibits a linear decrease in resistance with applied pressure and its thermal resistance at 30 psi (52 mm^2-K/W) is significantly higher (~20%) than the advertised value of 40 mm^2-K/W. The indium foil demonstrates exceptional performance above 20 psi, but still does not reach its advertised thermal performance rating of less than 20 mm^2-K/W even at the highest pressures.

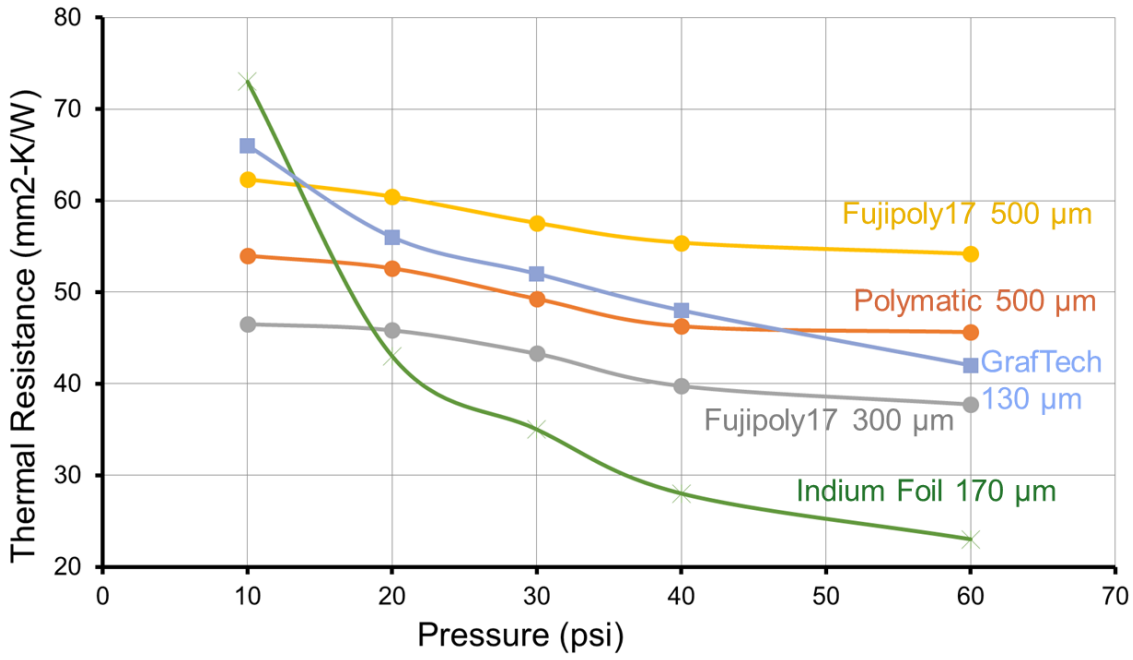

Figure 52. Thermal resistance as a function of pressure for thin Polymathic and Fujipoly samples as well as Graftech graphite TIMs and Indium metal TIMs.

Lastly, the thermal resistance as a function of pressure for a second Indium foil sample of 70 µm in thickness and the Laird PCM material are measured and the results are included below in Figure 53. Interestingly, the resistance of the 170 µm and 70 µm Indium samples is the same, indicating that their measured thermal resistance is dominated by

contact resistances. The Laird PCM demonstrates the highest performance and is able to reach thermal resistances approaching 10 mm^2-K/W at pressures as low as 20 psi.

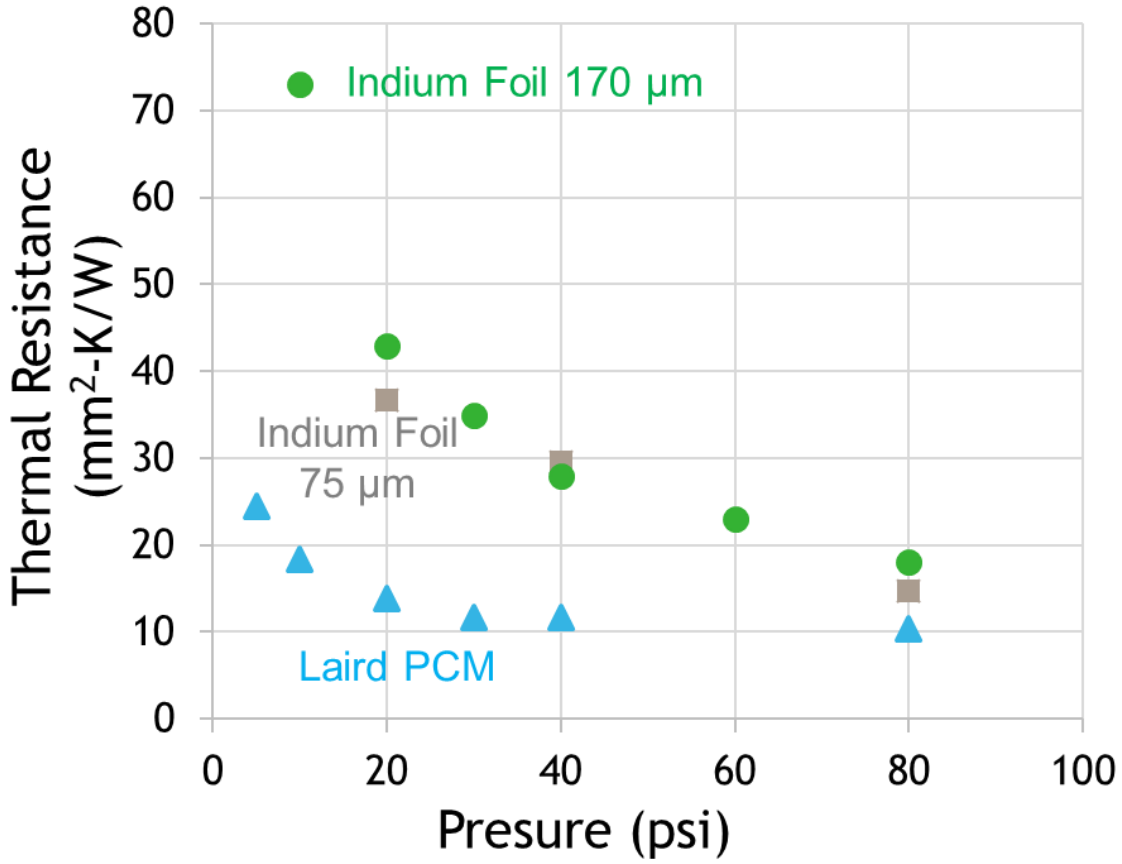

Figure 53. Thermal resistance as a function of pressure for two types of Indium foil and for a Laird phase change materials TIM with approximate bond line thickness of 50-100 µm.

The thermal resistance as a function of pressure for a double sided P3HT nanofiber array fabricated using techniques described in Chapter 3 is plotted in Figure 54. For this sample, the material stack was comprised of ~25 µm of nanofiber forest on both sides of a 75 µm thick P3HT film (characterized using SEM imaging in Section 3.2). With a known P3HT film thermal conductivity of ~0.2 W/m-K, the estimated film resistance is equal to 350 mm^2-K/W. The red open circle triangles represent the fiber film thermal resistance,

which is equal to ~ 50 mm^2-K/W at 100 psi. Assuming, insignificant compression of the nanofibers, the total fiber thickness is ~50 μm and the effective thermal conductivity is ~ 1 W/m-K. Assuming a ~50% fill fraction and no contact resistance, this equates to a thermal conductivity of ~ 2 W/m-K for individual polymer nanofibers. These results agree well with the measured thermal conductivity of 200 nm diameter P3HT nanofiber arrays in Chapter 2.

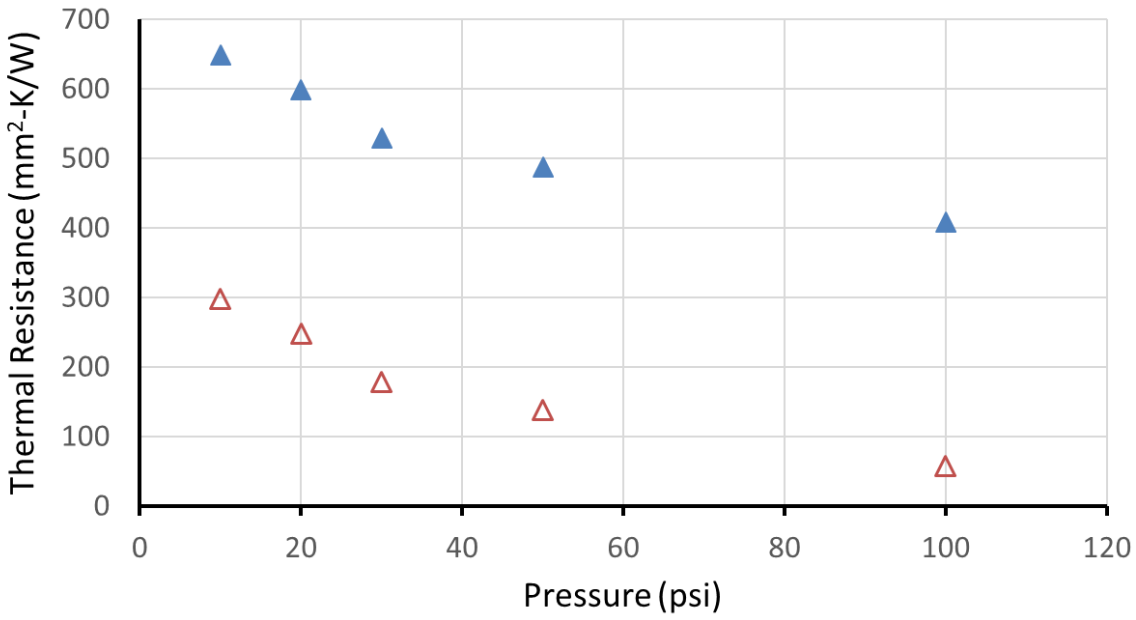

Figure 54. Thermal resistance as a function of pressure for double sided P3HT nanofiber arrays with middle P3HT film thickness of approximately 75 μm and fiber forest thickness of approximately 25 μm on each side. The closed blue triangle is the total TIM resistance and the open red triangles are the calculated fiber array resistance after subtracting the estimated film resistance of 350 mm^2-K/W.

However, it is clear from Figure 55 that the surface of the nanofiber array does compress significantly and that the effective thermal conductivity is likely less than 1 W/m-K and that thermal contact resistances can be significant for vertically aligned polymer fiber structures, further validating similar observations from Chapter 2. Regardless, it is

promising that the nanofiber array could maintain improved performance up to 80 psi and future work will focus of reducing the middle P3HT film thickness.

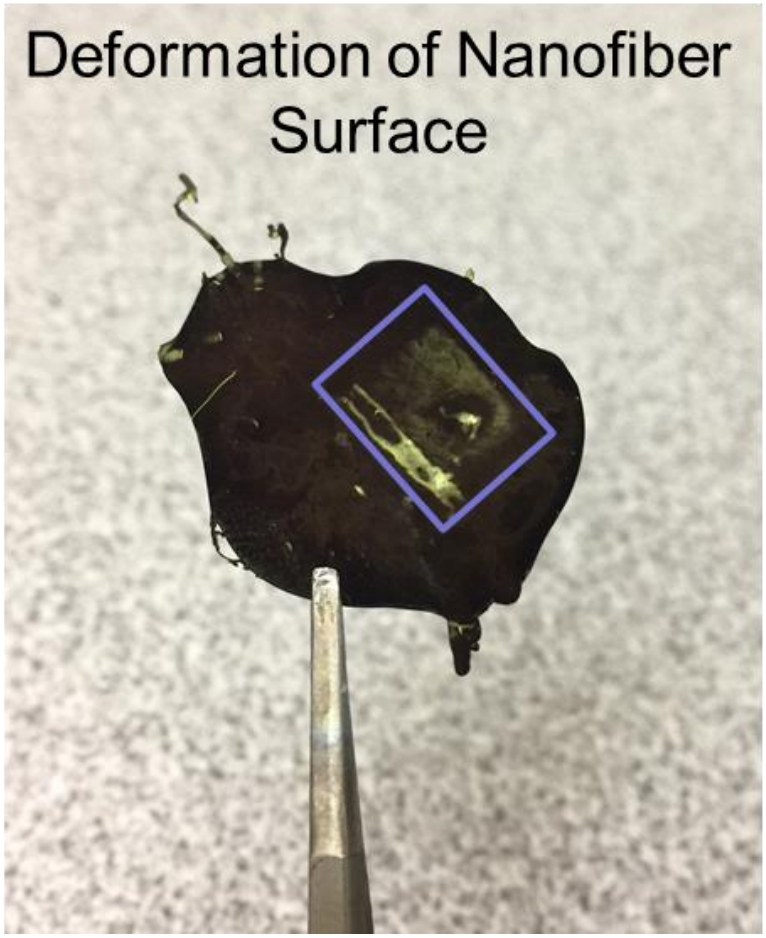

Figure 55. Visual indication of surface compression for vertically aligned arrays of 200 nm P3HT nanofibers after reference bar measurements up to 80 psi. This sample was only tested under compression to determine surface restructuring as a function of force. The sample that was measured for thermal testing was cut to fit the bar dimension of 1 cm^2.

6.4 Conclusions

This chapter reports on the thermal resistance as a function of pressure for several industry leading thermal interface materials. These materials demonstrate extremely high effective thermal conductivities (peaking around 10 W/m-K) and thermal resistances that are typically 10-20 % larger than advertised. In addition, a double sided P3HT nanofiber array was measured to determine the sample performance as a function of pressure. It was determined that the nanofiber array had an effective thermal conductivity of ~ 1 W/m-K and was able to maintain improved performance up to 80 psi.

CHAPTER 7. CONCLUSIONS AND RECCOMENDATIONS

7.1 Summary of Key Findings

7.1.1 Chapter 2

In Chapter 2 we exploit the clustering of regioregular poly(3-hexylthiophene) (rr-P3HT) nanotubes in a unique template etching process to create surfaces that exhibit tunable wetting and contact thermal energy transport. Vertical arrays of rr-P3HT nanotubes are cast from solution in nanoscale alumina templates, and a solution etching process is used to partially release the nanotubes from the template. The clustering of rr-P3HT nanotube tips upon template etching produces hierarchical surface structuring with a distinct pattern of interconnected ridges, and the spacing between the ridges increases with increased template etch times. These changes in morphology cause the water contact angle to increase from 141° to 168° as the etch time is increased from 4 to 12 minutes. When assembled into an interface, the morphological changes cause the thermal contact resistance of the vertical rr-P3HT nanotube arrays to increase linearly at a rate of approximately 6 mm^2K/W per 2 minute etch interval (after 6 minutes of etching is surpassed). The effective thermal conductivity of the rr-P3HT nanotube arrays is 1 ± 0.2 W/m-K independent of the etch time, which is approximately 5 times higher than the bulk rr-P3HT film value. A summary of the important findings is included in Figure 56.

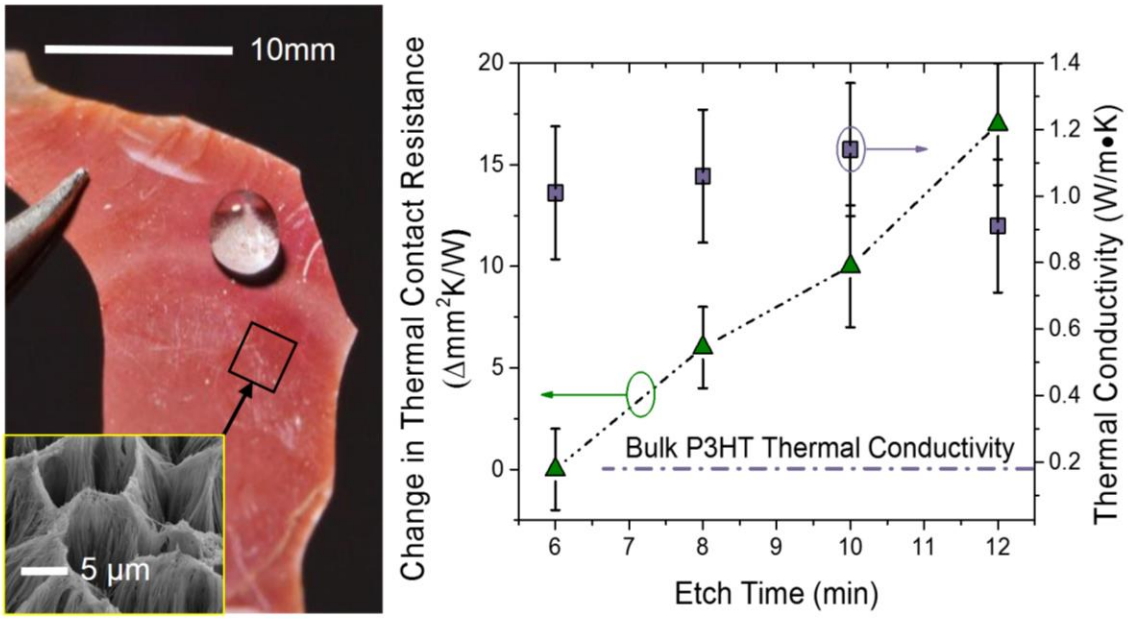

Figure 56. Chapter 2 summary image of water droplet on hydrophobic P3HT nanotube surface with inset SEM image illustrating nanotube clustering. The plot on the right illustrates thermal contact resistance and thermal conductivity as a function of nanotube surface morphology.

7.1.2 Chapter 3

In Chapter 3 we impregnate nanoporous anodic aluminum oxide (AAO) templates with molten polymer to fabricate large area arrays of vertically aligned polymer nanofibers. Nanoscale confinement effects and flow induced chain elongation improve polymer chain alignment (measured using polarized Raman spectroscopy) and thermal conductivity (measured using the photoacoustic method) along the fiber's long axis. Conjugated poly(3-hexylthiophene-2,5-diyl) (P3HT) and non-conjugated polyethylene (PE) of various molecular weights are explored to establish a relationship between polymer structure, nanofiber diameter, and the resulting thermal conductivity. In general, thermal conductivity improves with decreasing fiber diameter and increasing polymer molecular

weight. Thermal conductivity of approximately 7 W/m-K was achieved for both the ~200 nm diameter HDPE fibers and the 100 nm diameter P3HT fibers. These results pave the way for optimization of the processing conditions to produce high thermal conductivity fiber arrays using different polymers, which could potentially be used in thermal interface applications.

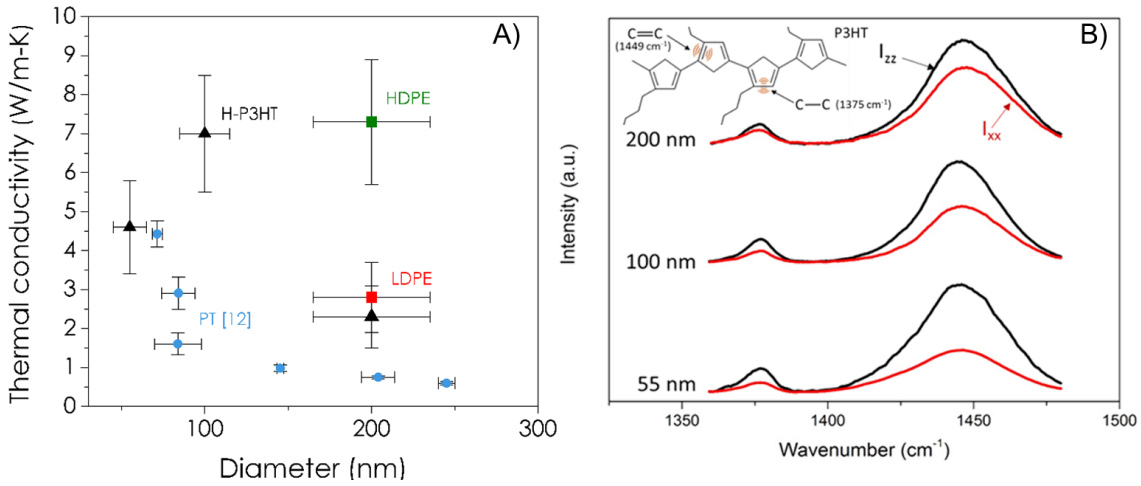

Figure 57. Chapter 3 summary slide illustrating A) Nanofiber thermal conductivity as a function of fiber diameter and polymer. B) Polarized Raman measurements of 55, 100, and 200 nm diameter P3HT nanofibers with intensities in the ZZ and XX directions shown. Inset image illustrates the P3HT backbone bonds associated with the Raman peaks.

7.1.3 Chapter 4

In Chapter 4 nanoporous alumina membranes are filled with multi-walled carbon nanotubes (MWCNTs) and then poly(3-hexylthiophene-2,5-diyl) (P3HT) melt, resulting in nanofibers with nanoconfinement induced co-alignment of both MWCNT and polymer chains. The simple sonication process proposed here can achieve vertically aligned arrays of P3HT/MWCNT composite nanofibers with 3 wt% to 55 wt% MWCNT content, measured using thermogravimetric methods. Electrical and thermal transport in the

composite nanofibers improves drastically with increasing carbon nanotube content where nanofiber thermal conductivity peaks at 4.7 ± 1.1 $Wm^{-1}K^{-1}$ for 24 wt% MWCNT and electrical percolation occurs once 20 wt% MWCNT content is surpassed. This is the first report of the thermal conductivity of template fabricated composite nanofibers and the first proposed processing technique to enable template fabrication of composite nanofibers with high filler content and long aspect ratio fillers, where enhanced properties can also be realized on the macroscale due to vertical alignment of the nanofibers. These materials are interesting for thermal management applications due to their high thermal conductivity and temperature stability. Summary Figure 58 includes SEM and optical images of the fabricated materials, as well as the resultant thermal and electrical properties as a function of MWCNT wt%.

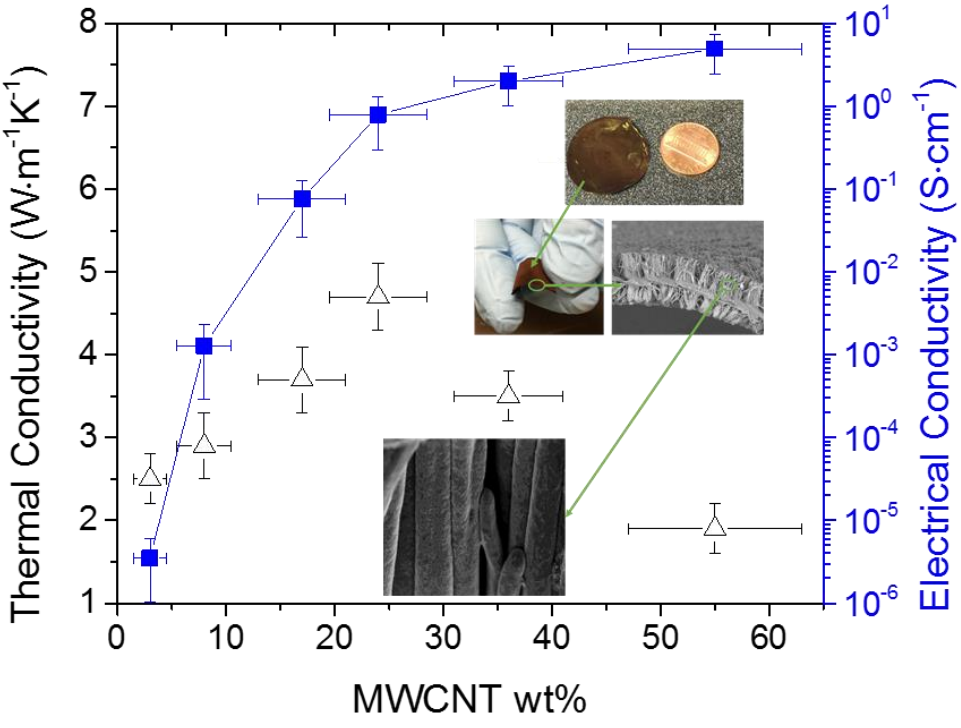

Figure 58. Chapter 4 summary slide illustrating thermal and electrical conductivity as a function of MCNT wt% in template fabricated P3HT/MWCNT nanofibers. Inset image illustrates SEM and optical images of the fabricated materials.

7.1.4 Chapter 5

In Chapter 5, laser induced graphene (LIG) foams, fabricated through a simple and cost effective laser ablation method, are infiltrated with poly(3-hexylthiophene) (P3HT) in a step-wise fashion to demonstrate the impact of polymer on the thermal conductivity of the composite system. Surprisingly, the addition of polymer results in a drastic (250%) improvement in material thermal conductivity, enhancing the graphene foam's thermal conductivity from 0.68 W/m-K to 1.72 W/m-K for the fully infiltrated composite material. Graphene foam density measurements and theoretical models are utilized to estimate the effective ribbon thermal conductivity as a function of polymer filling. Here it is proposed that the polymer solution acts as binding material which draws graphene ligaments together through elastocapillary coalescence and bonds these ligaments upon drying, resulting in greatly reduced contact resistance within the foam and an effective thermal conductivity improvement greater than what would be expected from the addition of polymer alone. These materials demonstrated promising thermal conductance and may pave the way for future low-cost foam based thermal interface materials.

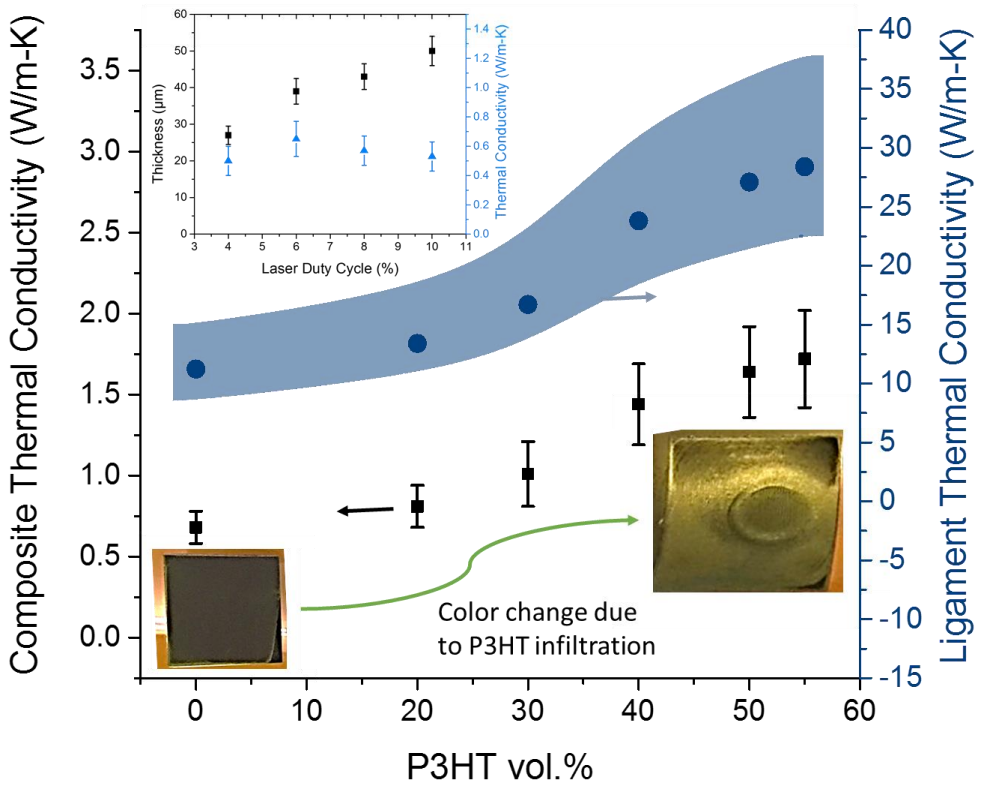

Figure 59. Chapter 5 summary slide illustrating LIG thermal conductivity and thickness as a function of laser duty cycle (inset figure) and LIG/P3HT composite thermal conductivity as a function of P3HT vol.%. Inset images demonstrate the change in LIG color upon P3HT infiltration and the blue shaded region corresponds to the theoretically calculated LIG ligament thermal conductivity.

7.1.5 Chapter 6

Chapter 6 introduces the 1D reference bar technique for industry standard thermal resistance measurements of thermal interface materials. Several high performance TIMs are benchmarked, including Indium Heat Spring foils, Laird phase change materials, Graftech graphite films, and Fujipoly and Polymatech pads. Overall, their thermal resistances are like manufacture specifications, but typically measure med 5-20% higher resistance than advertised. In addition, a doubled sided P3HT nanofiber array was

measured to determine applicability as a thermal interface material. The nanofiber TIM measured a very high resistance of over 400 mm^2-K/W even at moderate pressures. This high resistance was due to the presence of a low thermal conductivity inner film layer of ~75 μm bulk P3HT and the effective TIM thermal conductivity was improved to 1 W/m-K when the resistance due to bulk P3HT film was removed.

7.2 Recommendations for Future Work

A large portion of this work focused on examining the difference in resulting structure and properties of P3HT nanofibers as a function of processing conditions, molecular weight, and fiber diameter. Considering recent developments, it would be interesting to perform a follow-up study to determine the impact of thermal annealing on the resultant thermal properties of template fabricated nanofibers. It is likely that thermal annealing will result in significant structural and thermal property changes, as has been recently reported for similar sized polyethylene nanofibers.[176] However, it would be interesting to investigate the role of the hard template in suppressing structural changes during annealing in-template.

A second focus of this work was on the development of the first template fabricated polymer based composite nanofibers with high filler concentration. For both the composite system and for the pure polymer systems, the relatively low template porosity (~50%) will always limit the fiber number density to less than 50% fill fraction. Hence, higher porosity templates should be used to fabricate double sided nanofiber areas and the middle film

thickness needs to be minimized. The double-sided samples of both pure polymer or various diameters and MWCNT fiber composites could then be tested in the 1D reference bar. These developments would pave the way for materials with much lower thermal resistance in application and could be commercially attractive for use as TIM

The unexpected increase in thermal conductivity of the LIG foam upon P3HT infiltration is still not fully understood and further structural analysis could help to determine the ability of the P3HT solution to repair broken ligament connections. In addition, polymer solutions of non-conjugated polymers could be applied in a similar manner to determine the impact of π-π bonding, or lack thereof, on the thermal transport. Finally, the LIG processing steps could be further optimized to further improve the crystal domain sizes in the graphene ligaments, which should drastically increase ligament thermal conductance.

REFERENCES

1. Sahin, O.; Coskun, A. K. On the Impacts of Greedy Thermal Management in Mobile Devices. *On the Impacts of Greedy Thermal Management in Mobile Devices* **2015,** *7*, 55-58.

2. Chung, D. Thermal Interface Materials. *Thermal Interface Materials* **2001,** *10*, 56-59.

3. Kadoya, K.; Matsunaga, N.; Nagashima, A. Viscosity and Thermal Conductivity of Dry Air in the Gaseous Phase. *Viscosity and Thermal Conductivity of Dry Air in the Gaseous Phase* **1985,** *14*, 947-970.

4. Narumanchi, S.; Mihalic, M.; Kelly, K.; Eesley, G. In *Thermal Interface Materials for Power Electronics Applications*, Thermal and Thermomechanical Phenomena in Electronic Systems, 2008. ITHERM 2008. 11th Intersociety Conference on, IEEE: 2008; pp 395-404.

5. Lin, W.; Moon, K.-S.; Wong, C. P. A Combined Process of in Situ Functionalization and Microwave Treatment to Achieve Ultrasmall Thermal Expansion of Aligned Carbon Nanotube–Polymer Nanocomposites: Toward Applications as Thermal Interface Materials. *A Combined Process of in Situ Functionalization and Microwave Treatment to Achieve Ultrasmall Thermal Expansion of Aligned Carbon Nanotube–Polymer Nanocomposites: Toward Applications as Thermal Interface Materials* **2009,** *21*, 2421-2424.

6. Guo, Y.; Lim, C. K.; Chen, W. T.; Woychik, C. G. Solder Ball Connect (Sbc) Assemblies under Thermal Loading: I. Deformation Measurement Via Moiré Interferometry, and Its Interpretation. *Solder Ball Connect (Sbc) Assemblies under Thermal Loading: I. Deformation Measurement Via Moiré Interferometry, and Its Interpretation* **1993,** *37*, 635-648.

7. Prasher, R. Thermal Interface Materials: Historical Perspective, Status, and Future Directions. *Thermal Interface Materials: Historical Perspective, Status, and Future Directions* **2006,** *94*, 1571-1586.

8. Choy, C. Thermal Conductivity of Polymers. *Thermal Conductivity of Polymers* **1977,** *18*, 984-1004.

9. Prasher, R. S.; Shipley, J.; Prstic, S.; Koning, P.; Wang, J.-L. Thermal Resistance of Particle Laden Polymeric Thermal Interface Materials. *Thermal Resistance of Particle Laden Polymeric Thermal Interface Materials* **2003,** 431-439.

10. Sarvar, F.; Whalley, D. C.; Conway, P. P. In *Thermal Interface Materials - a Review of the State of the Art*, 2006 1st Electronic Systemintegration Technology Conference, 5-7 Sept. 2006; 2006; pp 1292-1302.

11. Tzeng, J. J. W.; Weber, T. W.; Krassowski, D. W. In *Technical Review on Thermal Conductivity Measurement Techniques for Thin Thermal Interfaces*, Sixteenth Annual IEEE Semiconductor Thermal Measurement and Management Symposium (Cat. No.00CH37068), 2000; 2000; pp 174-181.

12. Prasher, R.; Chiu, C.-P., Thermal Interface Materials. In *Materials for Advanced Packaging*, Lu, D.; Wong, C. P., Eds. Springer International Publishing: Cham, 2017; pp 511-535.

13. Shahil, K. M. F.; Balandin, A. A. Graphene–Multilayer Graphene Nanocomposites as Highly Efficient Thermal Interface Materials. *Graphene–Multilayer Graphene Nanocomposites as Highly Efficient Thermal Interface Materials* **2012,** *12*, 861-867.

14. Yu, H.; Li, L.; Kido, T.; Xi, G.; Xu, G.; Guo, F. Thermal and Insulating Properties of Epoxy/Aluminum Nitride Composites Used for Thermal Interface Material. *Thermal and Insulating Properties of Epoxy/Aluminum Nitride Composites Used for Thermal Interface Material* **2012,** *124*, 669-677.

15. Zhu, D.; Yu, W.; Du, H.; Chen, L.; Li, Y.; Xie, H. Thermal Conductivity of Composite Materials Containing Copper Nanowires. *Thermal Conductivity of Composite Materials Containing Copper Nanowires* **2016,** *2016*, 6.

16. Noh, Y. J.; Kim, S. Y. Synergistic Improvement of Thermal Conductivity in Polymer Composites Filled with Pitch Based Carbon Fiber and Graphene Nanoplatelets. *Synergistic Improvement of Thermal Conductivity in Polymer Composites Filled with Pitch Based Carbon Fiber and Graphene Nanoplatelets* **2015,** *45*, 132-138.

17. Chen, S.; Feng, Y.; Qin, M.; Ji, T.; Feng, W. Improving Thermal Conductivity in the through-Thickness Direction of Carbon Fibre/Sic Composites by Growing Vertically Aligned Carbon Nanotubes. *Improving Thermal Conductivity in the through-Thickness Direction of Carbon Fibre/Sic Composites by Growing Vertically Aligned Carbon Nanotubes* **2017,** *116*, 84-93.

18. Uetani, K.; Ata, S.; Tomonoh, S.; Yamada, T.; Yumura, M.; Hata, K. Elastomeric Thermal Interface Materials with High through-Plane Thermal Conductivity from Carbon Fiber Fillers Vertically Aligned by Electrostatic Flocking. *Elastomeric Thermal Interface Materials with High through-Plane Thermal Conductivity from Carbon Fiber Fillers Vertically Aligned by Electrostatic Flocking* **2014,** *26*, 5857-5862.

19. Biercuk, M. J.; Llaguno, M. C.; Radosavljevic, M.; Hyun, J. K.; Johnson, A. T.; Fischer, J. E. Carbon Nanotube Composites for Thermal Management. *Carbon Nanotube Composites for Thermal Management* **2002,** *80*, 2767-2769.

20. Marconnet, A. M.; Yamamoto, N.; Panzer, M. A.; Wardle, B. L.; Goodson, K. E. Thermal Conduction in Aligned Carbon Nanotube–Polymer Nanocomposites with High Packing Density. *Thermal Conduction in Aligned Carbon Nanotube–Polymer Nanocomposites with High Packing Density* **2011,** *5*, 4818-4825.

21. Han, S.; Chung, D. D. L. Increasing the through-Thickness Thermal Conductivity of Carbon Fiber Polymer–Matrix Composite by Curing Pressure Increase and Filler Incorporation. *Increasing the through-Thickness Thermal Conductivity of Carbon Fiber Polymer–Matrix Composite by Curing Pressure Increase and Filler Incorporation* **2011,** *71*, 1944-1952.

22. Silva, C. A.; Marotta, E.; Schuller, M.; Peel, L.; O'Neill, M. In-Plane Thermal Conductivity in Thin Carbon Fiber Composites. *In-Plane Thermal Conductivity in Thin Carbon Fiber Composites* **2007,** *21*, 460-467.

23. Zhang, Y.-F.; Han, D.; Zhao, Y.-H.; Bai, S.-L. High-Performance Thermal Interface Materials Consisting of Vertically Aligned Graphene Film and Polymer. *High-Performance Thermal Interface Materials Consisting of Vertically Aligned Graphene Film and Polymer* **2016,** *109*, 552-557.

24. Kim, K.; Ju, H.; Kim, J. Vertical Particle Alignment of Boron Nitride and Silicon Carbide Binary Filler System for Thermal Conductivity Enhancement. *Vertical Particle Alignment of Boron Nitride and Silicon Carbide Binary Filler System for Thermal Conductivity Enhancement* **2016,** *123*, 99-105.

25. Han, Z.; Fina, A. Thermal Conductivity of Carbon Nanotubes and Their Polymer Nanocomposites: A Review. *Thermal Conductivity of Carbon Nanotubes and Their Polymer Nanocomposites: A Review* **2011,** *36*, 914-944.

26. Green, C. E.; Prinzi, L.; Cola, B. A. In *Design and Evaluation of Polymer-Carbon Nanotube Composites for Reliable, Low Resistance, Static and Dynamic Thermal Interface Materials*, 2016 15th IEEE Intersociety Conference on Thermal and Thermomechanical Phenomena in Electronic Systems (ITherm), May 31 2016-June 3 2016; 2016; pp 657-661.

27. Huang, X.; Jiang, P.; Tanaka, T. A Review of Dielectric Polymer Composites with High Thermal Conductivity. *A Review of Dielectric Polymer Composites with High Thermal Conductivity* **2011,** *27*, 8-16.

28. Fu, Y.-X.; He, Z.-X.; Mo, D.-C.; Lu, S.-S. Thermal Conductivity Enhancement with Different Fillers for Epoxy Resin Adhesives. *Thermal Conductivity Enhancement with Different Fillers for Epoxy Resin Adhesives* **2014,** *66*, 493-498.

29. Xu, Y.; Chung, D. D. L.; Mroz, C. Thermally Conducting Aluminum Nitride Polymer-Matrix Composites. *Thermally Conducting Aluminum Nitride Polymer-Matrix Composites* **2001,** *32*, 1749-1757.

30. Kemaloglu, S.; Ozkoc, G.; Aytac, A. Properties of Thermally Conductive Micro and Nano Size Boron Nitride Reinforced Silicon Rubber Composites. *Properties of*

Thermally Conductive Micro and Nano Size Boron Nitride Reinforced Silicon Rubber Composites **2010,** *499*, 40-47.

31. Zhou, W.; Wang, C.; Ai, T.; Wu, K.; Zhao, F.; Gu, H. A Novel Fiber-Reinforced Polyethylene Composite with Added Silicon Nitride Particles for Enhanced Thermal Conductivity. *A Novel Fiber-Reinforced Polyethylene Composite with Added Silicon Nitride Particles for Enhanced Thermal Conductivity* **2009,** *40*, 830-836.

32. Boubakeur Essedik, B.; Amine, A.; Dongyan, Z.; Salah, S.; Djouadi, M. A.; Yoke Khin, Y. Thermal Conductivity of Vertically Aligned Boron Nitride Nanotubes. *Thermal Conductivity of Vertically Aligned Boron Nitride Nanotubes* **2016,** *9*, 075002.

33. Klett, J. W.; McMillan, A. D.; Gallego, N. C.; Walls, C. A. The Role of Structure on the Thermal Properties of Graphitic Foams. *The Role of Structure on the Thermal Properties of Graphitic Foams* **2004,** *39*, 3659-3676.

34. Song, J.-l.; Guo, Q.-g.; Zhong, Y.-j.; Gao, X.-q.; Feng, Z.-h.; Fan, Z.; Shi, J.-l.; Liu, L. Thermophysical Properties of High-Density Graphite Foams and Their Paraffin Composites. *Thermophysical Properties of High-Density Graphite Foams and Their Paraffin Composites* **2012,** *27*, 27-34.

35. Calmidi, V.; Mahajan, R. The Effective Thermal Conductivity of High Porosity Fibrous Metal Foams. *The Effective Thermal Conductivity of High Porosity Fibrous Metal Foams* **1999,** *121*, 466-471.

36. Xiao, X.; Zhang, P.; Li, M. Effective Thermal Conductivity of Open-Cell Metal Foams Impregnated with Pure Paraffin for Latent Heat Storage. *Effective Thermal Conductivity of Open-Cell Metal Foams Impregnated with Pure Paraffin for Latent Heat Storage* **2014,** *81*, 94-105.

37. Moeini Sedeh, M.; Khodadadi, J. M. Thermal Conductivity Improvement of Phase Change Materials/Graphite Foam Composites. *Thermal Conductivity Improvement of Phase Change Materials/Graphite Foam Composites* **2013,** *60*, 117-128.

38. Klett, J.; Hardy, R.; Romine, E.; Walls, C.; Burchell, T. High-Thermal-Conductivity, Mesophase-Pitch-Derived Carbon Foams: Effect of Precursor on Structure and Properties. *High-Thermal-Conductivity, Mesophase-Pitch-Derived Carbon Foams: Effect of Precursor on Structure and Properties* **2000,** *38*, 953-973.

39. Zhang, X.; Yeung, K. K.; Gao, Z.; Li, J.; Sun, H.; Xu, H.; Zhang, K.; Zhang, M.; Chen, Z.; Yuen, M. M. Exceptional Thermal Interface Properties of a Three-Dimensional Graphene Foam. *Exceptional Thermal Interface Properties of a Three-Dimensional Graphene Foam* **2014,** *66*, 201-209.

40. Zhao, Y.-H.; Wu, Z.-K.; Bai, S.-L. Thermal Resistance Measurement of 3d Graphene Foam/Polymer Composite by Laser Flash Analysis. *Thermal Resistance Measurement of 3d Graphene Foam/Polymer Composite by Laser Flash Analysis* **2016,** *101*, 470-475.

41. Choy, C. L.; Ong, E. L.; Chen, F. C. Thermal Diffusivity and Conductivity of Crystalline Polymers. *Thermal Diffusivity and Conductivity of Crystalline Polymers* **1981,** *26*, 2325-2335.

42. Choy, C. L.; Young, K. Thermal Conductivity of Semicrystalline Polymers — a Model. *Thermal Conductivity of Semicrystalline Polymers — a Model* **1977,** *18*, 769-776.

43. Choy, C. L.; Luk, W. H.; Chen, F. C. Thermal Conductivity of Highly Oriented Polyethylene. *Thermal Conductivity of Highly Oriented Polyethylene* **1978,** *19*, 155-162.

44. Hansen, D.; Bernier, G. A. Thermal Conductivity of Polyethylene: The Effects of Crystal Size, Density and Orientation on the Thermal Conductivity. *Thermal Conductivity of Polyethylene: The Effects of Crystal Size, Density and Orientation on the Thermal Conductivity* **1972,** *12*, 204-208.

45. Fujishiro, H.; Ikebe, M.; Kashima, T.; Yamanaka, A. Thermal Conductivity and Diffusivity of High-Strength Polymer Fibers. *Thermal Conductivity and Diffusivity of High-Strength Polymer Fibers* **1997,** *36*, 5633-5637.

46. Wang, X.; Ho, V.; Segalman, R. A.; Cahill, D. G. Thermal Conductivity of High-Modulus Polymer Fibers. *Thermal Conductivity of High-Modulus Polymer Fibers* **2013,** *46*, 4937-4943.

47. Loomis, J.; Ghasemi, H.; Huang, X.; Thoppey, N.; Wang, J.; Tong, J. K.; Xu, Y.; Li, X.; Lin, C.-T.; Chen, G. Continuous Fabrication Platform for Highly Aligned Polymer Films. *Continuous Fabrication Platform for Highly Aligned Polymer Films* **2014,** 1-11.

48. Smith, P.; Lemstra, P. J. Ultra-High-Strength Polyethylene Filaments by Solution Spinning/Drawing. *Ultra-High-Strength Polyethylene Filaments by Solution Spinning/Drawing* **1980,** *15*, 505-514.

49. Fukushima, Y.; Murase, H.; Ohta, Y., Dyneema®: Super Fiber Produced by the Gel Spinning of a Flexible Polymer. In *High-Performance and Specialty Fibers*, Springer: 2016; pp 109-132.

50. O'Connor, T. C.; Robbins, M. O. Chain Ends and the Ultimate Strength of Polyethylene Fibers. *Chain Ends and the Ultimate Strength of Polyethylene Fibers* **2016,** *5*, 263-267.

51. Shen, S.; Henry, A.; Tong, J.; Zheng, R.; Chen, G. Polyethylene Nanofibres with Very High Thermal Conductivities. *Polyethylene Nanofibres with Very High Thermal Conductivities* **2010,** *5*, 251-255.

52. Ma, J.; Zhang, Q.; Zhang, Y.; Zhou, L.; Yang, J.; Ni, Z. A Rapid and Simple Method to Draw Polyethylene Nanofibers with Enhanced Thermal Conductivity. *A Rapid and Simple Method to Draw Polyethylene Nanofibers with Enhanced Thermal Conductivity* **2016,** *109*, 033101.

53. Lu, C.; Chiang, S. W.; Du, H.; Li, J.; Gan, L.; Zhang, X.; Chu, X.; Yao, Y.; Li, B.; Kang, F. Thermal Conductivity of Electrospinning Chain-Aligned Polyethylene Oxide (Peo). *Thermal Conductivity of Electrospinning Chain-Aligned Polyethylene Oxide (Peo)*.

54. Ma, J.; Zhang, Q.; Mayo, A.; Ni, Z.; Yi, H.; Chen, Y.; Mu, R.; Bellan, L. M.; Li, D. Thermal Conductivity of Electrospun Polyethylene Nanofibers. *Thermal Conductivity of Electrospun Polyethylene Nanofibers* **2015,** *7*, 16899-16908.

55. Zhong, Z.; Wingert, M. C.; Strzalka, J.; Wang, H.-H.; Sun, T.; Wang, J.; Chen, R.; Jiang, Z. Structure-Induced Enhancement of Thermal Conductivities in Electrospun Polymer Nanofibers. *Structure-Induced Enhancement of Thermal Conductivities in Electrospun Polymer Nanofibers* **2014,** *6*, 8283-8291.

56. Singh, V.; Bougher, T. L.; Weathers, A.; Cai, Y.; Bi, K.; Pettes, M. T.; McMenamin, S. A.; Lv, W.; Resler, D. P.; Gattuso, T. R., *et al.* High Thermal Conductivity in Chain-Oriented Amorphous Polythiophene. *High Thermal Conductivity in Chain-Oriented Amorphous Polythiophene* **2014,** *9*, 384-390.

57. Cao, B. Y.; Li, Y. W.; Kong, J.; Chen, H.; Xu, Y.; Yung, K. L.; Cai, A. High Thermal Conductivity of Polyethylene Nanowire Arrays Fabricated by an Improved Nanoporous Template Wetting Technique. *High Thermal Conductivity of Polyethylene Nanowire Arrays Fabricated by an Improved Nanoporous Template Wetting Technique* **2011,** *52*, 1711-1715.

58. Bougher, T. L.; Smith, M. K.; Kalaitzidou, K.; Cola, B. A. In *Thermal Conductivity of Melt-Processed Nanofibers*, Thermal and Thermomechanical Phenomena in Electronic Systems (ITherm), 2016 15th IEEE Intersociety Conference on, IEEE: 2016; pp 1354-1359.

59. Schlitt, S.; Greiner, A.; Wendorff, J. H. Cylindrical Polymer Nanostructures by Solution Template Wetting. *Cylindrical Polymer Nanostructures by Solution Template Wetting* **2008,** *41*, 3228–3234.

60. Shirai, Y.; Takami, S.; Lasmono, S.; Iwai, H.; Chikyow, T.; Wakayama, Y. Improvement in Carrier Mobility of Poly(3,4-Ethylenedioxythiophene) Nanowires Synthesized in Porous Alumina Templates. *Improvement in Carrier Mobility of Poly(3,4-Ethylenedioxythiophene) Nanowires Synthesized in Porous Alumina Templates* **2011,** *49*, 1762-1768.

61. Steinhart, M.; Wendorff, J.; Greiner, A.; Wehrspohn, R.; Nielsch, K.; Schilling, J.; Choi, J.; Gösele, U. Polymer Nanotubes by Wetting of Ordered Porous Templates. *Polymer Nanotubes by Wetting of Ordered Porous Templates* **2002,** *296*, 1997.

62. Smith, M. K.; Singh, V.; Kalaitzidou, K.; Cola, B. A. High Thermal and Electrical Conductivity of Template Fabricated P3ht/Mwcnt Composite Nanofibers. *High Thermal and Electrical Conductivity of Template Fabricated P3ht/Mwcnt Composite Nanofibers* **2016,** *8*, 14788-14794.

63. Bougher, T. L.; Singh, V.; Cola, B. A. In *Thermal Interface Materials from Vertically Aligned Polymer Nanotube Arrays*, Proceedings of the ASME 4th Micro/Nanoscale Heat & Mass Transfer Conference, Hong Kong, ASME: Hong Kong, 2013.

64. Holliday, S.; Ashraf, R. S.; Wadsworth, A.; Baran, D.; Yousaf, S. A.; Nielsen, C. B.; Tan, C.-H.; Dimitrov, S. D.; Shang, Z.; Gasparini, N. High-Efficiency and Air-Stable P3ht-Based Polymer Solar Cells with a New Non-Fullerene Acceptor. *High-Efficiency and Air-Stable P3ht-Based Polymer Solar Cells with a New Non-Fullerene Acceptor* **2016,** *7*.

65. Taphouse, J. H.; Bougher, T. L.; Singh, V.; Abadi, P. P. S. S.; Graham, S.; Cola, B. A. Carbon Nanotube Thermal Interfaces Enhanced with Sprayed on Nanoscale Polymer Coatings. *Carbon Nanotube Thermal Interfaces Enhanced with Sprayed on Nanoscale Polymer Coatings* **2013,** *24*, 105401.

66. Lin, J.; Peng, Z.; Liu, Y.; Ruiz-Zepeda, F.; Ye, R.; Samuel, E. L. G.; Yacaman, M. J.; Yakobson, B. I.; Tour, J. M. Laser-Induced Porous Graphene Films from Commercial Polymers. *Laser-Induced Porous Graphene Films from Commercial Polymers* **2014,** *5*, 5714.

67. Martin, C. R. Membrane-Based Synthesis of Nanomaterials. *Membrane-Based Synthesis of Nanomaterials* **1996,** *8*, 1739-1746.

68. Martin, C. R. Template Synthesis of Electronically Conductive Polymer Nanostructures. *Template Synthesis of Electronically Conductive Polymer Nanostructures* **1995,** *28*, 61-68.

69. Duvail, J. L.; Retho, P.; Fernandez, V.; Louarn, G.; Molinie, P.; Chauvet, O. Effects of the Confined Synthesis on Conjugated Polymer Transport Properties. *Effects of the Confined Synthesis on Conjugated Polymer Transport Properties* **2004,** *108*, 18552-18556.

70. Choy, C. L.; Fei, Y.; Xi, T. G. Thermal-Conductivity of Gel-Spun Polyethylene Fibers. *Thermal-Conductivity of Gel-Spun Polyethylene Fibers* **1993,** *31*, 365-370.

71. Singh, V.; Bougher, T. L.; Weathers, A.; Cai, Y.; Bi, K.; Pettes, M. T.; McMenamin, S. A.; Lv, W.; Resler, D. P.; Gattuso, T. R., *et al.* High Thermal Conductivity of Chain-Oriented Amorphous Polythiophene. *High Thermal Conductivity of Chain-Oriented Amorphous Polythiophene* **2014,** *9*, 384-390.

72. Papkov, D.; Zou, Y.; Andalib, M.; Goponenko, A.; Cheng, S.; Dzenis, Y. Simultaneously Strong and Tough Ultrafine Continuous Nanofibers. *Simultaneously Strong and Tough Ultrafine Continuous Nanofibers* **2013,** *7*, 3324-3331.

73. Lu, G.; Hong, W.; Tong, L.; Bai, H.; Wei, Y.; Shi, G. Drying Enhanced Adhesion of Polythiophene Nanotubule Arrays on Smooth Surfaces. *Drying Enhanced Adhesion of Polythiophene Nanotubule Arrays on Smooth Surfaces* **2008,** *2*, 2342-2348.

74. Tadmor, Z.; Gogos, C. G. Injection Molding. In *Principles of polymer processing*; John Wiley & Sons: New York, 2006.

75. Cao, B.-Y.; Kong, J.; Xu, Y.; Yung, K.-L.; Cai, A. Polymer Nanowire Arrays with High Thermal Conductivity and Superhydrophobicity Fabricated by a Nano-Molding Technique. *Polymer Nanowire Arrays with High Thermal Conductivity and Superhydrophobicity Fabricated by a Nano-Molding Technique* **2013,** *34*, 131-139.

76. Jin, M.; Feng, X.; Feng, L.; Sun, T.; Zhai, J.; Li, T.; Jiang, L. Superhydrophobic Aligned Polystyrene Nanotube Films with High Adhesive Force. *Superhydrophobic Aligned Polystyrene Nanotube Films with High Adhesive Force* **2005,** *17*, 1977-1981.

77. Mao, C.; Liang, C.; Luo, W.; Bao, J.; Shen, J.; Hou, X.; Zhao, W. Preparation of Lotus-Leaf-Like Polystyrene Micro- and Nanostructure Films and Its Blood Compatibility. *Preparation of Lotus-Leaf-Like Polystyrene Micro- and Nanostructure Films and Its Blood Compatibility* **2009,** *19*, 9025-9029.

78. Liao, Y. C.; Chiang, C. K.; Lu, Y. W. Contact Angle Hysteresis on Textured Surfaces with Nanowire Clusters. *Contact Angle Hysteresis on Textured Surfaces with Nanowire Clusters* **2013,** *13*, 2729-2734.

79. Xu, J.; Li, M.; Zhao, Y.; Lu, Q. Control over the Hydrophobic Behavior of Polystyrene Surface by Annealing Temperature Based on Capillary Template Wetting Method. *Control over the Hydrophobic Behavior of Polystyrene Surface by Annealing Temperature Based on Capillary Template Wetting Method* **2007,** *302*, 136-140.

80. Li, H.; Wang, X.; Song, Y.; Liu, Y.; Li, Q.; Jiang, L.; Zhu, D. Super-"Amphiphobic" Aligned Carbon Nanotube Films. *Super-"Amphiphobic" Aligned Carbon Nanotube Films* **2001,** *40*, 1743-1746.

81. Bico, J.; Roman, B.; Moulin, L.; Boudaoud, A. Adhesion: Elastocapillary Coalescence in Wet Hair. *Adhesion: Elastocapillary Coalescence in Wet Hair* **2004,** *432*, 690-690.

82. Arezki, B.; José, B.; Benoît, R. Elastocapillary Coalescence: Aggregation and Fragmentation with a Maximal Size. *Elastocapillary Coalescence: Aggregation and Fragmentation with a Maximal Size* **2007,** *76*, 060102.

83. Hill, J.; Haller, K.; Gelfand, B.; Ziegler, K. Eliminating Capillary Coalescence of Nanowire Arrays with Applied Electric Fields. *Eliminating Capillary Coalescence of Nanowire Arrays with Applied Electric Fields* **2010,** *2*, 1992-1998.

84. Duan, H.; Berggren, K. Directed Self-Assembly at the 10 Nm Scale by Using Capillary Force-Induced Nanocohesion. *Directed Self-Assembly at the 10 Nm Scale by Using Capillary Force-Induced Nanocohesion* **2010,** *10*, 3710-3716.

85. Barthlott, W.; Neinhuis, C. Purity of the Sacred Lotus, or Escape from Contamination in Biological Surfaces. *Purity of the Sacred Lotus, or Escape from Contamination in Biological Surfaces* **1997,** *202*, 1-8.

86. Feng, L.; Zhang, Y.; Xi, J.; Zhu, Y.; Wang, N.; Xia, F.; Jiang, L. Petal Effect: A Superhydrophobic State with High Adhesive Force. *Petal Effect: A Superhydrophobic State with High Adhesive Force* **2008,** *24*, 4114-4119.

87. Dawood, M. K.; Zheng, H.; Kurniawan, N. A.; Leong, K. C.; Foo, Y. L.; Rajagopalan, R.; Khan, S. A.; Choi, W. K. Modulation of Surface Wettability of Superhydrophobic Substrates Using Si Nanowire Arrays and Capillary-Force-Induced Nanocohesion. *Modulation of Surface Wettability of Superhydrophobic Substrates Using Si Nanowire Arrays and Capillary-Force-Induced Nanocohesion* **2012,** *8*, 3549-3557.

88. Indrani, C.; Neha, S.; Smita, G.; Shankar, G.; Pushan, A. Clustered Copper Nanorod Arrays: A New Class of Adhesive Hydrophobic Materials. *Clustered Copper Nanorod Arrays: A New Class of Adhesive Hydrophobic Materials* **2013,** *9*, 11513-11520.

89. Kang, S.; Pokroy, B.; Mahadevan, L.; Aizenberg, J. Control of Shape and Size of Nanopillar Assembly by Adhesion-Mediated Elastocapillary Interaction. *Control of Shape and Size of Nanopillar Assembly by Adhesion-Mediated Elastocapillary Interaction* **2010,** *4*, 6323-6331.

90. Cola, B. A.; Xu, J.; Cheng, C. R.; Xu, X. F.; Fisher, T. S.; Hu, H. P. Photoacoustic Characterization of Carbon Nanotube Array Thermal Interfaces. *Photoacoustic Characterization of Carbon Nanotube Array Thermal Interfaces* **2007,** *101*, 054313.

91. Taphouse, J. H.; Smith, O. N. L.; Marder, S. R.; Cola, B. A. A Pyrenylpropyl Phosphonic Acid Surface Modifier for Mitigating the Thermal Resistance of Carbon Nanotube Contacts. *A Pyrenylpropyl Phosphonic Acid Surface Modifier for Mitigating the Thermal Resistance of Carbon Nanotube Contacts* **2014,** *24*, 465-471.

92. Tao, T.; Yang, Z.; Lance, D.; Ali, K.; Meyyappan, M.; Arun, M. Dense Vertically Aligned Multiwalled Carbon Nanotube Arrays as Thermal Interface Materials. *Dense Vertically Aligned Multiwalled Carbon Nanotube Arrays as Thermal Interface Materials* **2007,** *30*, 92-100.

93. Steinhart, M.; Wehrspohn, R.; Gösele, U.; Wendorff, J. Nanotubes by Template Wetting: A Modular Assembly System. *Nanotubes by Template Wetting: A Modular Assembly System* **2004,** *43*, 1334-1344.

94. Gennes; F.; D.; A.; B. Capillarity and Wetting Phenomena: Drops, Bubbles, Pearls, Waves. *Capillarity and Wetting Phenomena: Drops, Bubbles, Pearls, Waves* **2004,** *57*, 120000-120067.

95. Chi, M.-H.; Kao, Y.-H.; Wei, T.-H.; Lee, C.-W.; Chen, J.-T. Curved Polymer Nanodiscs by Wetting Nanopores of Anodic Aluminum Oxide Templates with Polymer

Nanospheres. *Curved Polymer Nanodiscs by Wetting Nanopores of Anodic Aluminum Oxide Templates with Polymer Nanospheres* **2014,** *6*, 1340-1346.

96. Shanmugham, S.; Jeong, J.; Alkhateeb, A.; Aston, E. D. Polymer Nanowire Elastic Moduli Measured with Digital Pulsed Force Mode Afm. *Polymer Nanowire Elastic Moduli Measured with Digital Pulsed Force Mode Afm* **2005,** *21*, 10214-10218.

97. Chakrapani, N.; Wei, B.; Carrillo, A.; Ajayan, P. M.; Kane, R. S. Capillarity-Driven Assembly of Two-Dimensional Cellular Carbon Nanotube Foams. *Capillarity-Driven Assembly of Two-Dimensional Cellular Carbon Nanotube Foams* **2004,** *101*, 4009-4012.

98. Holmes-Farley, S.; Reamey, R. H.; Nuzzo, R.; McCarthy, T. J.; Whitesides, G. M. Reconstruction of the Interface of Oxidatively Functionalized Polyethylene and Derivatives on Heating. *Reconstruction of the Interface of Oxidatively Functionalized Polyethylene and Derivatives on Heating* **1987,** *3*, 799-815.

99. Manceau, M.; Rivaton, A.; Gardette, J. L.; Guillerez, S.; Lemaitre, N. The Mechanism of Photo- and Thermooxidation of Poly(3-Hexylthiophene) (P3ht) Reconsidered. *The Mechanism of Photo- and Thermooxidation of Poly(3-Hexylthiophene) (P3ht) Reconsidered* **2009,** *94*, 898-907.

100. Jeong, M. G.; Seo, H. O.; Kim, D. H.; Kim, K. D.; Park, E. J.; Kim, Y. D.; Lim, D. C. Initial Stage of Photoinduced Oxidation of Poly(3-Hexylthiophene-2,5-Diyl) Layers on Zno under Dry and Humid Air. *Initial Stage of Photoinduced Oxidation of Poly(3-Hexylthiophene-2,5-Diyl) Layers on Zno under Dry and Humid Air* **2014,** *118*, 3483-3489.

101. Tan, E. P.; Lim, C. T. Effects of Annealing on the Structural and Mechanical Properties of Electrospun Polymeric Nanofibres. *Effects of Annealing on the Structural and Mechanical Properties of Electrospun Polymeric Nanofibres* **2006,** *17*, 2649-2654.

102. Wong, T.-S.; Sun, T.; Feng, L.; Aizenberg, J. Interfacial Materials with Special Wettability. *Interfacial Materials with Special Wettability* **2013,** *38*, 366-371.

103. Gao, L.; McCarthy, T. J. How Wenzel and Cassie Were Wrong. *How Wenzel and Cassie Were Wrong* **2007,** *23*, 3762-3765.

104. Gao, L.; McCarthy, T. J. An Attempt to Correct the Faulty Intuition Perpetuated by the Wenzel and Cassie "Laws". *An Attempt to Correct the Faulty Intuition Perpetuated by the Wenzel and Cassie "Laws"* **2009,** *25*, 7249-7255.

105. Extrand, C. W. Model for Contact Angles and Hysteresis on Rough and Ultraphobic Surfaces. *Model for Contact Angles and Hysteresis on Rough and Ultraphobic Surfaces* **2002,** *18*, 7991-7999.

106. Choi, W.; Tuteja, A.; Mabry, J. M.; Cohen, R. E.; McKinley, G. H. A Modified Cassie-Baxter Relationship to Explain Contact Angle Hysteresis and Anisotropy on Non-Wetting Textured Surfaces. *A Modified Cassie-Baxter Relationship to Explain Contact Angle Hysteresis and Anisotropy on Non-Wetting Textured Surfaces* **2009,** *339*, 208-216.

107. Hanping, H.; Xinwei, W.; Xianfan, X. Generalized Theory of the Photoacoustic Effect in a Multilayer Material. *Generalized Theory of the Photoacoustic Effect in a Multilayer Material* **1999,** *86*.

108. Cola, B. A.; Xu, J.; Cheng, C. R.; Xu, X. F.; Fisher, T. S.; Hu, H. P. Photoacoustic Characterization of Carbon Nanotube Array Thermal Interfaces. *Photoacoustic Characterization of Carbon Nanotube Array Thermal Interfaces* **2007,** *101*.

109. Duda, J. C.; Hopkins, P. E.; Shen, Y.; Gupta, M. C. Thermal Transport in Organic Semiconducting Polymers. *Thermal Transport in Organic Semiconducting Polymers* **2013,** *102*, 251912.

110. Rojo, M. M.; Martin, J.; Grauby, S.; Borca-Tasciuc, T.; Dilhaire, S.; Martin-Gonzalez, M. Decrease in Thermal Conductivity in Polymeric P3ht Nanowires by Size-Reduction Induced by Crystal Orientation: New Approaches Towards Thermal Transport Engineering of Organic Materials. *Decrease in Thermal Conductivity in Polymeric P3ht Nanowires by Size-Reduction Induced by Crystal Orientation: New Approaches Towards Thermal Transport Engineering of Organic Materials* **2014,** *6*, 7858-7865.

111. Choy, C. L.; Chen, F. C.; Luk, W. H. Thermal Conductivity of Oriented Crystalline Polymers. *Thermal Conductivity of Oriented Crystalline Polymers* **1980,** *18*, 1187-1207.

112. Choy, C. L. Thermal Conductivity of Polymers. *Thermal Conductivity of Polymers* **1977,** *18*, 984-1004.

113. Choy, C. L.; Wong, Y. W.; Yang, G. W.; Kanamoto, T. Elastic Modulus and Thermal Conductivity of Ultradrawn Polyethylene. *Elastic Modulus and Thermal Conductivity of Ultradrawn Polyethylene* **1999,** *37*, 3359-3367.

114. Shen, S.; Henry, A.; Tong, J.; Zheng, R. T.; Chen, G. Polyethylene Nanofibres with Very High Thermal Conductivities. *Polyethylene Nanofibres with Very High Thermal Conductivities* **2010,** *5*, 251-255.

115. Henry, A.; Chen, G.; Plimpton, S. J.; Thompson, A. 1d-to-3d Transition of Phonon Heat Conduction in Polyethylene Using Molecular Dynamics Simulations. *1d-to-3d Transition of Phonon Heat Conduction in Polyethylene Using Molecular Dynamics Simulations* **2010,** *82*, 144308.

116. Singh, V.; Bougher, T. L.; Weathers, A.; Cai, Y.; Bi, K.; Pettes, M. T.; McMenamin, S. A.; Lv, W.; Resler, D. P.; Gattuso, T. R. High Thermal Conductivity of Chain-Oriented Amorphous Polythiophene. *High Thermal Conductivity of Chain-Oriented Amorphous Polythiophene* **2014**.

117. Smith, M. K.; Singh, V.; Kalaitzidou, K.; Cola, B. A. Poly(3-Hexylthiophene) Nanotube Array Surfaces with Tunable Wetting and Contact Thermal Energy Transport. *Poly(3-Hexylthiophene) Nanotube Array Surfaces with Tunable Wetting and Contact Thermal Energy Transport* **2015,** *9*, 1080-1088.

118. Lee, Y.-J.; Jeng, K.-S.; Chen, J.-T.; Sun, K. W. Exceptionally Low Thermal Conductivity of Poly (3-Hexylthiophene) Single Nanowires. *Exceptionally Low Thermal Conductivity of Poly (3-Hexylthiophene) Single Nanowires* **2015,** *5*, 90847-90851.

119. Wang, X.; Cola, B. A.; Bougher, T. L.; Hodson, S. L.; Fisher, T. S.; Xu, X. Photoacoustic Technique for Thermal Conductivity and Thermal Interface Measurements. In *Annual Review of Heat Transfer*; Begell House, Inc: Danbury, Connecticut, 2013; Vol. 16, pp 135-157.

120. Hanping, H.; Xinwei, W.; Xianfan, X. Generalized Theory of the Photoacoustic Effect in a Multilayer Material. *Generalized Theory of the Photoacoustic Effect in a Multilayer Material* **1999,** *86*, 3593.

121. Citra, M. J.; Chase, D. B.; Ikeda, R. M.; Gardner, K. H. Molecular Orientation of High-Density Polyethylene Fibers Characterized by Polarized Raman Spectroscopy. *Molecular Orientation of High-Density Polyethylene Fibers Characterized by Polarized Raman Spectroscopy* **1995,** *28*, 4007-4012.

122. Gall, M.; Hendra, P.; Peacock, O.; Cudby, M.; Willis, H. The Laser-Raman Spectrum of Polyethylene: The Assignment of the Spectrum to Fundamental Modes of Vibration. *The Laser-Raman Spectrum of Polyethylene: The Assignment of the Spectrum to Fundamental Modes of Vibration* **1972,** *28*, 1485-1496.

123. Pigeon, M.; Prud'Homme, R. E.; Pezolet, M. Characterization of Molecular Orientation in Polyethylene by Raman Spectroscopy. *Characterization of Molecular Orientation in Polyethylene by Raman Spectroscopy* **1991,** *24*, 5687-5694.

124. Puppulin, L.; Takahashi, Y.; Zhu, W.; Pezzotti, G. Raman Polarization Analysis of Highly Crystalline Polyethylene Fiber. *Raman Polarization Analysis of Highly Crystalline Polyethylene Fiber* **2011,** *42*, 482-487.

125. Xiao, G.; Sun, Y.; Xu, W.; Lin, Y.; Su, Z.; Wang, Q. Large-Scale Highly Ordered Hierarchical Structures of Conjugated Polymer Via Self-Assembly from Mixed Solvents. *Large-Scale Highly Ordered Hierarchical Structures of Conjugated Polymer Via Self-Assembly from Mixed Solvents* **2015,** *5*, 76472-76475.

126. Veerender, P.; Saxena, V.; Chauhan, A. K.; Koiry, S. P.; Jha, P.; Gusain, A.; Choudhury, S.; Aswal, D. K.; Gupta, S. K. Probing the Annealing Induced Molecular Ordering in Bulk Heterojunction Polymer Solar Cells Using in-Situ Raman Spectroscopy. *Probing the Annealing Induced Molecular Ordering in Bulk Heterojunction Polymer Solar Cells Using in-Situ Raman Spectroscopy* **2014,** *120, Part B*, 526-535.

127. Sun, Y.; Xiao, G.; Lin, Y.; Su, Z.; Wang, Q. Self-Assembly of Large-Scale P3ht Patterns by Confined Evaporation in the Capillary Tube. *Self-Assembly of Large-Scale P3ht Patterns by Confined Evaporation in the Capillary Tube* **2015,** *5*, 20491-20497.

128. Cheng, H.-L.; Lin, J.-W.; Jang, M.-F.; Wu, F.-C.; Chou, W.-Y.; Chang, M.-H.; Chao, C.-H. Long-Term Operations of Polymeric Thin-Film Transistors: Electric-Field-

Induced Intrachain Order and Charge Transport Enhancements of Conjugated Poly(3-Hexylthiophene). *Long-Term Operations of Polymeric Thin-Film Transistors: Electric-Field-Induced Intrachain Order and Charge Transport Enhancements of Conjugated Poly(3-Hexylthiophene)* **2009,** *42*, 8251-8259.

129. Shin, K.; Woo, E.; Jeong, Y. G.; Kim, C.; Huh, J.; Kim, K.-W. Crystalline Structures, Melting, and Crystallization of Linear Polyethylene in Cylindrical Nanopores. *Crystalline Structures, Melting, and Crystallization of Linear Polyethylene in Cylindrical Nanopores* **2007,** *40*, 6617-6623.

130. Wang, Z. L.; Tang, D. W.; Li, X. B.; Zheng, X. H.; Zhang, W. G.; Zheng, L. X.; Zhu, Y. T. T.; Jin, A. Z.; Yang, H. F.; Gu, C. Z. Length-Dependent Thermal Conductivity of an Individual Single-Wall Carbon Nanotube. *Length-Dependent Thermal Conductivity of an Individual Single-Wall Carbon Nanotube* **2007,** *91*.

131. Bar-Cohen, A.; Albrecht, J. D.; Maurer, J. J. In *Near-Junction Thermal Management for Wide Bandgap Devices*, 2011 IEEE Compound Semiconductor Integrated Circuit Symposium (CSICS), 16-19 Oct. 2011; 2011; pp 1-5.

132. Hennig, J.; Knappe, W. Anisotropy of Thermal Conductivity in Stretched Amorphous Linear Polymers and in Strained Elastomers. *Anisotropy of Thermal Conductivity in Stretched Amorphous Linear Polymers and in Strained Elastomers* **1964,** *6*, 167-174.

133. Ebbesen, T. W.; Lezec, H. J.; Hiura, H.; Bennett, J. W.; Ghaemi, H. F.; Thio, T. Electrical Conductivity of Individual Carbon Nanotubes. *Electrical Conductivity of Individual Carbon Nanotubes* **1996,** *382*, 54-56.

134. Berber, S.; Kwon, Y.-K.; Tománek, D. Unusually High Thermal Conductivity of Carbon Nanotubes. *Unusually High Thermal Conductivity of Carbon Nanotubes* **2000,** *84*, 4613-4616.

135. Salvetat, J.-P.; Bonard, J.-M.; Thomson, N. H.; Kulik, A. J.; Forró, L.; Benoit, W.; Zuppiroli, L. Mechanical Properties of Carbon Nanotubes. *Mechanical Properties of Carbon Nanotubes* **1999,** *69*, 255-260.

136. Kim, P.; Shi, L.; Majumdar, A.; McEuen, P. L. Thermal Transport Measurements of Individual Multiwalled Nanotubes. *Thermal Transport Measurements of Individual Multiwalled Nanotubes* **2001,** *87*, 215502.

137. Bounioux, C.; Diaz-Chao, P.; Campoy-Quiles, M.; Martin-Gonzalez, M. S.; Goni, A. R.; Yerushalmi-Rozen, R.; Muller, C. Thermoelectric Composites of Poly(3-Hexylthiophene) and Carbon Nanotubes with a Large Power Factor. *Thermoelectric Composites of Poly(3-Hexylthiophene) and Carbon Nanotubes with a Large Power Factor* **2013,** *6*, 918-925.

138. Berson, S.; de Bettignies, R.; Bailly, S.; Guillerez, S.; Jousselme, B. Elaboration of P3ht/Cnt/Pcbm Composites for Organic Photovoltaic Cells. *Elaboration of P3ht/Cnt/Pcbm Composites for Organic Photovoltaic Cells* **2007,** *17*, 3363-3370.

139. Zhang, D.; Kandadai, M. A.; Cech, J.; Roth, S.; Curran, S. A. Poly(L-Lactide) (Plla)/Multiwalled Carbon Nanotube (Mwcnt) Composite: Characterization and Biocompatibility Evaluation. *Poly(L-Lactide) (Plla)/Multiwalled Carbon Nanotube (Mwcnt) Composite: Characterization and Biocompatibility Evaluation* **2006,** *110*, 12910-12915.

140. Martín-Fabiani, I.; García-Gutiérrez, M.-C.; Rueda, D. R.; Linares, A.; Hernández, J. J.; Ezquerra, T. A.; Reynolds, M. Crystallization under One-Dimensional Confinement in Alumina Nanopores of Poly(Trimethylene Terephthalate) and Its Composites with Single Wall Carbon Nanotubes. *Crystallization under One-Dimensional Confinement in Alumina Nanopores of Poly(Trimethylene Terephthalate) and Its Composites with Single Wall Carbon Nanotubes* **2013,** *5*, 5324-5329.

141. Maiz, J.; Sacristan, J.; Mijangos, C. Probing the Presence and Distribution of Single-Wall Carbon Nanotubes in Polyvinylidene Difluoride 1d Nanocomposites by Confocal Raman Spectroscopy. *Probing the Presence and Distribution of Single-Wall Carbon Nanotubes in Polyvinylidene Difluoride 1d Nanocomposites by Confocal Raman Spectroscopy* **2010,** *484*, 290-294.

142. Massuyeau, F.; Zhao, Y.; El Mel, A. A.; Yaya, A.; Geschier, F.; Gautron, E.; Lefrant, S.; Mevellec, J. Y.; Ewels, C.; Hsu, C.-S., *et al.* Improved Photoconductive Properties of Composite Nanofibers Based on Aligned Conjugated Polymer and Single-Walled Carbon Nanotubes. *Improved Photoconductive Properties of Composite Nanofibers Based on Aligned Conjugated Polymer and Single-Walled Carbon Nanotubes* **2013,** *6*, 149-158.

143. Datsyuk, V.; Trotsenko, S.; Reich, S. Carbon-Nanotube–Polymer Nanofibers with High Thermal Conductivity. *Carbon-Nanotube–Polymer Nanofibers with High Thermal Conductivity* **2013,** *52*, 605-608.

144. Chien, A.-T.; Cho, S.; Joshi, Y.; Kumar, S. Electrical Conductivity and Joule Heating of Polyacrylonitrile/Carbon Nanotube Composite Fibers. *Electrical Conductivity and Joule Heating of Polyacrylonitrile/Carbon Nanotube Composite Fibers* **2014,** *55*, 6896-6905.

145. Krishnamoorthy, T.; Thavasi, V.; Subodh G, M.; Ramakrishna, S. A First Report on the Fabrication of Vertically Aligned Anatase Tio2 Nanowires by Electrospinning: Preferred Architecture for Nanostructured Solar Cells. *A First Report on the Fabrication of Vertically Aligned Anatase Tio2 Nanowires by Electrospinning: Preferred Architecture for Nanostructured Solar Cells* **2011,** *4*, 2807-2812.

146. Cola, B. A.; Xu, J.; Cheng, C.; Xu, X.; Fisher, T. S. Photoacoustic Characterization of Carbon Nanotube Array Thermal Interfaces. *Photoacoustic Characterization of Carbon Nanotube Array Thermal Interfaces* **2007,** *101*, 054313.

147. Huang, Y. Y.; Terentjev, E. M. Dispersion of Carbon Nanotubes: Mixing, Sonication, Stabilization, and Composite Properties. *Dispersion of Carbon Nanotubes: Mixing, Sonication, Stabilization, and Composite Properties* **2012,** *4*, 275.

148. Ali, E. A.; Marcio, H. L.; Edward, M. S.; Ray, H. B. Thermal Conductivity of Multi-Walled Carbon Nanotube Sheets: Radiation Losses and Quenching of Phonon Modes. *Thermal Conductivity of Multi-Walled Carbon Nanotube Sheets: Radiation Losses and Quenching of Phonon Modes* **2010,** *21*, 035709.

149. Nicho, M. E.; García-Escobar, C. H.; Arenas, M. C.; Altuzar-Coello, P.; Cruz-Silva, R.; Güizado-Rodríguez, M. Influence of P3ht Concentration on Morphological, Optical and Electrical Properties of P3ht/Ps and P3ht/Pmma Binary Blends. *Influence of P3ht Concentration on Morphological, Optical and Electrical Properties of P3ht/Ps and P3ht/Pmma Binary Blends* **2011,** *176*, 1393-1400.

150. Ramani, R.; Srivastava, J.; Alam, S. Application of Model-Free Kinetics to the Thermal and Thermo-Oxidative Degradation of Poly(3-Hexyl Thiophene). *Application of Model-Free Kinetics to the Thermal and Thermo-Oxidative Degradation of Poly(3-Hexyl Thiophene)* **2010,** *499*, 34-39.

151. Sun, Y.; Han, Y.; Liu, J. Controlling Pcbm Aggregation in P3ht/Pcbm Film by a Selective Solvent Vapor Annealing. *Controlling Pcbm Aggregation in P3ht/Pcbm Film by a Selective Solvent Vapor Annealing* **2013,** *58*, 2767-2774.

152. Laurent, C.; Flahaut, E.; Peigney, A. The Weight and Density of Carbon Nanotubes Versus the Number of Walls and Diameter. *The Weight and Density of Carbon Nanotubes Versus the Number of Walls and Diameter* **2010,** *48*, 2994-2996.

153. Nan, C.-W.; Liu, G.; Lin, Y.; Li, M. Interface Effect on Thermal Conductivity of Carbon Nanotube Composites. *Interface Effect on Thermal Conductivity of Carbon Nanotube Composites* **2004,** *85*, 3549-3551.

154. Hwang, J.; Jang, J.; Hong, K.; Kim, K. N.; Han, J. H.; Shin, K.; Park, C. E. Poly(3-Hexylthiophene) Wrapped Carbon Nanotube/Poly(Dimethylsiloxane) Composites for Use in Finger-Sensing Piezoresistive Pressure Sensors. *Poly(3-Hexylthiophene) Wrapped Carbon Nanotube/Poly(Dimethylsiloxane) Composites for Use in Finger-Sensing Piezoresistive Pressure Sensors* **2011,** *49*, 106-110.

155. Han-Dong, J.; Fei, Z.; Wei-Long, X.; Wei-Hao, Y.; Meng-Qi, Z.; Xiao-Tao, H. The Structure and Optical Properties of Regio-Regular Poly(3-Hexylthiophene) and Carboxylic Multi-Walled Carbon Nanotubes Composite Films. *The Structure and Optical Properties of Regio-Regular Poly(3-Hexylthiophene) and Carboxylic Multi-Walled Carbon Nanotubes Composite Films* **2014,** *47*, 505502.

156. Cannon, J. P.; Bearden, S. D.; Gold, S. A. Characterization of Conjugated Polymer/Anodic Aluminum Oxide Nanocomposites Fabricated Via Template Wetting. *Characterization of Conjugated Polymer/Anodic Aluminum Oxide Nanocomposites Fabricated Via Template Wetting* **2010,** *41*, 836-841.

157. Karim, M. R. Synthesis and Characterizations of Poly(3-Hexylthiophene) and Modified Carbon Nanotube Composites. *Synthesis and Characterizations of Poly(3-Hexylthiophene) and Modified Carbon Nanotube Composites* **2012,** *2012*, 34-34.

158. Kim, G.-H.; Lee, D.; Shanker, A.; Shao, L.; Kwon, M. S.; Gidley, D.; Kim, J.; Pipe, K. P. High Thermal Conductivity in Amorphous Polymer Blends by Engineered Interchain Interactions. *High Thermal Conductivity in Amorphous Polymer Blends by Engineered Interchain Interactions* **2015,** *14*, 295-300.

159. Yung, K.; Liem, H. Enhanced Thermal Conductivity of Boron Nitride Epoxy-Matrix Composite through Multi-Modal Particle Size Mixing. *Enhanced Thermal Conductivity of Boron Nitride Epoxy-Matrix Composite through Multi-Modal Particle Size Mixing* **2007,** *106*, 3587-3591.

160. Wong, C. P.; Bollampally, R. S. Thermal Conductivity, Elastic Modulus, and Coefficient of Thermal Expansion of Polymer Composites Filled with Ceramic Particles for Electronic Packaging. *Thermal Conductivity, Elastic Modulus, and Coefficient of Thermal Expansion of Polymer Composites Filled with Ceramic Particles for Electronic Packaging* **1999,** *74*, 3396-3403.

161. Cola, B. A.; Xu, J.; Cheng, C.; Xu, X.; Fisher, T. S.; Hu, H. Photoacoustic Characterization of Carbon Nanotube Array Thermal Interfaces. *Photoacoustic Characterization of Carbon Nanotube Array Thermal Interfaces* **2007,** *101*, 054313.

162. Shahil, K. M.; Balandin, A. A. Graphene–Multilayer Graphene Nanocomposites as Highly Efficient Thermal Interface Materials. *Graphene–Multilayer Graphene Nanocomposites as Highly Efficient Thermal Interface Materials* **2012,** *12*, 861-867.

163. Huang, X.; Jiang, P.; Xie, L. Ferroelectric Polymer/Silver Nanocomposites with High Dielectric Constant and High Thermal Conductivity. *Ferroelectric Polymer/Silver Nanocomposites with High Dielectric Constant and High Thermal Conductivity* **2009,** *95*, 242901.

164. Chen, H.; Ginzburg, V. V.; Yang, J.; Yang, Y.; Liu, W.; Huang, Y.; Du, L.; Chen, B. Thermal Conductivity of Polymer-Based Composites: Fundamentals and Applications. *Thermal Conductivity of Polymer-Based Composites: Fundamentals and Applications* **2016,** *59*, 41-85.

165. Hong, J.-P.; Yoon, S.-W.; Hwang, T.; Oh, J.-S.; Hong, S.-C.; Lee, Y.; Nam, J.-D. High Thermal Conductivity Epoxy Composites with Bimodal Distribution of Aluminum Nitride and Boron Nitride Fillers. *High Thermal Conductivity Epoxy Composites with Bimodal Distribution of Aluminum Nitride and Boron Nitride Fillers* **2012,** *537*, 70-75.

166. Burger, N.; Laachachi, A.; Ferriol, M.; Lutz, M.; Toniazzo, V.; Ruch, D. Review of Thermal Conductivity in Composites: Mechanisms, Parameters and Theory. *Review of Thermal Conductivity in Composites: Mechanisms, Parameters and Theory* **2016,** *61*, 1-28.

167. Liu, Z.; Shen, D.; Yu, J.; Dai, W.; Li, C.; Du, S.; Jiang, N.; Li, H.; Lin, C.-T. Exceptionally High Thermal and Electrical Conductivity of Three-Dimensional Graphene-Foam-Based Polymer Composites. *Exceptionally High Thermal and Electrical Conductivity of Three-Dimensional Graphene-Foam-Based Polymer Composites* **2016,** *6*, 22364-22369.

168. Hu, H.; Wang, X.; Xu, X. Generalized Theory of the Photoacoustic Effect in a Multilayer Material. *Generalized Theory of the Photoacoustic Effect in a Multilayer Material* **1999,** *86*, 3953-3958.

169. Vargaftik, N. B. Handbook of Thermal Conductivity of Liquids and Gases. In CRC press: 1993.

170. Yu, Q.; Thompson, B. E.; Straatman, A. G. A Unit Cube-Based Model for Heat Transfer and Fluid Flow in Porous Carbon Foam. *A Unit Cube-Based Model for Heat Transfer and Fluid Flow in Porous Carbon Foam* **2005,** *128*, 352-360.

171. Li, M.; Sun, Y.; Xiao, H.; Hu, X.; Yue, Y. High Temperature Dependence of Thermal Transport in Graphene Foam. *High Temperature Dependence of Thermal Transport in Graphene Foam* **2015,** *26*, 105703.

172. Pettes, M. T.; Ji, H.; Ruoff, R. S.; Shi, L. Thermal Transport in Three-Dimensional Foam Architectures of Few-Layer Graphene and Ultrathin Graphite. *Thermal Transport in Three-Dimensional Foam Architectures of Few-Layer Graphene and Ultrathin Graphite* **2012,** *12*, 2959-2964.

173. Shtein, M.; Nadiv, R.; Buzaglo, M.; Kahil, K.; Regev, O. Thermally Conductive Graphene-Polymer Composites: Size, Percolation, and Synergy Effects. *Thermally Conductive Graphene-Polymer Composites: Size, Percolation, and Synergy Effects* **2015,** *27*, 2100-2106.

174. Jarrett, R. N.; Merritt, C.; Ross, J.; Hisert, J. In *Comparison of Test Methods for High Performance Thermal Interface Materials*, Semiconductor Thermal Measurement and Management Symposium, 2007. SEMI-THERM 2007. Twenty Third Annual IEEE, IEEE: 2007; pp 83-86.

175. Thompson, D. R.; Rao, S. R.; Cola, B. A. A Stepped-Bar Apparatus for Thermal Resistance Measurements. *A Stepped-Bar Apparatus for Thermal Resistance Measurements* **2013,** *135*, 041002.

176. Zhang, T.; Luo, T. Giant Thermal Rectification from Polyethylene Nanofiber Thermal Diodes. *Giant Thermal Rectification from Polyethylene Nanofiber Thermal Diodes* **2015,** *11*, 4657-4665.